To Kim...and an end to a thirteen
week separation in our fourteen
week old marriage.

TABLE OF CONTENTS

Transfer Products from the Reactions of Heavy Ions with Heavy Nuclei

Kenneth Eugene Thomas III

Nuclear Science Division
Lawrence Berkeley Laboratory
and Department of Chemistry
University of California
Berkeley, CA 94720

ABSTRACT

Production of nuclides heavier than the target from ^{86}Kr and ^{136}Xe induced reactions with ^{181}Ta and ^{238}U has been investigated. Attempts were made to produce new neutron excessive neptunium and plutonium isotopes via the deep inelastic mechanism. No evidence was found in this work for ^{242}Np or ^{247}Pu. Estimates were made for the production of ^{242}Np, ^{247}Pu, and ^{248}Am from heavy ion reactions with uranium targets.

Comparisons of reactions of ^{86}Kr and ^{136}Xe ions with thick ^{181}Ta targets and ^{86}Kr, ^{136}Xe and ^{238}U ions with thick ^{238}U targets indicate that the "most probable" products are not dependent on the projectile. The most probable products can be predicted by the equation

$$Z-Z_{target} = 0.43\ (A-A_{target}) + 1.0.$$

The major effect of the projectile is the magnitude of the production cross-section of the heavy products. Based on these results, estimates are made of the "most probable" mass of element 114 produced from heavy ion induced reactions with ^{248}Cm and ^{254}Es targets.

These estimates give the mass number of element 114 as ~287 if produced in heavy ion reactions with these very heavy targets.

Excitation functions of gold and bismuth isotopes arising from ^{86}Kr and ^{136}Xe induced reactions with thin ^{181}Ta targets were measured. These results indicate that the shape and location (in Z and A above the target) of the isotopic distributions are not strongly dependent on the projectile incident energy. Also, the nuclidic cross-sections are found to increase with an increase in projectile energy to a maximum at approximately 1.4-1.5 times the Coulomb barrier. Above this maximum, the nuclidic cross-sections are found to decrease with an increase in projectile energy. This decrease in cross-section is believed to be due to fission of the heavy products caused by high excitation energy and angular momentum.

ACKNOWLEDGEMENTS

I wish to extend a special thanks to the following:

Mom and Dad, for their continuous support, encouragement, and love;

Fred Hurst, for getting me started in separations chemistry;

Glenn Seaborg, for providing the opportunity to do this work;

Diana Lee for her help with the computers and analysers and for always being so cheerful;

The SHEIKS research group for LUNCH, BEER, and rubber-band wars, and particularly Ken Moody for his assistance with the irradiations and Pat McGaughey for the backpacking and winetasting trips;

"Cal" Calhoun, for keeping me "safe" and even helping with the chemistry;

Fred Lothrop, Bob Stevenson, and the SuperHilac crew, for making sure I got beam;

And Kim, for marrying me even though I was a grad student, and for making me get out of grad school.

This work has been supported by the Nuclear Physics Division of the U. S. Department of Energy under Contract No. W-7405-ENG-48.

I. INTRODUCTION

A. Background

Since the first particle accelerators were built, a major effort has been made to produce new elements and new isotopes of known elements. The synthetic elements beyond element 101 were produced by light heavy ion[1] ($Z \leq 10$) reactions. In these reactions, two predominant mechanisms are observed—direct interaction and compound nucleus formation. Direct interaction or direct reactions involve the transfer of a few nucleons and, consequently, small transfers of energy. In compound nucleus formation the target "absorbs" the projectile to form an excited compound system which is statistically equilibrated. The compound system then deexcites by particle emission and fission.[2] Compound nucleus formation was the basis of the production of the elements $Z = 101$ to $Z = 106$.

As heavier projectiles are used and the compound nucleus is pushed beyond the known elements, fission of the compound system becomes more important. As the projectile mass reaches beyond that of argon, not only is fission of the compound system observed but also a new reaction mechanism is observed. The mechanism has become known by several names—deep inelastic transfer, strongly damped collisions and quasi-fission. This new mechanism has been observed in the reactions of very heavy ions[3] such as ^{40}Ar, ^{63}Cu, ^{84}Kr, and [illegible]Kr.[4-10] It now appears that incomplete fusion reaction or massive transfer may occur with projectiles lighter than argon.[11,12] Deep inelastic reactions have been observed to compete with compound nucleus formation more and more as the projectile becomes heavier. When the projectile is as heavy as Xe, no indication of compound nucleus formation is found.[13,14]

When compound nucleus formation using the reaction $^{48}Ca + {}^{248}Cm$[15-17] failed to produce superheavy elements with half-lives greater than several seconds, other methods had to be considered. One possibility is that the half-lives of the superheavy elements produced in the reaction $^{48}Ca + {}^{248}Cm$ are too short to be observed in previous experiments. Future experiments may be designed to search for shorter half-lives. Another possibility is that all of the superheavy elements undergo fission at the excitation energies available in the compound nucleus reaction. The deep inelastic transfer mechanism may allow significant mass transfer with low enough excitation energy to produce observable amounts of superheavy elements. For this reason the deep inelastic process has been considered a possible pathway to the superheavy elements.[18-21]

A wide range of projectile and target combinations has been used to study deep inelastic transfer reactions since this mechanism was first observed. It is beyond the scope of this work to attempt a summary or review of all of this effort. However, much of the work is discussed in several recent reviews and lectures.[2,18,22-25] The most attractive feature of deep inelastic transfer reactions for new element and new isotope production is the possibility of transferring large numbers of nucleons from the projectile to the target.

Deep inelastic processes have several distinguishing characteristics. The initial kinetic energy of the projectile is all or partially damped into internal excitation and collective degrees of freedom. This yields product kinetic energies ranging down to the Coulomb energies of the products. A transfer of nucleons takes place while the target and projectile are in contact. However, the product masses are observed in distributions centered around the target and projectile. For heavy target-heavy projectile systems the transfer of mass is mainly toward symmetry of the system. There is evidence that the degree of mass transfer is related to the dissipation of the kinetic energy.[26] The angular distributions of deep inelastic products show side peaking for light products whose kinetic energy is slightly above the Coulomb energy. Those light products resulting from a more direct reaction process are forward peaked. Products of various degrees of energy dissipation fall between these extremes. Further, large amounts of angular momentum transfer can result from deep inelastic collisions.

Most studies of the deep inelastic process have been performed using in-beam methods such as the E-ΔE telescopes.[27] These methods are limited to observation of products of $Z \leq 60$. Much important information about the kinematics of deep inelastic reactions has been gained through this work. However, only limited direct information about the heavy partner--particularly products heavier than a heavy element target--is gained in this manner. Several experiments have been performed to observe production of elements heavier than the target. Much of this work has been performed with uranium targets,[28-32] gold targets,[33] and tantalum targets.[34] In order to determine the best reactions to use in order to produce new elements and new heavy isotopes, it is helpful to map out production of nuclides above the target by observation of known nuclides. If trends in heavy nuclide production are observed, perhaps these trends can be applied to synthesis of new elements and new heavy isotopes from other target-projectile combinations.

B. Proposed Study

This work is presented in two parts. The first deals with attempts to produce new neutron excessive isotopes in the actinide region. The second deals with production of nuclides heavier than the target in a mass region where fission does not play as important a role in the deexcitation of primary products from deep inelastic collisions.

Heavy ion experiments with uranium targets[28-32] have shown that fairly broad isotopic distributions of the heavy actinide elements result from these reactions. It seems likely that previously unknown neutron excessive nuclides could be produced by deep inelastic reactions with sufficient cross-section to allow observation and identification. Because cross-sections drop fairly rapidly as Z is increased above the target, a good place to start a search for new nuclides is near the target.

Uranium was chosen as the target for the initial work in the new isotope production studies. Uranium foils are readily available and can be obtained in essentially monoisotopic composition (99.8 percent ^{238}U). Further, most other studies of actinide production in heavy ion reactions have been performed with uranium targets. For this reason any information peripheral to new isotope production from heavy ion reactions with uranium targets can be compared and added to existing data. Uranium requires no special handling as do other heavier actinide targets, and uranium can be obtained in thick foils to maximize the number of target atoms and thus the production of heavy nuclides.

Having chosen ^{238}U as the target, possible new heavy nuclides include ^{242}Np, ^{247}Pu, and ^{248}Am. All of these are predicted to be beta-particle emitters and the half-lives are predicted to be ~20 minutes, ~15 minutes, and ~25 minutes, respectively.[35] (Shortly after this work was initiated, ^{242}Np was produced through use of a different type of reacton.)[36] In order to observe any beta-particles emitted by these nuclides, it is necessary to chemically separate them from all other activities. If this work proved successful the experiments would be extended to other elements and other target-projectile combinations. If it did not prove successful (as was the case) estimates of production could be made and other possible reactions to produce these isotopes could be suggested. This region of the Chart of the Nuclides[37] is shown in Figure 1.

The second part of this study deals with heavy element production from tantalum targets. Tantalum was chosen as the target for this study for several reasons. First, it is essentially monoisotopic (~99.99 percent ^{181}Ta); this alleviates any ambiguity as to which target isotope the projectile reacted with to give a particular product. Second, use of tantalum as the target allows a range of Z of approximately ten over which to observe products heavier than the target. Since the cross-sections of most of these nuclides are expected to be less than one millibarn, chemistry is almost certainly required to observe these products and the chemistries of these elements are fairly simple. Third, tantalum is of high atomic number ($Z = 73$) so one would expect some similarity with reactions involving other high atomic number targets (with the exception of fission in the case of ^{209}Bi and ^{238}U targets). Finally, tantalum is a good target material. This means that tantalum has a high melting point (3000°C) and can thus withstand high beam intensities and therefore high temperatures. It also is a strong metal and can be rolled into thin self-supporting foils and can be obtained in high purity.

Experiments using thick tantalum targets were planned to map out the region of iridium to bismuth. This region of the Chart of the Nuclides[38] is shown in Figure 2. Chemical separations are required in order to observe the small amount of activity due to these nuclides as opposed to bulk activity due to all other reaction products. The samples are analysed for gamma-ray activity to identify individual isotopes. Nuclidic cross-sections are determined and plotted versus nuclidic mass number to obtain locations of the peaks in the isotopic distributions. Also, the decrease in cross-section with increase in Z above the target is observed. These results are compared with results from other heavy ion–heavy target systems to get an idea of trends in production above the target and to observe any differences caused by fission.

Also, as a part of this study, a series of thin target experiments were performed. The term "thin target" refers to a foil whose thickness is such that the beam energy is degraded a relatively small amount as compared to the term "thick target" which refers to foils which are thick enough to degrade the beam from the incident energy to the Coulomb barrier for the reaction. In other words, the energy of the beam as it exits a thin target is above the Coulomb barrier. Recoiling reaction products that escape from the thin target are stopped in aluminum. From the work of Otto, et al.,[39] ~10 mg/cm^2 of aluminum should be sufficient to stop essentially all recoils which might escape from the target. This series of experiments was performed to obtain information about the dependence of nuclidic cross-sections and of the shapes of isotopic distributions on the energy of the projectile. This, too, involved the use of chemical separations and gamma-ray analysis. Both the target and the aluminum catcher foil were dissolved in the separation procedure to insure the observation of all products from the reaction.

^{86}Kr and ^{136}Xe were chosen as the projectiles for this study for several reasons. First is a practical reason--these beams are "readily" available at the SuperHilac at beam intensities high enough (>100 namps. d.c.) to allow radiochemical studies. Also, both of these projectiles have been used in numerous reactions with tantalum and uranium targets and other heavy element targets, thus facilitating comparisons. Also, any differences in the reactions of the two projectiles are to be observed.

C. Other Heavy Ion Experiments with Tantalum and Uranium

A wide range of experiments has been performed with uranium targets. These include reactions induced by Kr and Xe ion projectiles at energies near the Coulomb barrier to determine the extent of Coulomb fission of uranium;[40-42] attempts to produce superheavy elements via compound nucleus formation with ^{63}Cu,[43] via fission of the compound system in the reaction of xenon with uranium,[44] and via the deep inelastic reactions of ^{86}Kr, ^{136}Xe, and ^{238}U with uranium.[45-49] Also, numerous experiments have been performed using heavy ion reactions with uranium to study the mass distributions,[6,11] and to study characteristics of deep-inelastic processes by measurements of charge distributions, angular distributions and kinetic energy spectra of fragments.[50,51] Several reactions with thick targets to measure heavy product yields have been reported as well.[28-32,34] These last experiments will be discussed further at the end of this work.

In contrast to uranium targets, tantalum has not drawn much attention. Investigation of one reaction with ^{86}Kr ions[52] and one with ^{136}Xe ions[53] are the major works. These experiments were designed to measure charge distributions, kinetic energy spectra and angular distributions of the projectile-like fragments to characterize the deep inelastic process. One set of experiments has been performed using the reaction of ^{84}Kr ions with tantalum targets (as well as other target-projectile combinations) to identify products heavier than the target.[34] Numerous other heavy ion reactions have been performed with targets such as ^{209}Bi, ^{208}Pb and ^{197}Au. Some of this work will be mentioned later in this paper. The reference list in Reference 22 will lead to descriptions of most of the work.

II. EXPERIMENTAL METHODS

In this section and the two which follow, a broad range of procedures will be discussed. These procedures may be classed as irradiations, chemical processing of targets, and data collection and analysis. Each of these will be discussed in detail in the following sections. Where necessary, the discussion will branch to consider the differences in the procedures for the handling of tantalum and uranium targets.

A. Irradiations

All irradiations performed as a part of this work took place at the Lawrence Berkeley Laboratory SuperHilac.[54] The SuperHilac is a linear accelerator which can deliver projectile ions as heavy as ^{208}Pb at energies up to 8.5 MeV per nucleon. Work is currently in progress to extend this capability to uranium beams.[55] The irradiations took place at the end of the 0° beam line-E32. More recently, this area has been enclosed and modified and is now termed the SHEIKS cave.

Energy measurements were performed by insertion of a Si-Au surface barrier detector into the beam-line just forward of the target system. Typical energy spectra are shown in Figure 3. The lower of these is for a ^{86}Kr beam and the upper spectrum is for a ^{136}Xe beam; the measured energies are shown on the spectra. There is a crystal defect involved with this type of measurement which shifts the measured energy spectrum approximately 30 MeV below the actual beam energy. Because of the location of the targets, there could be problems with "contamination" of the desired beam with lower energy ions. Special care was taken to see that these lower energy peaks in the beam energy spectrum were removed or kept to a minimum. This was checked before and after each irradiation as well as periodically throughout each irradiation. When extraneous energies exceeded approximately 10-20 percent of the total beam, the target was discarded. In all experiments reported on in this work, beam contaminants did not exceed a few percent.

Projectiles used in this study included ^{86}Kr and ^{136}Xe. The average charge state of the ^{86}Kr was +22 and that of the xenon ions was +29. These values were arrived at by the beam studies group[56] and were checked once during the experiments.

A listing of all irradiations performed in this work is given in Table 1. Each irradiation is designated by a code for identification. This code is read as experiment number two for the reaction of xenon with tantalum for the code XT2. A "K" used in this code represents the use of ^{86}Kr as the projectile. A letter representing the chemical fraction would follow this code.

B. Target Systems

All of the uranium target experiments used the copper TAG target system which has been in use at both the 88" cyclotron and the SuperHilac for many years. The target is mounted onto the face of a large copper block and held in place with an aluminum ring. The block and target arrangement fit into an adapter which in turn is connected to the beam line. A carbon collimator is located within the adaptor

Table 1. Irradiation Information

Experiment*	Target Thickness	Incident Energy (lab)	Length of Bombardment	Average Intensity
KU3	23.8 mg/cm^2	731 MeV	419 min	1600 nA d.c.
KU4	23.8	731	111	1660
XU5	20.1	1156	600	1290
KT3	21.6	731	355	940
KT4	4.77	506	206	250
KT5	4.70	394	193	360
KT6	4.68	731	255	400
KT7	21.6	731	443	1350
KT8	4.58	620	268	350
XT2	19.6	1156	287	870
XT4	19.6	1156	354	1120
XT7	5.24	1156	190	390
XT8	4.85	980	248	330
XT9	5.00	801	201	360

*Experiment code: K = ^{86}Kr; X = ^{136}Xe; U = uranium, T = tantalum; number represents experiment number of the reaction.

upstream from the target. The collimator used in these experiments is 1.2 cm diameter. Figure 4 gives a diagram of this system. Water is circulated through the copper block for cooling. The copper block serves as part of the Faraday cup for determining integrated beam intensity.

The tantalum experiments were carried out in the new SHEIKS cave area at the SuperHilac using a target system designed by Matti Nurmia and modified by Kenton Moody. This system is similar to the TAG system but with the capability of also handling gas-cooled thin targets. It is a modular system allowing easy removal of targets. A diagram of the system is given in Figure 5. Figure 6 is a photograph of the target system. Targets and catcher foils are mounted on an aluminum slug and held in place on the stainless steel, water-cooled beam stop with a copper ring. The inner diameter of this copper ring is larger than the diameter of the collimated beam. Water is circulated through the tail-piece cooling the target from the back. The tail-piece twistlocks onto a teflon ring which serves as an electrical insulator between the target and the collimator. The teflon ring, in turn, is mounted to the copper housing of a carbon collimator. Collimator sizes used in these experiments vary between 0.95 cm and 1.6 cm diameter. The copper housing is mounted to a second teflon ring which is mounted to the beam-line adaptor. The target tail-piece unit is used as a Faraday cup for beam integration. The beam flux is monitored and integrated by a Brookhaven Instruments Corporation electrometer in all irradiations.

C. Targets

The uranium targets used in this work were obtained from Lawrence Livermore Laboratory. These were depleted uranium disks 2.5 cm or 1.9 cm in diameter and 1.0 mm thick. From experience, this material was found to be free of impurities which would interfere with the chemistries. No elemental analysis was performed since it is not possible to produce the transuranium nuclides in significant amounts other than from the reactions with uranium.

The thick tantalum targets were obtained from Orion Chemical Co., Huntington Beach, Ca. This foil was approximately 0.076 mm thick. Table 2 gives the analysis of the material performed by Orion Chemical. Also, a sample of the foil was given to Dr. Walter Loveland of Oregon State University for neutron activation analysis. He observed no impurities in the material; Table 3 gives upper limits which were determined for a range of elements.

Thin tantalum foils of 0.0030 mm thickness were obtained from A.D. McKay, Darien, Ct. These are pin-hole free unsupported metal foils. An analysis of the foil is given in Table 4. The major contaminant is niobium. The compound nucleus from the reaction of krypton with niobium is iridium. This is lower in Z than the products of interest—gold and bismuth—and thus is no problem in the reactions studied. However, in the reaction of xenon with niobium this is not the case. Gold and bismuth would not arise from a compound nucleus type reaction between niobium and xenon, but could conceivably arise from a transfer of mass to xenon (see, for example, Ref. 57 and 58).

Table 2. Analysis of 0.076 mm 99.99^{+}% Tantalum (in ppm). Reported by Orion Chemical Co. (Lot 1715)

Pb + Bi	<10	Ni	5
Nb	25	Si	5
W	25	all other	<10
Fe	30		

Table 3. Analysis of 0.076 mm 99.99^{+} tantalum (in ppm). Reported by Walter Loveland. (Upper limits only - no impurities observed)

Cl	45	Sb	1.2
Ba	330	Ce	1.3
Dy	0.44	Sm	0.54
Mn	1.1	Eu	0.11
Lu	0.24	Tb	0.25
Cr	7.2	Yb	2.8
Hg	1.6	Sc	48 ppb
In	15	Co	0.086 ppb

Table 4. Analysis of 0.0030 mm Tantalum (in ppm). Reported by A. D. McKay, Co.

Al	5	Mo	100	V	5
Ca	2	Na	10	W	100
Co	1	Nb	<500	Zr	10
Cu	2	Ni	3	C	2
Fe	30	Si	10	H	2
Mg	5	Sn	2	N	25
Mn	2	Ti	20	O	50

However, since a sizeable mass transfer is involved to produce gold and bismuth from xenon, the cross-section for this reaction would be extremely small. This fact combined with the relatively small amount of niobium present renders the contribution to gold and bismuth from this source insignificant. This same argument should hold for any impurity of lower mass than tantalum. The only real problems would arise from significant quantities of impurities heavier than tantalum and these are absent in both the thick and the thin tantalum targets.

The aluminum foil used as a recoil catcher in the thin target experiments was also obtained from Orion Chemical Co. This material had a thickness of 0.015 mm and was 99.999 percent pure. An analysis of the foil is given in Table 5.

Target thicknesses were determined by two different methods depending on whether the beam stopped in the foil or was only degraded in energy when passing through the foil. The thin tantalum targets were obtained pre-cut into one inch square pieces. These measurements were checked and the foil was then weighed. The thickness in mg/cm^2 was determined by dividing the weight in mg by the area of the foil in cm^2. The foil was assumed to be of uniform thickness.

The thicknesses of the thick targets were determined by the following method. The thickness used in cross-section calculations was determined by calculating the thickness of tantalum or uranium required to degrade the beam energy from its incident energy down to the Coulomb barrier. The range-energy tables of Northcliffe and Schilling[59] were used in these estimations. The Coulomb barrier was determined using the relation:

Table 5. Analysis of 0.015 mm 99.999% Aluminum (in ppm). Reported by Orion Chemical Co. (Lot 4119)

Ca	0.1	Mn	1
Cu	1	Si	3
Fe	4	All Others	<1
Mg	0.2		

$$B = \frac{1.44\ (Z_t)\ (Z_p)}{1.22\ (A_t^{1/3} + A_p^{1/3}) + 2.0}$$

obtained from Reference 60A, B. From this equation the energies of the projectiles (in the laboratory frame) required to overcome the Coulomb barrier are:

$^{136}Xe + {}^{181}Ta$	652.8 MeV
$^{86}Kr + {}^{181}Ta$	389.1 MeV

III. CHEMISTRY

A. General

This section is devoted to the chemical procedures used in this work. As a part of the discussion the chemical properties upon which the separations are based will be considered briefly. The procedures themselves are a combination of numerous procedures and methods used elsewhere. These methods are tied together in a smoothly flowing chemistry which is a compromise of time and purity. The goal of most of the work is to obtain as pure a sample as possible within a relatively short timescale (about 2 hours, at most). The procedures discussed here were arrived at through numerous trials and uses and represent the best procedure used. Certainly there are alternate methods which could be used and numerous revisions can improve upon the separation procedures used here. Following the separation procedures will be a discussion of chemical yield determination and a summary of samples obtained from each experiment.

The neptunium-plutonium chemical procedure was designed purely for observation of new beta-particle emitters. A consequence of this was that steps which may have increased chemical yield were ignored in order to shorten the separation time. Later, this chemistry was used in combination with gamma-ray analysis to determine the cross-sections and thus isotopic distribution of those nuclides produced in order to explain why no new beta-particle emitters were observed. The transplutonium separation was originally designed for alpha-particle analysis of transplutonium samples from heavy ion reactions with uranium.[31,32] This was modified to follow the neptunium-plutonium chemistry in this work. The goal of this procedure was to obtain cross-sections for the production of americium isotopes via gamma-ray analysis in order to determine the feasibility of new americium isotope production. Therefore, the sample did not need to be as clean as that for beta-particle counting.

Similarly, it is not necessary to have absolutely pure fractions for samples from the tantalum target chemical procedures. However, the cleaner the fraction is, the easier and more reliable the analysis will be.

All chemicals in this work are standard reagent grade chemicals obtained from numerous chemical supply firms. Saturated HCl solution is prepared before use by bubbling HCl gas into reagent grade concentrated HCl solution. Solutions are prepared by dilution of the appropriate reagent with purified water obtained from a Millipore Water Purification System. This system contains two mixed-bed ion-exchange cartridges, an activated carbon cartridge, and two filters.

Ion-exchange resins were obtained from Bio Rad Laboratories. No further sizing of the resins was performed. All columns packed with resins were prepared by slurrying the resin in water and adding small amounts of the slurry to the column full of water. As each aliquot settled, another was added until the column of resin was the appropriate length. Next, a series of solutions of various HCl and NaOH concentrations was cycled through the column followed by a water wash. Finally, the column was equilibrated with the appropriate solution before use. Columns used to contain the resin were thick glass-walled tubes ending in a platinum tube tip and having a reservoir at the top. Pressure was supplied via tygon tubing and a regulator valve from a cylinder of compressed nitrogen.

The pH was determined using a Corning Digital 109 General Purpose pH meter and a Ag/AgCl electrode.

B. Uranium Targets

The following discussion and procedure is based on information and procedures contained in References 61-69. No single part of the procedure comes exclusively from a given reference but represents the use of a mixture of information from several references. Further details of chemical properties and procedures may be obtained from the sources contained within this reference list.

Uranium metal is readily soluable in numerous reagents including nitric acid and aqua-regia. However, there is very little control over the dissolution using these reagents alone. In this work it is necessary to have a fast, reproducible, controlled dissolution of the target. A uranium-hydrochloric acid electrochemical cell allows this. The major reactions employed in this cell are:

$U > U^{+4} + 4\ e^-$

$2e^- + 2\ H^+ > H_2$

Theoretically, the dissolution should be a function of time governed by the equation

$$N = \frac{(i)(t)}{(F)(n)}$$

where N = moles of uranium

i = current in amperes

t = time in seconds

F = 96,400 Coulombs/mole of electrons

n = moles of electrons

Figure 7 shows examples of calibration curves for hydrochloric acid and nitric acid media. Deviations from the theoretical curve are due in part to competing oxidation-reduction reactions; however, the method allows a rough estimate and some degree of control of the dissolution of the uranium metal target.

Once the uranium is dissolved, the problem becomes one of obtaining samples pure enough for counting by the appropriate method. Since plutonium and neptunium are to be analysed for beta-radiation emission rate, an extremely high degree of purity is required. The transplutonium sample is to be analysed for gamma-ray activity arising from the decay of americium isotopes, so extreme purity is not necessary in the preparation of this sample.

For neptunium and plutonium it becomes necessary to achieve high separation factors from the large mass of uranium, extremely high activities of lanthanides, zirconium, hafnium, and the elements between lead and uranium. The first separation to be performed is removal of uranium and the bulk of radioactivities. A lanthanum fluoride precipitation performed with lanthanum and zirconium carriers will co-precipitate all +3 lanthanides and actinides as well as neptunium (IV and V), plutonium (III and IV) and thorium. Most other activities including zirconium, hafnium, protactinium, and uranium (present as UO_2^{+2}) do not precipitate. Washing of the precipitate will remove residual contaminants trapped in the precipitate.

Anion-exchange chromatography may be employed for separation of neptunium and plutonium from all other activities precipitated by lanthanum fluoride. If the dissolved fluoride precipitate is loaded onto an anion-exchange column in approximately 8M HNO_3, thorium, neptunium, plutonium (IV) and any residual uranium are adsorbed and the +3 actinides and lanthanides can be eluted with clean 8M HNO_3. Thorium can be removed from the anion-exchange column by elution with 9M HCl. Because of "tailing" of the thorium band, further purification from thorium is required. Neptunium and plutonium are only slightly adsorbed onto anion-exchange resin from 1M HCl and can thus be removed from the column and the residual uranium which will remain on the resin.

Upon further treatment on a clean anion-exchange column, neptunium and plutonium can be completely separated from thorium and then from each other. Loading the column in 9M HCl minimizes adsorption and tailing of thorium. Neptunium-plutonium separation is achieved by reduction of plutonium (IV) to plutonium (III) using hydroiodic acid. Plutonium (III) is not adsorbed by an anion-exchange column. Neptunium is not adsorbed from a dilute HCl-HF solution and can be removed from the column with this mixture.

Returning now to the actinide-lanthanide fraction, it is necessary to remove the bulk of the activity in order to detect the relatively low levels of activity of americium. This fraction is not to be counted to determine beta-particle activity so extremely high purity is not necessary. Separation of actinides from lanthanides can be partially achieved through the use of a cation-exchange column and elution with saturated HCl solution. The sample is prepared for this step by precipitation of the +3 lanthanides and actinides as the hydroxides using lanthanum carrier. After dissolution of $La(OH)_3$ with HCl gas, radium can be precipitated onto $BaCl_2$ using barium carrier. Following these steps the sample can be loaded onto a cation-exchange column. The +3 actinides exhibit lower adsorption than most of the +3 lanthanides when the HCl concentration is greater than approximately 12M. Elution with saturated HCl solution (~13M) brings the transplutonium ions and ions of the heaviest lanthanides off of the column in the first fraction. Actinium and the bulk of the lanthanides are retained on the column at this point. Depending on where the cut is taken for the first fraction, some of the residual radium may still be in the sample. This procedure is discussed in greater detail in Reference 70.

A final clean-up step is required, particularly if the sample is ever to be analysed for alpha-particle activity. Up to this point, no effort has been made to remove the lead and bismuth daughters which have been growing in from their thorium and actinium parents since the initial precipitations. The final step makes use of the adsorption of lead and bismuth onto an anion-exchange column from dilute HCl. Under these conditions, the transplutonium ions are not adsorbed. The sample obtained after this step should be "clean" enough for alpha-particle analysis and gamma-ray analysis but is not clean enough for beta-particle detection due to the presence of lutetium and possibly ytterbium activities.

An attempt was made to obtain a pure americium sample for beta-particle detection. The procedure attempted was based on the methods of Moore.[71,72] The procedure called for oxidation of americium (III) to americium (V) followed by either solvent extraction or extraction chromatography using bis(2-ethylhexyl) orthophosphoric acid (HDEHP) as the extractant. Although the step involving extraction chromatography was relatively short and gave a high chemical yield, it was necessary to use it as part of the existing transplutonium chemical procedure or develop a similar chemistry in order to obtain a high purity americium sample. Because of the length of time involved in separation and the low cross-sections predicted for any new beta-particle emitting americium isotope, this approach was abandoned.

The details of the chemical procedure discussed above can be described as follows. The dissolution procedure is one developed for use with thick uranium targets.[61] A drawing of the dissolver apparatus is shown in Figure 8. A flow scheme of the separation is given in Figures 9 and 10.

Prior to irradiation, the uranium foil is cleaned of oxides in 8M HNO_3, rinsed in water and then in ethanol and dried. The target is stored in vacuum until the irradiation. After irradiation the target is placed in a teflon cup on top of a copper electrode (see Figure 8). The irradiated side of the target should be face up. A teflon tube is screwed down firmly on top of the uranium and the entire apparatus is adjusted so that a platinum coil electrode is just above the metal target. The platinum electrode is connected to an oscillator and electrically connected to the negative lead of a voltage source. The copper electrode is connected through an ammeter to the positive lead of the voltage source.

At this point in the procedure, 2 ml of 2.5M HCl is added to the teflon holder. The oscillator source is turned on and the teflon holder is further adjusted so that the platinum electrode gives adequate stirring of the solution. The voltage source is now turned on and the voltage is adjusted so that the ammeter reads 1.5 ampere. The timer is started at the instant the power is turned on and timed for approximately ninety seconds. During this time the voltage will periodically have to be adjusted to maintain a 1.5 ampere current. At the end of the dissolving period, the voltage source is turned off and the platinum electrode is removed.

The black uranium-hydrochloric acid solution is removed from the teflon holder and transferred to a 15 ml centrifuge cone containing tracers and carriers. The target and holder are rinsed with two 75λ washes of water which are added to the uranium-hydrochloric acid mixture. Finally, the solution is heated in an oil bath and concentrated nitric acid and hydrochloric acid are added dropwise until the solution turns to the clear yellow of UO_2^{+2}.

Using the above dissolution procedure it is possible to dissolve about 120 mg from the face of the target. This translates to approximately 60 mg/cm^2 which is sufficiently greater than the range of the projectiles so as to capture all recoiling reaction products within the target.

The centrifuge cone into which the uranium solution is transfered contains approximately 500 micrograms of lanthanum and 500 micrograms of zirconium as solutions of the nitrates. The tracers used are ^{237}Np and ^{238}Pu. After treatment of the solution with nitric acid, the yellow solution is cooled in an ice-bath and approximately 300λ of concentrated hydrofluoric acid is added (enough to yield a roughly 2M solution of HF). The solution is allowed to stand for 3-5 minutes--long enough to transport the liquid from the SuperHilac to the Nuclear Science Building. The test tube containing the fluoride solution is then centrifuged for 1 minute at high speed and the yellow solution is then removed from the lanthanum fluoride precipitate.

The lanthanum fluoride precipitate is now washed with two 500λ aliquots of 2M HCl-HF solution to remove any trapped target solution. Next, three drops of saturated boric acid solution and 150λ of concentrated nitric acid are added to the precipitate. The solution obtained from dissolution of the precipitate is roughly 8M in HNO_3.

It is transferred to the top of an anion-exchange column (2.5 cm x 3 mm i.d.; Dowex 1x8, 400 mesh; flow rate = 6 drops per min.) in the nitrate form. The solution is forced into the column using pressurized N_2. The test tube is rinsed with one drop of 8M HNO_3 and this solution is transferred to the column and forced in. Next, the top of the column is washed with one drop of 8M HNO_3 and this, too, is forced into the column. The column walls above the resin bed are dried with a cotton swab. (Note: These added column preparation steps were found to be necessary to prevent cross-contamination of fractions.)

The anion-exchange column is rinsed with 20 drops (~0.02 ml/drop) of 8M HNO_3 to remove the +3 lanthanides and actinides for further processing (to be described later). The next step is to remove thorium from the column by elution with 25 drops of 9M HCl. Finally, neptunium and plutonium are removed from the column in 30 drops of 1M HCl. This solution is taken to dryness and then taken up in two drops of 9M HCl.

The two drops of 9M HCl are added to the top of a fresh anion-exchange column similar to the one used above. The performance of this column is shown in Figure 11A. The solution is forced into the column and followed first by a one drop wash of the test-tube and then a one drop wash of the top of the column with 9M HCl. Again, the top of the column is dried with a cotton swab. The column is now washed with an additional 15 drops of 9M HCl to remove any residual thorium; this effluent is discarded. Plutonium is now eluted from the column by reduction to the +3 oxidation state with 0.2M HI/12M HCl; 15 drops are collected and evaporated onto a 0.05 mm thick platinum disk as the plutonium sample. Finally, neptunium is obtained by elution with 0.1M HF/4M HCl; 10 drops are collected and evaporated onto another 0.05 mm platinum disk as the neptunium fraction.

The samples are then mounted onto aluminum counting cards and covered with one thickness of saran wrap. The samples are finally placed in the beta-particle detectors for periods up to 1 month after the end-of-bombardment. Table 6 gives an example of the times involved for various steps in this chemical procedure.

At this point, some comments are necessary concerning the purity of the neptunium and plutonium samples. Separation factors were measured for separation of uranium, thorium, americium, and protactinium from neptunium and plutonium. All separation factors (the ratio of the initial count-rate to the count-rate in the chemical sample) were at least 10^5 and most likely much higher. It is expected that the +3 lanthanides would exhibit separation factors similar to that of americium. Analysis of the gamma-ray spectra of the experimental samples showed no cerium contamination and no unidentified gamma-ray energies. The plutonium-neptunium separation proved equally effective with decontamination of the plutonium sample being greater than 10^5. Decontamination of the neptunium fraction was not measured directly but is believed to be greater than 10^3 on the basis of low-level tracer results.

Attention is now turned to the transplutonium fraction. Separation times are given at the bottom of Table 6. These times are applicable when one person performs the full chemistry. The time required for the transplutonium chemistry can be shortened substantially and that for the neptunium-plutonium chemistry can be shortened slightly by drafting a second person to perform one of the chemical procedures.

After removal from the first anion-exchange column, the 8M HNO_3 solution is neutralized with concentrated ammonium hydroxide by adding the reagent dropwise until the solution turns cloudy, and then two drops more are added. The mixture is cooled in an ice-bath and the precipitate, $La(OH)_3$, is centrifuged out. This is primarily a volume reduction step. Following centrifugation and removal of the supernatant, the precipitate is washed with two 500λ aliquots of cold water. HCl gas is then bubbled into the precipitate for 3 to 5 minutes after the precipitate dissolves. Following this, 1 mg of $Ba(NO_3)_2$ solid is added to the solution, the mixture is cooled in an ice-bath, and more HCl gas is bubbled in. The mixture is then centrifuged and the solution is removed from the $BaCl_2$ precipitate.

The saturated HCl solution containing the lanthanides and actinides is placed on the top of a cation-exchange column (6 cm x 3 mm i.d.; AG MP-50 resin; flow rate = 3 drops/min) in the hydrogen form. The solution is forced into the column and a drop of saturated HCl is added to the top of the column. This, too, is forced in and the top of the column is dried with a cotton swab. The transplutonium

Table 6. Chemical Separation Times (Time after end-of-bombardment) for Neptunium-Plutonium and Transplutonium Separations.

Beam off	0.0 min
Dissolution complete	2.5
LaF_3 and wash complete	17
on 1st anion-exchange column	18
An-Ln off column	26
Th off column	32
Np-Pu off column	37
on 2nd anion-exchange column	50
Th off column	55
Pu off column	59
Np off column	62
$La(OH)_3$ and wash complete	68
$BaCl_2$ precipitation	82
on MP-50 column	84
TP off MP-50 column	93
on 1.5M HCl column	106
TP off 1.5M HCl column	110

elements are eluted from the column with 35-40 drops of saturated HCl. The performance of the MP-50 column is shown in Figure 11B. The effluent is taken to dryness in a centrifuge cone and taken up in two drops of 1.5M HCl.

The 1.5M HCl solution is placed on the top of a third anion-exchange column similar to the other two mentioned above. The test-tube is rinsed and the column prepared as before. The transplutonium elements are eluted in the first 15-20 drops and this fraction is evaporated onto a 0.05 mm thick platinum disk for analysis.

The only major contaminants in this fraction are ytterbium and lutetium. These could have been removed as well by use of a longer MP-50 column or using an alchohol saturated HCl solution. However, both of these procedures would have increased the required time for separation considerably by taking longer to elute the transplutonium ions from the column and by yielding larger volumes of effluent to be evaporated. Alpha-particle pulse-height analysis showed no contaminating alpha-particle peaks.

C. Thick Tantalum Targets

In this section will be discussed the separations performed on thick irradiated tantalum foils. The information and procedures are contained in References 73-84. Two separation procedures are discussed here. The first is designed to remove a gold fraction, a platinum-iridium fraction, and a mercury fraction. The second is designed to separate out thallium, bismuth, and lead into individual fractions.

Tantalum has the qualities of a good target but its chemical properties cause problems with the separations of all the elements of interest. The metal is only readily soluble in mixtures of strong HF and HNO_3. The dissolution of 300-350 mg of tantalum requires rather large amounts of HF. The presence of such high concentrations of fluoride complicates most of the normal subsequent separation procedures. Because of this, instead of separating the other elements from the tantalum, it was decided to remove tantalum from the solutions before further separations. The presence of fluoride (or some other strong complexing agent) is required for tantalum to remain in solution. If sufficient boric acid is added to complex all fluoride, tantalum will precipitate out as the oxide. This then allows the use of "normal" separation procedures. However, the large amounts of near colloidal precipitate and high concentrations of fluoroborate cause significant reductions in chemical yields by trapping and adsorption in the precipitate.

Platinum and iridium both form salts with cesium of the form Cs_2MCl_6 where M represents the metal ion. This will occur if the metal ions are in the +4 state but not in the lower oxidation states. Under the conditions existing in solution, iridium has a tendency to reduce to the +3 state; hydrogen peroxide added to the solution can oxidize iridium to the +4 state.

Both gold and thallium can be extracted into ethyl acetate from solutions with an HCl concentration greater than about 1.5M or an HNO_3 concentration of ~8M. At somewhat higher HCl concentrations, various other metals are extracted as well. Mercury is the only other metal showing any extraction at low HCl concentrations and its affinity for the organic phase is small and approaches zero at about 1.5M HCl. In order to obtain gold or thallium in reasonably pure form, it is first necessary to extract them from solutions of approximately 3M HCl to separate them from bulk activity. Then, the organic phase can be washed with 1.5M HCl to remove most other metal contaminants including mercury. For further purification, gold metal can be precipitated or plated onto copper powder. Thallium can be reduced to +1 with sodium sulfite solution and then precipitated as the iodide.

Mercury can be reduced to the metal or to mercurous chloride with stannous chloride solution. Mercury can also be plated onto copper powder from 1M HCl.

Both bismuth and lead are extracted from aqueous solution by diphenylthiocarbazone (dithizone) in an organic solvent. Bismuth is extracted from a solution of pH ~2 into a CCl_4 phase containing dithizone. Silver will also extract at this pH; therefore, steps such as silver chloride precipitation or plating of silver onto copper powder are necessary clean-up steps. Bismuth can then be precipitated as BiOCl by dilution of an HCl solution with water. Lead is best extracted with $ChCl_3$ as the organic phase from a solution of pH ~8 using citrate ion to stabilize the metal ion at this pH and using cyanide ion to prevent the extraction of some contaminants. Once back-extracted into a weak acid solution, lead can be precipitated as

$PbCrO_4$. (Note: Even with the cyanide ion present, enough contaminating activity followed the lead in this procedure so as to make the lead fraction too impure to be useful.)

Flow schemes for chemical procedures I and II used for thick tantalum targets are given in Figures 12 and 13. The dissolution procedure for both chemical procedures is the same. Approximately 300 mg of 0.076 mm tantalum foil is placed in the bottom of a plastic centrifuge cone. The cone contains tracers and appropriate carriers (~1 mg of each). To the cone, 1 ml of 4:1 concentrated HF: concentrated HNO_3 is added. Once bubbles begin to form the reaction becomes extremely violent and produces a large amount of heat. As the reaction slows, concentrated HNO_3 is added dropwise until all of the tantalum dissolves. The solution is boiled in an oil bath for several minutes in order to boil away excess HF and HNO_3. The solution is diluted to ~2 ml with water, approximately 300 mg of B_2O_3 powder is added, and the solution is heated for another 5 minutes. Next, the solution is cooled and as much white Ta_2O_5 precipitate as possible is centrifuged out. The solution is removed from the precipitate, placed into a clean glass centrifuge cone, and allowed to stand for a few minutes. Another centrifugation is performed and the solution is transferred to a new tube. The solution is usually still cloudy at this point but most of the Ta_2O_5 has been removed.

To the approximately 2 ml of cloudy solution, roughly 1 ml of ethyl acetate is added with vigorous shaking for 1 minute. (In chemical procedure II, approximately 100λ of concentrated HCl are added during this extraction to enhance the thallium yield.) The mixture is centrifuged and the organic phase transferred to a clean centrifuge cone. Another aliquot of ethyl acetate is added to the aqueous phase and the extraction repeated; the two organic phases are combined for processing for gold or thallium. The aqueous phase is set aside for further treatment. At this point the two procedures begin to differ.

The carriers used in chemical procedure I (Figure 12) include 1 mg each of platinum, iridium and mercury all added prior to dissolution of the target. The organic phase from chemical procedure I is processed for gold. It is evaporated to near dryness and 1M HCl is added. The solution is heated further until all ethyl acetate has evaporated and then the solution is cooled. Approximately 1 mg of copper powder is added and the mixture is shaken for 1 minute. The mixture is then filtered and the powder washed with 1M HCl and then water. The sample is then mounted for counting.

The aqueous phase from the extraction is processed for platinum, iridium and mercury using chemical procedure I. Approximately 500λ of 30 percent H_2O_2 and 500λ of concentrated HCl are added to the aqueous phase and the solution is heated in an oil bath for a few minutes. The solution is centrifuged to remove any Ta_2O_5 which may have precipitated, transferred to a clean centrifuge cone, and then ~50 mg of CsCl solid is added to the solution. The solution is again heated, then cooled in an ice bath. The mixture is centrifuged and the supernatant is transferred to a clean test-tube. The

Fig. 15. Detection efficiency calibration curve for β^- detectors.

Fig. 16. Detection efficiency calibration curves for several counting arrangements of Ge(Li)3.

Fig. 17. Detection efficiency calibration curves for several counting arrangements of Ge(Li)4.

Fig. 18. β^- decay curve for neptunium fraction from experiment KU4.

Fig. 19. β^- decay curve for plutonium fraction from experiment KU4.

Fig. 20. Flow scheme for gamma-ray spectra data analysis.

Fig. 21. Gamma-ray spectrum of thallium fraction from experiment KT7.

Fig. 22. TAU2 display from analysis of the thallium fraction from experiment KT2.

Fig. 23. Isotopic distributions for Np, Pu, and Am from the reaction of ^{86}Kr ions with a thick uranium target. Incident energy is 731 MeV (8.5 MeV/A). Dashed curves are intended to aid the eye and are only approximations. The Np distribution is a result of quasi-elastic transfer and deep/inelastic transfer.

Fig. 24. Isotopic distributions for Np, Pu, and Am from the reaction of ^{136}Xe ions with a thick uranium target. Incident energy is 1156 MeV (8.5 MeV/A).

Fig. 25. Isotopic distributions for products heavier than tantalum from the reaction of ^{86}Kr ions with a thick tantalum target. The incident energy is 731 MeV (8.5 MeV/A). Solid points represent measured cross-sections. Open points represent cross-sections corrected for feeding from the parent where the two cross-sections differ. The curves are "eyeball" fits to the corrected cross-sections.

The dissolution and extraction steps of chemical procedure II (Figure 13) are the same as in procedure I. The only carrier used initially is lead (0.5 mg) as a solution of the nitrate; [illegible] carriers are added later. After the extraction with ethyl acetate, the organic phase is washed with two 500λ aliquots of 1.5M HCl. Thallium is then back-extracted from the ethyl acetate into an aqueous solution of sodium sulfite. At this point, 1 mg of thallium carrier (as an aqueous solution of thallous chloride) is added to the sodium sulfite solution used for back extraction. Roughly 500λ of saturated potassium iodide solution is now added and the solution is heated for a short time. Next, mixture is cooled in an ice-bath, then centrifuged, and the supernatant is discarded. The precipitate is washed with a small amount of ice water and filtered, and then the sample is mounted.

The aqueous phase from the ethyl acetate extraction is carefully adjusted to pH 2.5 by dropwise additions of concentrated NH_4OH and 6M NH_4OH. The pH must not be allowed to become greater than 4. A large amount of white precipitate will form; this is the remainder of the Ta_2O_5. After centrifuging out the Ta_2O_5, the pH is checked and readjusted as necessary. Two extractions using 500λ aliquots of dithizone (DTZ) solution (25 mg DTZ/50 ml CCl_4) are performed; the two organic phases are combined. A back-extraction is then performed on the DTZ solution using two 500λ aliquots of 2M HCl. At this point, either silver carrier for silver chloride precipitation or copper powder for reduction and plating of silver ion is added to remove silver (the copper powder was found to be more effective). Finally, 1 mg of bismuth carrier (as an aqueous solution of the chloride) is added to the HCl solution, the solution is diluted to about 20 ml with water and a few drops of dilute NH_4OH are added to precipitate BiOCl. The solution is heated for a short time then cooled in an ice-bath and filtered. The filtered precipitate is washed with cold water and then mounted.

Turning attention now to the aqueous phase from the DTZ extraction, the final task is to remove lead. To the solution are added 600λ of saturated sodium citrate solution and 100λ of saturated potassium cyanide solution. The pH of the solution is now adjusted to 8.5 with 6M NH_4OH. Three 1 ml aliquots of DTZ/$CHCl_3$ (300 mg DTZ/50 ml $CHCl_3$) are used to extract lead. The organic phases are combined and back-extractions are performed using three 1 ml aliquots of 0.5M HCl. Roughly 500λ of saturated Na_2CrO_4 solution is added to the aqueous phase and then 1M NH_4OH is added dropwise until the formation of $PbCrO_4$. The precipitate is filtered, washed with cold water and mounted.

The thallium fraction from chemical procedure II is very clean with the only contaminants being osmium and a small amount of iodine. Even with steps to remove silver there is a large amount of contamination due to silver and other activites near silver in the bismuth fraction. The lead fraction is so heavily contaminated that lead activities are not observable. Examples of the separation times involved in chemical procedures I and II are given in Tables 7 and 8.

Table 7. Chemical Separation Times for Tantalum Chemistry I

Beam off	0.0 min.
Ethyl acetate extraction	30
Gold plating	45
Cs_2MCl_6 precipitation	60
Hg precipitation	105
Hg plating	120

Table 8. Chemical Separation Times for Tantalum Chemistry II

Beam off	0.0 min
Ethyl acetate extraction	40
SO_3^{-2} back-extraction	50
TlI precipitation	55
pH = 2.7	70
DTZ extraction	75
Back-extraction	80
BiOCl precipitation	90
pH = 9	110
DTZ extraction	120
Back-extraction	125
$PbCrO_4$ precipitation	130

D. Thin Tantalum Target

The chemical procedure for the thin tantalum foil-aluminum catcher foil combination is similar to the previous two procedures. The dissolution procedure is different to make provision for the smaller amount of tantalum and a small amount of aluminum. The separation procedure is designed to obtain bismuth and gold in a relatively short period of time. No carrier is used initially; however bismuth and silver carriers are added later in the procedure where necessary. The flow scheme for this separation procedure is shown in Figure 14.

The roughly 30 mg of tantalum and 65 mg of aluminum are placed at the bottom of a plastic centrifuge cone. First, 250λ of 4:1 concentrated HF: concentrated HNO_3 is added followed by 250λ of concentrated HCl. When the reaction slows, the volume is increased to 1 ml with water. Dropwise addition of concentrated HCl continues until all of the aluminum dissolves (the tantalum dissolves "instantly" upon addition of the HF-HNO_3 solution). Next, 100 mg of B_2O_3 powder are added to the solution in the cone and the mixture is diluted to 2 ml with water. After heating for 5 to 10 minutes and then cooling in a ice bath the mixture is centrifuged and the supernatant is transferred to a glass test-tube.

Two extractions are now performed using 1 ml of ethyl acetate for each extraction. The two organic phases are combined for processing for gold. The organic phase is washed twice with 500λ of 1.5M HCl. Finally, the organic phase is boiled down in volume and then evaporated onto a platinum disk for counting.

The aqueous phase from the ethyl acetate extraction is boiled down to ~1 ml then cooled and any remaining Ta_2O_5 centrifuged out. The supernatant is transferred to a clean cone and the pH is adjusted to 3 with concentrated NH_4OH and 6M NH_4OH. Again, any precipitate is centrifuged out and the pH is readjusted as necessary. A dithizone extraction is performed using two 500λ aliquots of DTZ/CCl_4 (25 mg DTZ/50 ml CCl_4). The organic phases are combined and a back-extraction is performed using two 500λ aliquots of 2M HCl. This is followed by either a silver chloride precipitation by addition of silver carrier or plating of silver onto copper powder (without carrier). Following this step, 1 mg of bismuth carrier (as an aqueous solution of the chloride) is added, the solution is diluted to 20-30 ml with water, and a few drops of 1M NH_4OH are added. The BiOCl precipitate is filtered out of the solution and washed with cold water. The sample is then mounted.

The gold fraction contains iodine and rhenium as contaminants but neither are of high enough activity to obscure the gold gamma-ray lines. The bismuth fraction contains substantial contamination from silver and silver-like products. This complicates the bismuth analysis in the thin target experiments particularly in experiments where bismuth isotopes are produced with low cross-sections. Plating silver onto copper powder does a better job of silver removal than the silver chloride precipitation. Separation times are given in Table 9.

Table 9. Chemical Separation Times for Thin Tantalum Chemistry

Beam off	0.0 min
Ethyl acetate extraction	29
Sample evaporation	34
pH = 2.8	47
DTZ extraction	54
Back-extraction	57
Ag plating	59
BiOCl precipitation	64

E. Chemical Yield Determinations

Two methods are used in determining chemical yields in the uranium and tantalum experiments: addition of tracers and X-ray Fluorescence Analysis. For tracer chemical yields, alpha-particle, X-ray, and gamma-ray analysis techniques are used where necessary. A known volume of tracer is added to the centrifuge cone to be used in the dissolution step of the chemistry and another equal volume aliquot of the same tracer solution is evaporated onto a platinum disk. The use of mercury is the exception; evaporation of the tracer solution can cause the mercury to be volatilized away. Therefore, the mercury tracer aliquot is absorbed onto a stack of two or three pre-cut filter papers and the stack is taped onto a counting card.

All tracers emitting gamma-rays are counted on the same Ge(Li) detector as their corresponding chemical fractions. The tracer activity is determined by summing the counts in a peak and subtracting out a background determined from the regions just above and just below the peak. The count-rate is then corrected for detection efficiencies. Sample activities are obtained from SAMPO and TAU2 (see Data Collection and Analysis); the TAU2 results have been corrected for detection efficiency. The chemical yield is determined by taking the ratio of these two activities. Errors in the chemical yields determined by the above method are generally less than 5 percent.

Thallium chemical yield is determined by X-ray analysis of ^{204}Tl tracer. X-ray counts of the chemical fraction and the tracer sample are performed on the same detector at the same distance from the face of the detector. Under these conditions, no detection efficiency corrections are necessary. The determinations are made sufficiently long after bombardment (~1 month) to eliminate the possibility of contribution to the sample activity due to ^{202}Tl. Chemical yield is determined by taking the sum of the counts of the appropriate X-ray energy for each sample, correcting for background, and taking the ratio of corrected count-rates for the sample and the tracer. Errors in this method are generally less than 10 percent.

Alpha-particle pulse-height analysis is performed on the uncovered chemical sample and tracer sample using the same detector for each. This is to determine the presence of contaminating alpha-particle activities--none were observed. Following this step, both samples are counted in the same proportional counter to obtain bulk count-rates. The chemical yield is determined by taking the ratio of the sample and tracer activities--each of which has been corrected for the appropriate background (typically 1-2 cpm). The error in the chemical yield is generally less than 10 percent.

The chemical yields of platinum and lead are determined by X-ray Fluorescence Analysis. This analysis was performed by R. D. Giauque of Lawrence Berkeley Laboratory. Standards are first evaporated onto pre-cut filter papers approximately the same size as the chemical sample spot, then mounted on an aluminum counting card as closely as possible to the same arrangement as that used for the chemical sample. No precipitations or other chemistries are performed on the standard so differences do exist between the standard and the chemical sample. The counting cards of the standard and sample are arranged as closely as possible to the same position within the spectrometer. The chemical yield is determined by taking the ratio of the counts from the sample and standard for equivalent measurements. It should be noted that there is a substantial undeterminable error involved in this method. This arises both from differences between sample and standard preparation and, in the platinum-iridium samples, possible iridium "contamination" of platinum X-rays due to difficulties in resolving iridium and platinum X-rays. This error will not affect the relative yields within platinum or lead but may shift the measured cross-sections as a whole up or down in magnitude by some indeterminant factor (see Results section).

The tracers and methods used in the determination of chemical yield for each element are shown in Table 10. Also shown is a typical activity level used. For detection of alpha-particles, this activity represents 51 percent counting geometry. For X-ray and gamma-ray analysis, the activity is for the energy (or energies) given and for counting on shelf "one" with no efficiency correction.

F. Summary

A listing of all samples generated is given in Table 11. The code contains a letter representing the projectile ion (K or X), a letter representing the target (U or T) and a number representing the experiment number for that target-projectile combination. The fourth character in the sample code designates the chemical fraction: N for neptunium, P for plutonium (in uranium experiments only), TP for

Table 10. Chemical Yield Methods used in Uranium and Tantalum Experiments

Sample	Method	Tracer	Energy (MeV)	Count-rate (cpm)
Neptunium	α	Np-237	4.79	100
Plutonium	α	Pu-238	5.50	20
Americium	α	Am-241	5.48	50
Iridium	γ	Ir-192	0.316, others	10,000
Platinum	X-ray Fluorescence			
Gold	γ	Au-195	0.099	1000
Mercury	γ	Hg-203	0.279	1000
Thallium	K_α X-ray	Tl-204	0.078, 0.069	7000
Lead	X-ray Fluorescence			
Bismuth	γ	Bi-207	0.569, others	5000

Table 11. Chemical Samples Generated in Each Experiment.

Experiment	Samples
KU3	KU3N, KU3P, KU3TP
KU4	KU4N, KU4P
XU5	XU5N, XU5P, XU5TP
KT3	KT3A, KT3H, KT3P
KT4	KT4A, KT4B
KT5	KT5A, KT5B
KT6	KT6A, KT6B
KT7	KT7T, KT7L, KT7B
KT8	KT8A, KT8B
XT2	XT2A, XT2H, XT2P
XT4	XT4T, XT4L, XT4B
XT7	XT7A, XT7B
XT8	XT8A, XT8B
XT9	XT9A, XT9B

tranplutonium, P for platinum-iridium (in tantalum experiments), A for gold, H for mercury, T for thallium, L for lead, and B for bismuth.

A listing of typical chemical yields is given in Table 12. These values represent average chemical yields. Chemical yields of samples varied primarily with the difficulty of forming the Ta_2O_5 precipitate.

Table 12. Average Chemical Yeilds for Chemical Fractions.

Sample	Yield (%)
Np	75
Pu	25
TP	20
Ir	20
Pt	35
Au (thick target)	30
Au (thin target)	25
Hg	35
Tl	25
Pb	35
Bi (thick target)	20
Bi (thin target)	45

IV. DATA COLLECTION AND ANALYSIS

A. Beta-Particle Detection

Beta-particle detection is performed with gas-flow proportional counters contained within one inch thick lead caves. The detectors are end window type with 1 mg/cm^2, 2.5 cm diameter gold plated mylar used as the window. The central filament is 0.018 mm diameter gold plated tungsten wire. The chamber is made of aluminum. The power supply scaler system is a Model DS-2 Decade Scaler from Nuclear Measurements Corp., Indianapolis, Indiana. Operating voltages are found to be 1900-2000 volts; this is reasonably stable over periods of one to two weeks.

From experiment to experiment and within the counting periods of the samples, the voltage is adjusted to maintain a constant count rate for a ^{36}Cl source. This allows rough comparisons from experiment to experiment. In order to obtain cross-sections and allow more reliable comparisons, an efficiency calibration is necessary. Rigorous calibrations for self-absorption was not considered very important since all samples are weightless. Further, correction of efficiencies for differences in sample diameter are not performed. All samples are kept to a minimum size—usually 1.5 cm or less in diameter.

An approximate efficiency calibration was performed as follows. β^- calibration sources were obtained from New England Nuclear, Boston, Mass. (See Table 13). These are thin samples evaporated onto 1 mg/cm^2 aluminized mylar and covered with another piece of aluminized mylar. This arrangement is supported by a thin metal ring

Table 13. β^- Calibration Sources*

Source	$t_{1/2}$(yr.)	$E_{\beta^-,max}$(MeV)	Activity (microcuries)	Date
C-14	5730	0.16	0.138	12/76
Cl-36	3.0×10^5	0.74	0.0189	04/01/76
Sr-90, Y-90	28.5	0.55, 2.27	0.0210	04/09/76
Tc-99	2.1×10^5	0.29	0.037	04/02/76
Pm-147	2.6	0.22	0.077	04/01/76

---

*obtained from New England Nuclear, Boston, Massachusetts.

of 24 mm outer diameter and is not secured to a backing, allowing use in the experimenter's counting systems. Source calibration is performed to an error of less than 6 percent by New England Nuclear, using National Bureau of Standards references. To allow equivalent backscattering from the samples and the standards, the sources are mounted in the same manner as the experimental samples and are counted on the same shelves used in the experiments. After these data have been obtained, efficiencies are determined by taking the ratio of the observed count rate versus the disintegrations per minute on the date that count was taken. In the case of the ^{90}Sr-^{90}Y source, an efficiency for ^{90}Sr is interpolated from the graph of the efficiencies calculated from data obtained from the remaining β-calibration sources. This allows the estimation of the efficiency for ^{90}Y. Once efficiencies are calculated as a function of energy, this information is plotted; efficiencies for isotopes in experimental samples were obtained by reading from the graph the efficiency corresponding to the tabulated β^-energy. An example of such an efficiency curve is shown in Figure 15. Admittedly, this is a rather simplistic approach to obtaining beta-particle detection efficiences and significant errors can be introduced. However, it should be kept in mind that the primary purpose of the detection of beta-radiation in these experiments is the observation of an unknown beta-particle activity with cross-section determination being a secondary objective and subject to comparison with gamma-ray analysis.

All samples for beta-particle detection are prepared in the same manner. The counting cards used are flat aluminum plates, 8.8 x 6.3 x 0.16 cm, with a cross-hair marking representing the center of the card. To the center of this card is secured a piece of double backed adhesive tape. The sample itself is prepared by evaporation onto a 0.051 mm thick, 2.5 cm diameter platinum disk followed by heating to red-heat in the flame of a Bunsen burner. The platinum disk is placed, sample side up, onto the adhesive tape so that the sample spot is centered on the plate. The sample is then covered by one thickness of approximately 1 mg/cm^2 saran wrap. No further coverings or absorbers are placed either above or below the sample and card.

B. Gamma-Ray Counting

All gamma-ray analysis is performed using one of two ORTEC coaxial-germanium lithium drifted diode (Ge(Li)) detectors. Ge(Li)3 has an active volume of 60 cm^3 and Ge(Li)4 has an active volume of 90 cm^3. Detector resolutions are given in Table 14. Each detector is housed in an ~1 m^3 volume "cave" to lessen natural background contributions and prevent contamination of the spectra by other samples in the counting room. The cave is constructed of 5 cm of lead lined with 0.3 cm of steel and 0.3 cm of aluminum to reduce the contribution due to induced fluorescence in the lead. Each detector and its respective pre-amplifier are connected to linear amplifiers and then to a pulse-height analysis system built at Lawrence Berkeley Laboratory. These pulse-height analysis systems consist of a Texas Instruments 960A minicomputer, Northern Scientific NS-621 or NS-623

Table 14. Detector Resolution (FWHM) for Ge(Li)3 and Ge(Li)4

Detector	122.1 keV	661.6 keV	1332.5 keV
Ge(Li)3	1.37	1.71	2.09
Ge(Li)4	0.96	1.39	1.83

analog-to-digital convertor, 4096 channels of memory for storage and an Ampex magnetic tape deck. All measurements of a given sample are performed on only one detector.

In order to use the computer based analysis system it is necessary to have accurate energy and efficiency calibrations. These calibrations are determined using a National Bureau of Standards Mixed Radionuclide Gamma-Ray Emission Rate Point-Source Standard (SRM-4215F, 1978). The nearly point source contains the activities shown in Table 15. This source is counted on each shelf of each detector for periods of time long enough to give less than 10 percent error in count-rate.

These calibrations are processed using the computer program SAMPO.[85,86] This program determines photopeak centroids in the calibration spectra and calculates peak shape information for use in later analysis of experimental data by SAMPO. The centroid locations of the gamma-ray peaks are fit to a third-degree polynominal by least-squares analysis to obtain the energy-channel calibration. The pulse-height analysis system is particularly linear with only small contributions arising from the second and third degree terms in the polynominal. A sample energy calibration is shown in Table 16.

Efficiency calibrations are carried out for all possible geometries for each detector using the NBS standard. The resulting fits of the gamma-ray peaks from SAMPO give the count-rate for each gamma-ray line in the standard. This information combined with the reported activity of the standard reference material gives absolute efficiency as a function of energy for each shelf of each detector.

Table 15. Gamma-Ray Calibration Source Information*

Nuclide	$t_{1/2}$	Energy (MeV)	Activity (/min)
Cd-109	463.9d	0.088	3.34×10^4
Co-57	272.4d	0.122	5.96×10^4
Ce-139	137.7d	0.166	3.58×10^4
Hg-203	46.6d	0.279	1.13×10^5
Sn-113	115.0d	0.392	1.07×10^5
Sr-85	64.9d	0.514	1.79×10^5
Cs-137	30.0y	0.662	9.24×10^4
Y-88	106.7d	0.898	6.64×10^5
Co-60	5.27y	1.173	2.35×10^5
Co-60	5.27y	1.332	2.36×10^5
Y-88	106.7d	1.836	6.95×10^5

---

*obtained from National Bureau of Standards, dated 09/01/78

Table 16. Sample Energy Calibration

Spectrum channel X and energy E (keV)

$E = -1.1975 + 0.49953X + 1.82201 \cdot 10^{-7} X^2 + 1.06606 \cdot 10^{11} X^3$

E(gamma)	X	E(Calc)
88.03	178.53	87.99
122.06	246.65	122.02
165.80	334.31	165.82
279.21	561.09	279.14
391.7	786.22	391.66
513.98	1030.9	513.97
661.64	1326.2	661.62
898.0	1798.8	898.00
1173.21	2348.7	1173.2
1332.48	2666.9	1332.5
1836.1	3672.1	1836.1

The efficiencies for each shelf are fit using least-squares analysis to the following equation:

$$\text{Efficiency} = P(1) \times \left(E^{P(2)} + P(3) \times e^{P(4)\times E}\right)$$

as in Reference 85. This method of analysis yields errors in efficiencies of less than 3 percent. Efficiency parameters for shelf 1 of each detector are given in Table 17 and efficiency curves for several geometries of each detector are given in Figures 16 and 17. It should be noted here that sample placement corresponding to the same shelf numbers of the two detectors are not the same distance from the detector face. For example, shelf 1 of Ge(Li)3 is 0.4 cm and shelf 1 of Ge(Li)4 is 1.5 cm from the detector face. For this reason, even though Ge(Li)4 has the higher intrinsic efficiency, Ge(Li)3 allows closer placement of the sample to the detector and therefore higher practical efficiency. This is partly compensated for in Ge(Li)4 by the higher resolution.

Experimental samples for the measurement of the intensities of gamma-rays are mounted in the same manner as with the beta-particle counting. Samples were placed at distances from the detector so that ADC dead-time was <15 percent, and moved to closer shelves when dead-time is <5 percent. Most samples are of very low count-rate allowing placement near the detector. For most samples this means that the first counts are taken on shelf 2 or 3 followed by movement to shelf 1 as soon as possible. The errors due to counting this close to the

Table 17. Efficiency Parameters for Shelf 1.

Detector	P(1)	P(2)	P(3)	P(4)
Ge(Li)3	35.84	-1.144	-0.06420	-0.03400
Ge(Li)4	11.30	-1.005	-0.01703	-0.03757

for Efficiency = $P(1) \times (E^{P(2)} + P(3) \times e^{P(4) \times E})$

detector are deemed acceptable when compared to the advantages of having the higher efficiencies. The details of the counting procedure and errors involved in the methods mentioned above are discussed in somewhat more detail in References 58 and 88. Samples are counted for a maximum of one to two weeks after the irradiation for the chemically pure fractions and for as long as a month after irradiation for the more complex fractions. As many as 15 to 30 counts are made of a given sample, depending on its complexity, with count times ranging from 10 minutes to 24 hours.

Typically, samples in this study were of low activity. For this reason, the background of each system was checked by a two day count with no sample inside the cave. The gamma-ray lines observed due to background were assigned to the natural thorium and uranium chains, ^{226}Ra and daughters, ^{178m2}Hf, ^{40}K, and ^{137}Cs. Wherever necessary, the radiation due to these activities was subtracted from that in the samples.

C. Alpha and X-ray Counting

Most chemical yield determinations are performed through the use of the gamma-ray spectra of samples containing gamma-ray emitting tracers. However, three chemical samples contain tracers with no suitable gamma-rays for use in chemical yield determinations, i.e. no gamma-rays, or a gamma-ray of very low intensity or insufficient energy (<100 keV) to allow distinction from X-rays that may be present. In these cases, K_α X-rays or alpha-radiation are observed for the tracer.

For neptunium and plutonium, ^{237}Np and ^{238}Pu are used as tracers. Their primary radiations are alpha-particles. For chemical yield determination, a combination of pulse-height analysis and proportional counting is used. At some long time after bombardment (typically greater than one month to allow decay of all other possible alpha-particle emitters that might contribute to activity in the sample) the sample is analysed by pulse-height analysis using gold plated surface barrier detectors from ORTEC, Inc. These detectors have an active area of approximately 100 mm^2. The detectors are connected through a pre-amplifier to a TranLamp-linear amplifier, then to a biased amplifier and a Northern Scientific NS-610, 1024 channel pulse-height analyser. An energy calibration is obtained through use of ^{241}Am, ^{244}Cm, and ^{233}U sources. Efficiency calibrations are not necessary since only ratios of integrated counts in the peaks in the spectra are used. In counts ranging from two to eight hours in length, no contaminating activity has been observed. The chemical yield is determined by taking the ratio of integrated counts in a given peak from analysis of the tracer and the sample. This ratio is checked by use of a Fission Alpha Preset Counter, a windowless proportional counter, which gives the bulk count-rate of the sample. Ratios obtained in this manner are in good agreement with those from pulse-height analysis. The samples are prepared for alpha-particle analysis by removing the saran wrap cover and removing the platinum disk from the counting card. As mentioned earlier, all samples are essentially weightless.

The chemical yield of thallium is determined by X-ray analysis of the tracer, ^{204}Tl, through observation of the mercury X-rays from the 2.6 percent electron capture branch of the decay. The detector used for this is a 0.5 cm^3 intrinsic germanium detector. The detector is routed through its associated amplifier to another Northern Scientific NS-610 pulse-height analyser. The energy calibration is adjusted through use of various sources to approximately 0.1 keV per channel. An efficiency calibration is not necessary since only the ratio of identical lines is of interest. Chemical yield is determined by taking the ratio of integrated counts adjusted for background of a given line in the spectra of the experimental sample and the tracer sample. The samples are prepared for counting as similarly as possible to allow reproducible conditions for the X-ray detection. The only observable X-ray activity in the thallium fraction is a result of ^{204}Tl decay. Due to the relatively large amount of ^{204}Tl used and the length of time after irradiation that the X-ray count was performed, there is no significant contribution to the mercury X-rays from the 12.2 day decay of ^{202}Tl.

D. Data Analysis

The data from beta-particle counting are the easiest to analyse. Once all the data has been accumulated, decay curves of logarithm of count-rate versus time-after-bombardment are constructed. Examples of the decay curves for neptunium and plutonium samples from the reaction of ^{86}Kr with uranium are given in Figures 18 and 19. The plutonium sample activity is observed to decay to a constant background. This background is composed of natural or detector background (~10 cpm), counts due to alpha-particles from the ^{238}Pu tracer (~20 cpm), and any counts due to the β^--decay of ^{241}Pu. Therefore, the usual successive subtractions are performed (see, for example, Reference 87) starting with the observed background. This analysis yields reliable results for ^{243}Pu with some indication of decay of ^{245}Pu (see Results section). There is no indication of any other component.

In the case of beta-particle counting of neptunium samples, the count-rate due to ^{239}Np nearly obscured all other activities. In one experiment, the decay of ^{239}Np was followed for up to eight half-lives before any contribution due to background was observed. In all other experiments, counting was terminated after one to two weeks and the subtractions were performed starting with the 2.36 day decay of ^{239}Np. The only other activity observed repeatedly via this method was ^{240}Np. In some experiments, conditions were such that there was indication of the decay of 7.4 minute ^{240m}Np. No other activities were observed in any of the experiments.

No corrections are made in beta-particle decay curve analysis for detector dead-time. Experience with the system used here has shown that no corrections are necessary at count-rates below approximately 5×10^5 counts per minute. All samples from irradiations for short-lived activities had count rates lower than this value.

Analysis of the gamma-ray spectra generated in this work is somewhat more involved. A flow chart of the procedure used is shown in Figure 20. The following paragraphs will give a brief description of the procedures used; however, more detailed descriptions of the various computer programs may be found in References 58 and 88.

Following each gamma-ray count, the gamma-ray spectrum, a forty character label, the count time, and the start and stop time and day of the count are recorded onto magnetic tape This magnetic tape serves as input data for the computer program SAMPO.[85] From ten to thirty spectra each for two to six samples are stored on tape for future processing with SAMPO.

A sample gamma-ray spectrum is shown in Figure 21. The energy calibration, as mentioned earlier, is about 0.5 keV per channel with the maximum energy at about 2 MeV. This spectrum represents a 30 minute count of a chemically separated thallium sample from the reaction of ^{86}Kr with tantalum. The count was taken approximately three and one-half hours after the end-of-bombardment.

A modified version of the computer program SAMPO is used for most gamma-ray data analysis. All spectra are checked for correct input information prior to computer analysis. Card input to SAMPO includes peak fit information, energy calibration, efficiency calibration, time of end-of-bombardment, and information concerning each spectrum. This information includes shelf number of the count, code word for the sample and any corrections to the magnetic tape information that may be necessary.

Given this information, the automatic version of SAMPO reads each spectrum from tape and searches the spectrum for possible peaks. The code then fits these peaks with a Gaussian and with independent exponential tails on the high and low energy ends of the Gaussian. The peak shape information as a function of energy is placed into the program by punched card so that the shape of a given gamma-ray peak is determined by linear interpolation between the calibration points. Also, the code applies a smoothly varying background to the region. Having done this, the code determines the peak area giving the total counts in the peak corrected for background contributions. For each spectrum, a table of results is generated which contains the peak centroid channel and energy, total counts in the peak, peak area corrected for background, and count-rate corrected for detection efficiency for each gamma-ray line. Furthermore, the error associated with each determination is listed. This table of results can be obtained on paper if desired. SAMPO automatically generates microfiche output containing results of the peak search, a picture of the fitting of each peak, and the table of results for each spectrum.

SAMPO also generates a magnetic tape output for use in further data analysis. A file containing elapsed time after the end-of-bombardment to the midpoint of the count period, peak energy and count-rate (previously corrected for efficiency), and the sample code word is generated for each spectrum. This magnetic tape is then submitted for analysis by the computer program TAU1.

TAU1 is a sort program resulting in data for decay curves. Since the spectra are collected in chronological order, no further sorting by time-after-bombardment is necessary. The code first sorts by sample code collecting all data for the same sample. Once this is accomplished, the program sorts by energy, keeping data for any energy peak which was found in two or more spectra of that sample. Having completed this, a decay curve is constructed and estimates are made of the half-life and initial activity for a one and two component decay. This procedure is followed for each sample. A summary of the results is written to paper and the decay curve construction is written to magnetic tape for further analysis.

The next step of the analysis is to identify each gamma-ray line in the sample. This is done by use of the interactive computer code TAU2. The program combines the results from TAU1 with the gamma-ray table prepared by Binder, et al.,[89] both of which are on magnetic tape. The Binder table is a combination of an earlier version compiled from the literature and the Bowman-MacMurdo table.[90] TAU2 then displays a semilogarithmic plot of the count-rate (in gamma-rays per minute) versus the time-after-bombardment on a Tektronix 4014 graphics terminal. Also listed on the display is a segment of the gamma-ray table containing twenty gamma-ray lines nearest in energy to the energy of that represented by the decay curve. An example of one of these displays is shown in Figure 22. TAU2 allows the user to choose one, two, or three of these lines for use in fitting the decay curve. Decay curves may also be fit with background plus one half-life, growth and decay of a single gamma-ray line, or a half-life not listed in the gamma-ray table. In this work, choice of components is relatively easy since all samples have been chemically separated.

Once a suitable fit to the decay curve has been found and accepted, the display is recorded on microfiche and punched cards are generated. A punched card is generated for each half-life used in the fit. This card contains the designation of the isotope, half-life, known energy and abundance of the gamma-ray line, the observed energy, the sample code, the initial activity (A_0), and the error in A_0. The A_0 value has been corrected for the gamma-ray abundance and thus is in decays per minute. After all decay curves for a given sample have been analyzed, all cards are combined for use in the final step of the analysis.

The final step of the analysis involves calculation of cross-sections. First, all TAU2 cards from a given sample are sorted by energy, and cross-sections are calculated for each line observed. This is more of a bookkeeping step to allow observation of multiple identifications. Finally, the TAU2 cards are sorted by nuclide and the weighted average A_0 is determined. The cross-sections are calculated from the average A_0 values by the equation:

$$\sigma = A_0/N \sum_{i=1}^{n} \phi_i(1-e^{-\lambda t_{bi}}) \left\{\exp - \lambda\left(\sum_{j=i+1}^{n} t_{bj}\right)\right\}$$

This allows for fluctuating beam intensity. N is the number of target atoms per cm^2. ϕ_i is the beam intensity in the i^{th} period of length t_{bi}. The summation over t_{bj} is the time remaining between the end of the i^{th} interval and the end of the irradiation. The error in the cross-section is calculated as well.

Error in the cross-section is determined by standard methods of propagation of errors. The only value in the cross-section calculation which has an error associated with it is the value of A_0. The error in A_0 results from error in count-rate, error in detection efficiency, and error in the decay curve analysis. The details of the error calculations may be found in References 58, 85, 86, and 88.

A review of the results of this calculation is made to account for multiple uses of the same gamma-ray line and to account for individual lines of each nuclide which vary significantly from all other lines of the same nuclide. Also, a check is made of the gamma-ray intensities against those in the Table of the Isotopes[91] and the GSI Gamma-Ray Table.[92] Corrections of intensity, and therefore count-rate, are made as necessary. (Since this work was completed, the Binder table has undergone major revisions as necessitated by the more recent compilations.) When all "bad" identifications have been accounted for or removed, the cross-section calculation is performed again. The final results are corrected for chemical yield and the error in the cross-section is adjusted for the error in the chemical yield.

In this work, most nuclide cross-sections are based on the observation of two or more gamma-ray lines. The largest number of lines observed for a given nuclide is approximately thirty-five for ^{191}Au. Isotope identifications relying on one observed gamma-ray line are based on one component or obvious two component fits to the decay curves. Also, other possible lines for that nuclide are searched out and explanations as to why they were not observed are found. Other such identifications that did not meet these criteria are rejected. Results of the above analysis will be shown later in this work.

In some cases, particularly in low activity samples, SAMPO can not fit many of the gamma-ray lines of interest due to low activity or poor peak shape. Hand analysis of these data is necessary. Here, the number of measured counts in the energy region of the spectrum representing the gamma-ray are summed. An average background is determined from the number of counts in a few channels above and below this region; this background is subtracted from the summed counts in the region and a count-rate is determined. A_0 values are determined graphically by extrapolation of the decay curve due to the gamma-ray line back to the time of the end-of-bombardment. Cross-sections are calculated in the usual manner. This method proves useful in the count-rate range of approximately 0.5 to 1.5 counts per minute. Count-rates much lower than this are used primarily for the determination of upper-limits unless a very definite decay is observed.

V. RESULTS

A. Uranium Targets

Experimental results from the reactions of ^{86}Kr and ^{136}Xe ions with uranium nuclei are given in Tables 18 and 19 respectively. Experimental production cross-sections, in millibarns, are given for the indicated nuclides. Error in the cross-section is given in millibarns. Also listed is the method of determination of each nuclide production cross-section. All identifications from gamma-ray analysis are based on chemical fraction (Z identification), gamma-ray energy, and half-life. Identifications from beta-particle detection data are based on chemical fraction and half-life and are confirmed by gamma-ray analysis wherever possible. ^{239}Np and ^{240m}Np are not included in the tables or figures due to the large contribution to their measured radioactivity from their radioactive parents--^{239}U and ^{240}U. ^{237}Pu is determined by observation of the K_{α} X-rays of neptunium in the gamma-ray spectra. The energy of the 60 kev gamma-ray line of ^{237}Pu is below the threshold of the analyser system and consequently is not observed. For calculation of a cross-section, an intensity of 20 percent is used[91] for the $K_{\alpha 1}$ neptunium X-ray arising from the electron capture decay of ^{237}Pu.

Analysis of the decay curves from detection of beta-particles emitted by plutonium isotopes in the plutonium chemical fraction gave no indication of a short-lived or unidentified radioactivity. Due to high levels of activity in the neptunium fraction from ^{239}Np and ^{240}Np decay, no other activities were clearly identifiable from the

Table 18. Thick Target Cross-Sections for ^{86}Kr + ^{238}U. Incident Energy = 731 MeV (lab) (from Experiments KU3 and KU4).

Nuclide	Method of Determination	Cross-Section (mb)	Error (mb)
Np-234	γ	5.0×10^{-2}	1.6×10^{-2}
Np-236m	γ	6.6×10^{-1}	1.4×10^{-1}
Np-238	γ	4.4×10^{0}	0.5×10^{0}
Np-239	γ, β^-	(a)	
Np-240	γ, (β^-)	6.8×10^{-1}, (2.2×10^{-1})	1.3×10^{-1}
Np-240m	γ, β^-	(b)	
Pu-237	γ	2.3×10^{-2}(c)	5.8×10^{-3}
Pu-243	γ, (β^-)	3.7×10^{-3}, (6.1×10^{-3})	1.2×10^{-3}
Pu-245	β^-	$\sim 10^{-4}$(d)	
Am-239	γ	6.4×10^{-3}	1.6×10^{-3}
Am-240	γ	1.8×10^{-2}	2.5×10^{-3}
Am-244	γ	3.0×10^{-3}	1.0×10^{-3}

(a) Cross-section not calculated due to large contribution due to feeding from ^{239}U. Cross-section estimated at 10-20 mb.

(b) Cross-section not calculated due to growth from parent ^{240}U.

(c) K_α X-rays observed in gamma-ray analysis.

(d) Upper-limit.

Table 19. Thick Target Cross-Sections for $^{136}Xe + ^{238}U$. Incident Energy = 1156 MeV (lab) (from Experiment XU5)

Nuclide	Method of Determination	Cross-Section (mb)	Error (mb)
Np-234	γ	1.3×10^{-2}	4.0×10^{-3}
Np-238	γ	1.2×10^{0}	1.1×10^{-1}
Np-239	γ, (β^-)	(a)	
Np-240	γ, (β^-)	4.5×10^{-1}	5.0×10^{-2}
Np240m	γ, (β^-)	(b)	
Pu-243	γ, (β^-)	1.0×10^{-2}	2.2×10^{-3}
Pu-245	γ	$3.6 \times 10^{-4(c)}$	1.8×10^{-4}
Am-239	γ	5.1×10^{-3}	1.3×10^{-3}
Am-240	γ	1.3×10^{-2}	2.2×10^{-3}
Am-244	γ	2.8×10^{-3}	1.0×10^{-3}

(a) Cross-section not calculated due to unknown (but large) amount of feeding from ^{239}U.

(b) Cross-section not calculated due to feeding from ^{240}U.

(c) Use only as an upper-limit.

detection of beta-particles. Under the best of conditions, ^{240m}Np was observed. For these reasons, it was essentially impossible to detect a new neptunium beta-particle emitter with a half-life of less than one hour from these experiments.

Graphs of mass number of a nuclide versus the measured cross-section for that nuclide are shown in Figures 23 and 24. The dashed curves have been drawn to aid the eye and are approximations only. The true distribution of neptunium should be a superposition of two distributions—that from quasi-elastic transfer and that from deep inelastic. There are not enough data in this work to resolve such a distribution.

B. Thick Tantalum Targets

Experimentally determined production cross-sections for the reactions of ^{86}Kr and ^{136}Xe ions with thick tantalum targets are given in Tables 20 and 21. Cross-sections in millibarns are tabulated by nuclide. Errors in the cross-sections are also given in millibarns. Also listed for each nuclide is the number of gamma-ray energies observed which could be clearly identified as due to that nuclide. For many nuclides, other gamma-ray energies are observed which are not clearly identifiable as due to that particular radioactivity.

The last column in each of these tables contains a cross-section which has been corrected for feeding from the parent during the irradiation, and between the end-of-bombardment and the time the daughter is separated from the parent. Equations from Reference 93

Table 20. Thick Target Cross-Sections from the Reaction of ^{86}Kr ions with ^{181}Ta. Incident Energy = 731 MeV (lab) (from experiments KT3 and KT7).

Nuclide	No. Lines Observed	Cross-Section (mb)	Error (mb)	Corrected Cross-Section (mb)
Ir-183	2	Observed$^{(a)}$		
Ir-184	5	1.25×10^{0}	1.26×10^{-1}	1.2×10^{0}
Ir-185	4	1.18×10^{0}	1.20×10^{-1}	1.2×10^{0}
Ir-186	6	9.86×10^{-1}	9.99×10^{-2}	9.1×10^{-1}
Ir-186m	6	1.40×10^{0}	2.33×10^{-1}	(e)
Ir-187	4	2.70×10^{0}	2.84×10^{-1}	1.8×10^{0}
Ir-188	3	1.97×10^{-1}	5.57×10^{-1}	
Ir-190	3	6.46×10^{-1}	4.92×10^{-1}	6.4×10^{-1}
Ir-190m2	1	1.44×10^{-2}	3.55×10^{-3}	(e)
Pt-185A	2	Observed$^{(a)}$		
Pt-186	2	Observed$^{(a)}$		
Pt-187	3	6.21×10^{0}	$1.87 \times 10^{0(b)}$	$1.8 \times 10^{0(c)}$
Pt-188	4	6.99×10^{0}	$2.09 \times 10^{0(b)}$	$1.8 \times 10^{0(c)}$
Pt-189	6	$1.05 \times 10^{+1}$	$3.14 \times 10^{0(b)}$	$2.2 \times 10^{0(c)}$
Pt-191	3	1.12×10^{0}	$3.37 \times 10^{-1(b)}$	(d)
Au-189	3	Observed$^{(a)}$		
Au-190	5	1.61×10^{0}	1.62×10^{-1}	1.5×10^{0}
Au-191	36	8.77×10^{-1}	8.78×10^{-2}	5.3×10^{-1}
Au-192	12	4.28×10^{-1}	4.29×10^{-2}	1.5×10^{-2}

Table 20. (continued)

Nuclide	No. Lines Observed	Cross-Section (mb)	Error (mb)	Corrected Cross-Section (mb)
Au-193	4	2.22×10^{-1}	2.25×10^{-2}	5.2×10^{-2}
Au-194	1	2.23×10^{-2}	4.41×10^{-3}	(e)
Hg-191	3	3.45×10^{-1}	5.69×10^{-2}	3.4×10^{-1}
Hg-192	3	6.31×10^{-1}	8.09×10^{-2}	6.2×10^{-1}
Hg-193m	9	1.52×10^{-1}	1.57×10^{-2}	(e)
Hg-195	5	9.91×10^{-2}	1.27×10^{-2}	1.4×10^{-2}
Hg-195m	1	2.87×10^{-2}	5.74×10^{-3}	(e)
Hg-197m	1	4.42×10^{-1}	2.84×10^{-1}	(e)
Tl-192	2	Observed(a)		
Tl-193	4	Observed(a)		
Tl-194	2	5.83×10^{-2}	7.05×10^{-3}	5.0×10^{-2}
Tl-194m	2	5.77×10^{-2}	6.01×10^{-3}	(e)
Tl-195	6	1.22×10^{-1}	1.22×10^{-2}	1.1×10^{-1}
Tl-196	4	6.30×10^{-2}	6.45×10^{-3}	4.8×10^{-2}
Tl-196m	2	4.49×10^{-2}	4.60×10^{-3}	(e)
Tl-197	8	1.02×10^{-1}	1.03×10^{-2}	6.8×10^{-2}
Tl-198	8	4.29×10^{-2}	4.34×10^{-3}	4.6×10^{-3}
Tl-198m	2	1.83×10^{-2}	2.00×10^{-3}	(e)
Tl-199	4	3.44×10^{-2}	3.47×10^{-3}	7.9×10^{-4}(d)
Tl-200	2	3.47×10^{-3}	3.49×10^{-4}	9.7×10^{-4}(d)
Tl-201	1	5.83×10^{-3}	7.21×10^{-4}	(d)

Table 20 (continued)

Nuclide	No. Lines Observed	Cross-Section (mb)	Error (mb)	Corrected Cross-Section (mb)
Bi-200	2	1.67×10^{-2}	1.78×10^{-3}	1.2×10^{-2}
Bi-201	2	Observed		
Bi-202	3	1.94×10^{-2}	2.03×10^{-3}	1.7×10^{-2}
Bi-203	3	1.15×10^{-2}	4.09×10^{-3}	8.4×10^{-3}
Bi-204	4	5.22×10^{-3}	5.41×10^{-4}	2.8×10^{-3}
Bi-205	3	3.75×10^{-2}	1.83×10^{-2}	(d)
Bi-206	1	1.71×10^{-2}	1.26×10^{-2}	(d)

(a) Absolute gamma-ray intensities for these nuclides are not known. However, decay of each nuclide's gamma-ray energies was observed with the reported half-life.

(b) Reported errors in platinum isotope cross-sections are based on an assumed 30% error in the chemical yield as determined by X-ray Fluorescence Analysis.

(c) Values of the experimentally determined cross-sections for platinum isotopes have been multiplied by 0.29 before calculation of feeding correction to conform with cross-sections for gold and iridium isotopes. See text for explanation.

(d) Value of the experimental cross-section is consistent with all observed radiation of this nuclide arising from decay of its parent during the irradiation and before separation from its parent. Corrected cross-sections have values near or below zero.

(e) No feeding correction due to stable parent, very long-lived parent, or no known parent.

Table 21. Thick Target Cross-Sections from the Reaction of ^{136}Xe ions with ^{181}Ta. Incident Energy = 1156 MeV (lab.)(from experiments XT2 and XT4).

Nuclide	No. Lines Observed	Cross-Section (mb)	Error (mb)	Corrected Cross-Section (mb)
Ir-183	2	Observed(a)		
Ir-184	3	1.44×10^{-1}	1.48×10^{-2}	1.4×10^{-1}
Ir-185	3	3.30×10^{-1}	3.51×10^{-2}	3.3×10^{-1}
Ir-186	5	2.28×10^{-1}	2.38×10^{-2}	1.4×10^{-1}
Ir-186m	2	9.44×10^{-1}	9.59×10^{-2}	(e)
Ir-187	7	9.47×10^{-1}	9.49×10^{-2}	6.2×10^{-1}
Ir-188	4	4.18×10^{-1}	4.86×10^{-2}	4.0×10^{-1}
Ir-189	1	6.10×10^{-2}	1.33×10^{-1}	(d)
Ir-190m2	1	3.41×10^{-3}	1.27×10^{-3}	(e)
Pt-185A	2	Observed(a)		
Pt-185B	3	Observed(a)		
Pt-186	2	Observed(a)		
Pt-187	3	1.51×10^{-1}	4.81×10^{-2}(b)	1.9×10^{-1}(c)
Pt-188	4	2.99×10^{-1}	9.00×10^{-2}(b)	4.1×10^{-1}(c)
Pt-189	5	3.94×10^{-1}	1.18×10^{-1}(b)	4.2×10^{-1}(c)
Pt-191	3	1.48×10^{-1}	4.74×10^{-2}(b)	7.5×10^{-2}(c)
Au-189	4	Observed(a)		
Au-190	5	6.44×10^{-1}	6.45×10^{-2}	4.7×10^{-1}
Au-191	26	4.47×10^{-1}	4.60×10^{-2}	3.7×10^{-1}

Table 21 (continued)

Nuclide	No. Lines Observed	Cross-Section (mb)	Error (mb)	Corrected Cross-Section (mb)
Au-192	8	2.47×10^{-1}	2.48×10^{-2}	1.4×10^{-1}
Au-193	5	1.57×10^{-1}	1.58×10^{-2}	1.5×10^{-1}
Au-194	2	6.73×10^{-2}	6.78×10^{-3}	(e)
Au-196	2	8.33×10^{-3}	8.62×10^{-4}	7.5×10^{-3}
Au-196m	1	6.06×10^{-3}	6.30×10^{-4}	(e)
Hg-191	4	1.51×10^{-1}	1.52×10^{-2}	1.1×10^{-1}
Hg-192	3	3.01×10^{-1}	3.15×10^{-2}	2.66×10^{-1}
Hg-193m	10	1.19×10^{-1}	1.20×10^{-2}	(e)
Hg-195	3	6.31×10^{-2}	1.04×10^{-2}	(d)
Hg-195m	3	5.71×10^{-2}	6.20×10^{-3}	(e)
Tl-192	2	Observed(a)		
Tl-193	3	Observed(a)		
Tl-194m	2	5.41×10^{-2}	6.09×10^{-3}	(e)
Tl-195	4	2.29×10^{-1}	2.30×10^{-2}	2.2×10^{-1}
Tl-196	2	9.44×10^{-2}	9.50×10^{-3}	1.6×10^{-2}
Tl-196m	2	9.92×10^{-2}	1.14×10^{-2}	(e)
Tl-197	5	2.08×10^{-1}	2.10×10^{-2}	1.1×10^{-1}
Tl-198	3	9.09×10^{-2}	9.09×10^{-3}	9.0×10^{-2}
Tl-198m	3	2.79×10^{-2}	3.00×10^{-3}	(e)
Tl-199	4	7.87×10^{-2}	7.38×10^{-3}	6.6×10^{-2}
Tl-200	2	1.28×10^{-2}	1.30×10^{-3}	1.0×10^{-2}

Table 21 (continued)

Nuclide	No. Lines Observed	Cross-Section (mb)	Error (mb)	Corrected Cross-Section (mb)
Tl-201	1	5.02×10^{-2}	1.51×10^{-2}	3.9×10^{-2}(f)
Bi-201	3	Observed(a)		
Bi-202	1	1.16×10^{-1}	1.20×10^{-2}	(g)
Bi-203	2	7.25×10^{-1}	7.29×10^{-2}	(g)
Bi-204	2	2.35×10^{-2}	2.97×10^{-3}	(g)
Bi-205	3	3.18×10^{-2}	4.12×10^{-3}	(g)

(a) See footnote (a) in Table 20.

(b) See footnote (b) in Table 20.

(c) Values of the experimentally determined cross-sections for platinum isotopes have been multiplied by 2.1 before calculation of feeding contributions in order to conform with cross-sections measured for iridium and gold isotopes (see text).

(d) See footnote (d) in Table 20.

(e) See footnote (e) in Table 20.

(f) Upper-limit only.

(g) Attempts at correction of Bi isotope cross-sections failed due to inability to approximate Po isotope cross-sections correctly.

are used for these calculations. The corrected cross-section given in the table only represents an estimate of the true production cross-section of the nuclide. This is because cross-sections for most of the parent radioactivities could not be determined experimentally.

In order to make these corrections for feeding, it is necessary to assume that the parent is not fed by the grandparent. This assumption is approached in this work by making initial corrections to the highest Z within a mass chain and then successively making corrections to the next lower Z. Corrections are first made for bismuth isotopes by assuming a polonium isotopic distribution. This distribution is assumed to have a shape similar to the experimentally determined bismuth isotopic distribution. Further, the polonium peak cross-section is assumed to be ~5×10^{-3} millibarns located at mass 204 (for ^{86}Kr + Ta) and ~1×10^{-1} millibarns at mass 204 (for ^{136}Xe + Ta). These values are arrived at by rough extrapolation of trends observed for isotopes of gold, mercury, thallium, and bismuth. These assumptions prove to be rasonable for the ^{86}Kr reaction but appear to be very bad for the ^{136}Xe reaction (Polonium cross-sections seem to be overestimated). A similar procedure is followed for estimation of lead cross-sections for the calculation of feeding to thallium isotopes. The lead isotopic distribution is again assumed to resemble the bismuth distribution and it is assumed to be located, in peak cross-section and mass, half the difference between the apparent location of the distribution of thallium and bismuth isotopes. Corrections of mercury and gold isotope cross-sections are based on estimates of parent cross-sections determined directly from the corrected parent isotopic distribution or extrapolation of that distribution to the appropriate mass number.

Feeding corrections for platinum isotopes require an additional adjustment. As can be seen in Tables 20 and 21, platinum isotope cross-sections are quite different from iridium and gold isotope cross-sections. This is almost certainly due to the inaccuracy of the chemical yield (see chemical yield determination in the chemistry section). Prior to corrections for feeding, all platinum isotope cross-sections are multiplied by an arbitrary factor which has the effect of shifting the entire isotopic distribution of platinium higher or lower in cross-section. This factor is chosen such that the peak platinum cross-section is between the peak cross-sections of iridium and gold. Following this, calculations are performed for platinum and iridium isotopes in the same manner as for gold and mercury isotopes.

For all of the above reasons, these corrected cross-sections should be taken only as estimates. The errors for these cross-sections are quite large due to the estimation procedure and no attempt is made to determine errors.

Graphs of nuclidic cross-section versus nuclidic mass number for both thick target reactions are shown in Figures 25 and 26. The solid points represent the actual data. The open points represent the corrected cross-sections where these differ from the experimental cross-sections. When an isomeric pair is observed, the sum of the two cross-sections is plotted. The curves represent an "eyeball" fit to the corrected cross-sections.

C. Thin Tantalum Targets

Tables 22-28 contain experimentally determined cross-sections for the reactions of ^{86}Kr and ^{136}Xe with thin tantalum targets. These tables are set up in the same manner as Tables 20 and 21 for thick tantalum targets. The results for ^{86}Kr + ^{181}Ta are shown graphically in Figures 27 and 28. These are plots of nuclidic cross-section versus mass number of the nuclide for each energy. Figure 27 is the graph of gold isotopic cross-sections and Figure 28 is the graph of bismuth isotopic cross-sections. Results for the reaction ^{136}Xe + ^{181}Ta are shown in the same manner in Figures 29 and 30. Energies listed on these graphs are incident energies in the laboratory frame.

Excitation functions for gold and bismuth isotopes from these reactions are shown graphically in Figures 31-34. The energy information for these plots is given in Tables 29 and 30. In these graphs, the cross-section for a given nuclide is plotted versus the energy at which the cross-section is measured. Two energy scales are used. The scale at the bottom is the difference between the Coulomb barrier and the average energy of the beam as it passes through the target in the center-of-mass frame. The scale at the top of the graph is the ratio of the average projectile energy in the target and the Coulomb barrier. The horizontal lines drawn at the bottom of the graphs

Table 22. Thin-Target Cross-Sections $^{86}Kr + ^{181}Ta$ at an Incident Energy of 731 MeV (lab.) (from experiment KT6).

Nuclide	No. Lines Observed	Cross-Section (mb)	Error (mb)
Au-190	3	4.53×10^{-1}	5.08×10^{-2}
Au-191	7	2.89×10^{-1}	5.31×10^{-2}
Au-192	3	9.66×10^{-2}	1.29×10^{-2}
Au-193	2	2.04×10^{-1}	2.54×10^{-2}
Au-194	1	1.85×10^{-2}	2.92×10^{-3}
Bi-200	2	2.15×10^{-2}	2.21×10^{-3}
Bi-202	3	1.02×10^{-2}	4.51×10^{-3}
Bi-203	2	6.89×10^{-3}	1.31×10^{-3}
Bi-204	2	2.53×10^{-3}	5.45×10^{-4}

Table 23. Thin Target Cross-Sections for ^{86}Kr + ^{181}Ta at an Incident Energy of 620 MeV (lab.) (from Experiment KT8).

Nuclide	No. Lines Observed	Cross-Section (mb)	Error (mb)
Au-190	2	9.65×10^{-1}	9.75×10^{-2}
Au-191	8	7.59×10^{-1}	7.95×10^{-2}
Au-192	3	2.93×10^{-1}	3.90×10^{-2}
Au-194	1	3.26×10^{-2}	3.90×10^{-3}
Bi-200	2	6.41×10^{-2}	9.32×10^{-3}
Bi-202	2	3.90×10^{-2}	3.99×10^{-3}
Bi-203	2	1.51×10^{-2}	9.34×10^{-3}
Bi-204	2	9.78×10^{-3}	1.38×10^{-3}

Table 24. Thin Target Cross-Sections for ^{86}Kr + ^{181}Ta at an Incident Energy of 506 MeV (lab.) (from experiment KT4).

Nuclide	No. Lines Observed	Cross-Section (mb)	Error (mb)
Au-190	2	2.80×10^{-1}	3.22×10^{-2}
Au-191	2	3.18×10^{-1}	3.18×10^{-2}
Au-192	2	1.43×10^{-1}	1.44×10^{-2}
Au-193	2	2.91×10^{-1}	3.81×10^{-2}
Au-194	1	3.26×10^{-2}	6.50×10^{-3}
Bi-200	2	3.09×10^{-2}	6.01×10^{-3}
Bi-202	3	1.79×10^{-2}	2.70×10^{-3}
Bi-203	1	$6.34 \times 10^{-2(a)}$	6.82×10^{-3}
Bi-204	1	$1.29 \times 10^{-2(a)}$	6.85×10^{-3}

(a) Use as upper-limits.

Table 25. Thin Target Cross-Sections for ^{86}Kr + ^{181}Ta at an Incident Energy of 394 MeV (lab.) (from experiment KT5)*.

Nuclide	No. Lines Observed	Cross-Section (mb)	Error (mb)
Au-190	1	4.04×10^{-2}	1.11×10^{-2}
Au-191	2	1.29×10^{0}	2.58×10^{-1}
Au-192	1	1.43×10^{-1}	4.82×10^{-2}
Bi-202	2	4.86×10^{-2}	1.29×10^{-2}

* Cross-sections determined as for thick targets since Coulomb barrier is at 389 MeV and target is ~100 MeV thick. See text for explanation.

Table 26. Thin Target Cross-Sections for $^{136}Xe + ^{181}Ta$ at an Incident Energy of 1156 MeV (lab.) (from experiment XT7).

Nuclide	No. Lines Observed	Cross-Section (mb)	Error (mb)
Au-190	6	1.57×10^{-1}	4.38×10^{-2}
Au-191	10	4.88×10^{-1}	8.54×10^{-2}
Au-192	3	3.21×10^{-1}	3.22×10^{-2}
Au-193	3	2.08×10^{-1}	2.15×10^{-2}
Au-194	3	1.43×10^{-1}	6.71×10^{-2}
Bi-200	4	6.56×10^{-2}	1.31×10^{-2}
Bi-202	3	7.95×10^{-2}	1.62×10^{-2}
Bi-203	2	7.15×10^{-2}	2.02×10^{-2}
Bi-204	3	2.92×10^{-2}	5.75×10^{-3}

Table 27. Thin Target Cross-Sections for ^{136}Xe + ^{181}Ta at an Incident Energy of 980 MeV (lab.) (from experiment XT8).

Nuclide	No. Lines Observed	Cross-Section (mb)	Error (mb)
Au-190	3	6.82×10^{-1}	6.95×10^{-2}
Au-191	13	6.10×10^{-1}	6.13×10^{-2}
Au-192	4	3.94×10^{-1}	3.96×10^{-2}
Au-193	3	3.89×10^{-1}	4.02×10^{-2}
Au-194	2	1.15×10^{-1}	2.51×10^{-2}
Bi-200	3	7.97×10^{-2}	1.44×10^{-2}
Bi-202	3	1.35×10^{-1}	3.65×10^{-2}
Bi-203	1	1.92×10^{-1}	7.86×10^{-2}
Bi-204	2	5.52×10^{-2}	1.68×10^{-2}

Table 28. Thin Target Cross-Sections for $^{136}Xe + ^{181}Ta$ at an Incident Energy of 801 MeV (lab.) (from experiment XT9).

Nuclide	No. Lines Observed	Cross-Section (mb)	Error (mb)
Au-190	1	5.11×10^{-2}	5.72×10^{-3}
Au-191	2	6.27×10^{-2}	6.48×10^{-3}
Au-192	2	5.22×10^{-2}	5.82×10^{-3}
Au-193	2	4.14×10^{-2}	7.38×10^{-3}
Au-194	1	4.34×10^{2}(a)	3.92×10^{-2}

No bismuth isotopes observed.

(a) Use as upper-limit.

Table 29. Energy Information for ^{86}Kr Irradiations of Thin ^{181}Ta Targets (Coulomb barrier (B) = 389 MeV (lab)).

Incident Energy MeV (lab)	Energy Drop MeV (lab)	Average Energy MeV (lab)	$E_{Avg}-B$ MeV(c.m.)	E_{Avg}/B
731	69	697	209	1.79
620	70	585	133	1.50
506	82	465	51.5	1.20
394	5[(a)]	391.5	1.69	1.01

(a) Energy drop is from incident energy to the Coulomb barrier.

Table 30. Energy Information for ^{136}Xe Irradiations of Thin ^{181}Ta Targets (Coulomb barrier (B) = 653 MeV (lab)).

Incident Energy MeV (lab)	Energy Drop MeV (lab)	Average Energy MeV (lab)	$E_{Avg}-B$ MeV(c.m.)	E_{Avg}/B
1156	120	1096	253	1.68
980	130	916	150	1.40
801	137	733	45.7	1.12

(labeled Target Thickness) represent the energy range of the projectile for each experiment.

One final point should be made about the thin target experiments. One of the reactions of ^{86}Kr + ^{181}Ta was run at an incident energy slightly above the barrier. The target in this case must be treated as a thick target. The number of target atoms used in cross-section determinations for thick targets is represented by the range of ^{86}Kr from the incident energy to the Coulomb barrier. Since the incident energy is only slightly above the Coulomb barrier, the cross-section becomes extremely sensitive to the calculated value of the Coulomb barrier. The cross-sections listed in Table 25 are calculated using the value of the Coulomb barrier as determined through use of the equation given in the Targets section of the Experimental Methods Chapter. This gives values for cross-sections which seem too high and, therefore, these cross-sections are not shown in the graphs. This will be discussed further in the Discussion section.

No corrections for feeding from parents have been made in thin target cross-sections since there is no information on parent production.

D. Rhenium and Osmium Yields

Table 31 lists relative rhenium and osmium isotope yields from the reactions of both ^{86}Kr and ^{136}Xe with tantalum. Osmium isotopes appear as contaminants of the thallium fraction from the thick target experiments. Rhenium isotopes are observed as contaminants of the

Table 31. Relative Cross-Sections for Rhenium and Osmium Isotopes from the Reactions of ^{86}Kr and ^{136}Xe Ions with Tantalum Targets at 8.5 MeV/A

	^{86}Kr		^{136}Xe	
Nuclide	Cross-Section	Error	Cross-Section	Error
Re-179	—	----	1.37×10^{-2}	3.52×10^{-3}
Re-181	1.00×10^{0}	1.32×10^{-1}	1.00×10^{0}	2.00×10^{-1}
Re-182	2.93×10^{-1}	1.76×10^{-2}	5.7×10^{-1}	6.5×10^{-2}
Re-182m	1.13×10^{-1}	3.40×10^{-2}	—	—
Re-184	8.7×10^{-2}	9.1×10^{-3}	1.74×10^{-1}	2.01×10^{-2}
Os-181m	2.12×10^{-1}	3.00×10^{-2}	7.13×10^{-2}	1.50×10^{-2}
Os-182	1.00×10^{0}	8.69×10^{-2}	1.00×10^{0}	1.1×10^{-1}
Os-183	8.64×10^{-1}	7.75×10^{-2}	6.54×10^{-1}	5.32×10^{-2}
Os-183m	7.34×10^{-1}	9.28×10^{-2}	8.29×10^{-1}	8.10×10^{-2}
Os-185	—	--	8.55×10^{-1}	9.02×10^{-2}

gold fraction from the thin target experiments. However, only cross-sections for rhenium isotopes from the 8.5 MeV/A incident energy projectile experiments are given in the table since these yields are to be compared with thick target experiments at the same incident energy. Since chemical yields are not determined, absolute cross-sections cannot be calculated. For this reason, relative yields are determined for each isotope of the elements. The magnitude of these cross-sections cannot be compared with cross-sections of any other element--only with other isotopes of the same element from the same experiment. Most importantly, however, is that none of this changes the location of the isotopic distribution in Z and A so that peak position may be obtained. Finally, graphs of the rhenium and osmium yields are shown in Figures 35 and 36.

VI. DISCUSSION

A. Uranium Targets

Preliminary experiments indicated the presence of an unidentified short-lived beta-particle emitting activity in the plutonium fraction but this proved to be thorium contamination. Pure plutonium fractions showed no indications of any unknown activities. There was some indication of the presence of ^{245}Pu decay in the beta-particle counting of the plutonium fraction, although no clear 10.5 hour decay was observed. This was the basis for the upper-limit cross-sections given in Tables 18 and 19 for ^{245}Pu. Gamma-ray analysis yielded information on production of ^{237}Pu and ^{243}Pu which allowed an estimation of the isotopic distribution of plutonium.

Observation of new activities in the neptunium sample was virtually impossible using a heavy ion reaction with uranium. This was due to a combination of two factors. First, any new isotope would have been produced in relatively small cross-section. Second, the large count-rates of 7.4 minute ^{240m}Np, 65 minute ^{240}Np and 2.35 day ^{239}Np would have effectively obscured any other half-life occuring at small count-rates. Gamma-ray analysis confirmed the presence of ^{240m}Np, ^{240}Np, and ^{239}Np as well as allowed identification of ^{234}Np and ^{238}Np allowing an approximation of the isotopic distribution of neptunium.

The isotopic distribution of neptunium should be a superposition of two distributions. One distribution would be due to quasi-elastic transfer—the transfer of a very small number of nucleons. This distribution would be very narrow and have a relatively high cross-section. The second distribution, due to deep inelastic reactions, would be a broader distribution with a somewhat lower cross-section. This has been observed for gold isotopes from the reactions of heavy ions with gold.[38,58,94] The effect observed is smaller for a one proton pick-up and even smaller still for a two proton pick-up. Not enough data were obtained in this work to resolve the two components. However, the data did allow estimation of cross-sections.

No attempts were made to find new americium isotopes. Isotopic distributions of americium were determined by gamma-ray analysis. Based on the isotopic distributions, it would be highly unlikely to observe any americium isotope heavier than mass number 244 by beta-particle detection. Cross-section limits for beta-particle detection are roughly 1 microbarn. The situation only becomes worse for observation of actinides isotopes up to mendelevium since the products are increasingly more neutron deficient as can be seen in Figure 37.[95] (This figure is a compilation of actinide yields from various heavy ion-heavy target reactions performed by the Berkeley, Livermore, Argonne and GSI groups. The ^{238}U + ^{238}U results are from the GSI group and the ^{48}Ca + ^{248}Cm results are all from the Hulet group at Livermore.) Beyond mendelevium, any new heavy isotopes would decay by alpha-particle emission or spontaneous fission allowing lower detection limits; however, the peaks of the isotopic distributions would still occur to the neutron deficient side of beta-stability.

From the isotopic distributions of neptunium, plutonium and americium, the estimates given in Table 32 can be made by simple extrapolation of the curves shown in Figures 23 and 24. All count-rates are for the first count taken of that chemical fraction after chemical separation. Beam fluxes and irradiation times used in the estimates are those given in Table 1. Beta-particle count-rates have been corrected for detection efficiencies by use of the curves in Figure 15 (Pu counted on shelf 1; Np counted on shelf 5). Gamma-ray count-rates have not been adjusted for detection efficiency or gamma-ray intensities except as noted. Cross-section values represent upper-limits. It can be seen from these estimates that there is little possibility of observation of new neutron excessive nuclides near the target from a uranium target. Significantly lower detection limits are required for observation of new beta-particle emitting nuclides from these reactions.

As the Z of the products is increased, the products become more neutron deficient. This makes observations of new beta-particle emitting isotopes of elements removed by several Z units from the target even more difficult due to the extremely low production cross-sections. For elements heavier than atomic number 101, new heavy isotopes would most likely decay by alpha-particle emission or spontaneous fission. Detection limits for these types of decay are in the nanobarn range. However, in this mass region cross-sections of new heavy isotopes will probably be lower than the detection limits by several orders of magnitude.

Table 32. Cross-Section and Count-Rate Estimates for Neutron Excessive Nuclides Produced from Uranium Targets. (Predictions based on isotopic distributions.)

Nuclide	Method of Observation	Cross-Section (μb)	Count-Rate (cpm) in 1st Count[a]
Np-241	β^-(γ-135 keV)	50	15 (120)
Np-242	β^-	1	0
Pu-246	β^- (γ-270 keV)	10^{-1}	0.1 (0.5)[b]
Pu-247	β^-	5×10^{-2}	1[c]
Am-246	β^-	10^{-2}	0
Am-247	β^-	$<5\times10^{-3}$	0

(a) No adjustments for detection efficiency (for gamma-rays).

(b) Adjusted for gamma-ray intensity.

(c) Half-life assumed to be 15 min.

One further point about using deep inelastic processes to make new isotopes—heavy ion reactions are extremely non-specific. Virtually every element in the periodic table is produced either by direct reaction with the target or contaminants in the target or by fission of the heavy fragment. This poses a problem in observation of beta-particle emitters because of the chemical separations and decontamination factors required to produce pure samples.

If the deep inelastic process is to be applied to new actinide isotope production, the choice of the target is very important. As can be seen in Figures 23 and 24 the isotopic distributions are very steep near the target. The distributions become broader as the Z increases but cross-sections are dropping very rapidly with Z. Observation of new beta-particle emitters requires greater than microbarn cross-sections. This forces the choice of target to be one within ~3-4 charges of the nuclide that is sought and the target mass number to be within ~6 mass units from the "new isotope." Under these constraints, it would be reasonable to choose ^{244}Pu or ^{248}Cm as targets for use in producing ^{247}Pu. ^{248}Cm could also be used to produce ^{252}Bk. If the "new isotope" is expected to be an alpha-particle emitter, the limits in added charge and mass of detectable nuclides may be extended somewhat because of the greater sensitivity for detection.

To this point, no comment has been made concerning identification of the Z and A of the new activity. The use of chemical separations can lead to the identification of the atomic number of the new activity provided the separation is clean and specific. Perhaps the most conclusive evidence as to the Z and A is the identification of a known daughter activity. This can be almost impossible if the parent is ^{252}Bk, ^{252}Cm or ^{248}Am due to the long half-lives of the daughters. There is some possibility of identifying ^{247}Pu through observation of growth and decay of ^{247}Am. Harvey, <u>et al.</u>,[96] have proposed criteria for discovery of new elements;[96] presumably, similar criteria would apply for identification of new isotopes of existing elements.

More direct methods of synthesizing new isotopes may be more appropriate than deep inelastic reactions. These methods include fast neutron irradiations of heavy targets as was used by Katcoff, <u>et al.</u>,[36] in the production of ^{242}U and ^{242}Np. The (t,p) reaction has been used to produce ^{259}Fm from a ^{257}Fm target,[97] to produce ^{256m}Es from an ^{254}Es target,[98] and to produce ^{256}Cf from a ^{254}Cf target.[99] The (α,n) reaction with an ^{255}Es target has been used to produce the 43 minute isomer of ^{258}Md.[99] Neutron capture by ^{250}Cm has been used to produce ^{252}Cm.[100] If possible, methods such as these should be attempted before resorting to heavy ion reactions on heavy targets.

Comparison of isotopic distributions in Figures 23 and 24 reveals two points. First, the cross-sections of neptunium and plutonium isotopes are somewhat higher from the ^{86}Kr reaction than from the ^{136}Xe reaction, and the americium cross-sections are about the same from the two reactions. As can be seen in Figure 37 this trend is reversed beyond americium. Second, the peak in each distribution seems to occur at roughly the same mass number--238 for neptunium (this excludes ^{239}Np from the distribution), 239.5 for plutonium, and 241.5 for americium. These facts will be discussed further in relation to the thick tantalum target experimental results later in the discussion. No conclusions can be drawn about the widths of the distributions because of the lack of data; however, as a first approximation, the distributions of isotopes of elements near the target are similar.

To conclude this section of the discussion, the implications of the last paragraph to new isotope production should be pointed out. If the target is within ~3 charges from the "new isotope" there is little difference which projectile is used for the reaction. In general, the cross-sections of isotopes near the target are slightly higher with ^{86}Kr than with ^{136}Xe but no advantage is gained in the width of the distributions. However, roughly an order of magnitude is gained in cross-sections if ^{238}U is used as the projectile.[30]

B. Thick Tantalum Targets

The discussion in this section will center on the data presented in Tables 20 and 21 and Figures 25 and 26. Three general trends can be observed. First, the cross-sections from the ^{86}Kr induced reaction drop rapidly with an increase in Z above the target whereas the cross-sections from the ^{136}Xe induced reaction drop more slowly with Z. This is similar to, but somewhat more dramatic than, that observed in reactions with a uranium target. Table 33 lists the

Table 33. Peak Isotopic Distribution Cross-Sections of Products Heavier than the Target.

Z	Cross-Section (mb) $^{86}Kr+^{181}Ta$	$^{136}Xe+^{181}Ta$	$^{86}Kr+^{238}U$ (a)	$^{136}Xe+^{238}U$(b)	$^{238}U+^{238}U$(c)
2	—	—	~1.5×10^{-1}	~1×10^{-1}	--
3	—	—	3.1×10^{-2}	3.0×10^{-2}	--
4	3.0×10^{0}	1.2×10^{0}	3×10^{-3}	3.5×10^{-3}	1.2×10^{-1}
5	--	--	--	—	--
6	1.6×10^{0}	4.4×10^{-1}	2×10^{-5}	4×10^{-5}	4×10^{-4}
7	6.6×10^{-1}	2.6×10^{-1}	~5×10^{-7}	~3×10^{-6}	1.5×10^{-5}
8	1.3×10^{-1}	1.6×10^{-1}	5×10^{-8}	—	2×10^{-6}
9	—	--	--	—	--
10	1.8×10^{-2}	~1.1×10^{-1}	--	—	--

(a) Reference 95 and this work.

(b) Reference 30 and 95 and this work.

(c) Reference 30 and 102.

cross-section at the peak of the isotopic distributions for a given number of charges transferred to the target. These data are shown in graphical form in Figure 38. The references are given in the figure caption. These data are presented to compare peak cross-sections for the same number of charges transferred to the target. The results from the ^{136}Xe + Ta reaction show a nearly linear decrease in cross-section with increased proton transfer to the target. For comparison purposes, the results of thick target reactions of ^{86}Kr, ^{136}Xe, and ^{238}U with uranium are shown on the same graph. The decrease in cross-section with increase in Z is much more rapid from the uranium target experiments and also, as would be expected, the cross-sections are much lower from the uranium reactions. The primary factor in this difference is almost certainly the loss of cross-section due to fission of the uranium-like fragment from the reactions with uranium. Other factors affect cross-sections as well since the choice of projectile affects cross-sections for the same Z from the same target. Comparison of cross-sections for the same charge transfer to a tantalum target shows that the ^{86}Kr reaction yields higher cross-sections than the ^{136}Xe induced reaction near the target but at about 7-8 charge transfers the trend is reversed. Within the uranium target experiments, the ^{86}Kr and ^{136}Xe reactions show similar cross-sections to about a 5-6 charge transfer then ^{86}Kr reaction cross-sections drop significantly below the ^{136}Xe reaction cross-sections. The results from the ^{238}U + ^{238}U reaction are quite different possibly due to the symmetry of the reaction since the mass and the charge do not have to equilibrate in the reaction. In the reactions of ^{86}Kr and ^{136}Xe with heavy targets the trend is for mass to flow from the heavy target to the lighter projectile.

The second trend is that in general the widths of the isotopic distributions appear broader for the ^{136}Xe reactions with tantalum than for the ^{86}Kr reactions. The width of the distribution is governed by the primary fragment distribution width and the range of excitation energies of the primary fragments.[30,101] So, the differences in widths can result not only from differences in the primary fragment distributions but also in differences in excitation energies of the primary fragments. Since almost all of the data in this work fall on one side of the isotopic distributions, nothing quantitative can be obtained from the widths of the distributions.

The third trend is the location of the peaks in the isotopic distributions. Table 34 contains a list of the peak position as a function of ΔZ ($Z_{observed}-Z_{target}$) and ΔA ($A_{observed}-A_{target}$) for this work as well as several other reactions with heavy targets. These data are plotted in Figure 39. The results show a linear increase in mass with an increase in Z transferred to the target. The slope of this line ($\frac{\Delta Z}{\Delta A}$) in all cases is greater than the slope of the line of beta-stability and so heavy products from these reactions will always be more neutron deficient than the target It should be noted that the slopes of all of these lines except that for the ^{48}Ca + ^{248}Cm reaction are very similar (if the Bi point is removed from the

Table 34. Location of the Peak of the Isotopic Distributions Relative to the Target for Heavy Ion - Heavy Element Reactions

	ΔA for					
ΔZ	^{86}Kr+^{181}Ta	^{86}Kr+^{238}U$^{(a)}$	^{136}Xe+^{181}Ta	^{136}Xe+^{238}U$^{(b)}$	^{238}U + ^{238}U$^{(c)}$	^{48}Ca + ^{248}Cm$^{(d)}$
1	—	0	—	0	—	-
2	0	1.5	1	2	2.5	2.0
3	2	3.5	2.5	3.5	4.5	~4
4	5.5	5	5.5	6.0	6	7
5	7.0	—	7.5	—	11.3	—
6	9.0	11	9	11.0	13.4	—
7	11.5	12	11.0	$\leq$14	15.5	—
8	13.7	~14	15.0	—	—	—
9	—	—	—	—	—	—
10	20.2	—	~20	—	—	—

(a) Reference 95 and this work.

(b) References 30 and 95 and this work.

(c) References 30 and 102.

(d) Reference 15.

^{86}Kr + ^{181}Ta graph, the slope is 0.437). The only difference in these lines is the Z at which the net mass transfer is zero. For all of the uranium experiments and for the curium experi- ment, this Z is ~1.1 charges above the target; for the tantalum experiments this Z is ~2.0 charges above the target. This leads one to believe that the primary effect of the projectile on production of nuclides heavier than the target is its influence on cross-section. The final products observed in these reactions appear to be in the same position in Z and A relative to the target for any projectile used. The only difference in positioning seems to be dependent on the target—the change in Z at which the net mass transfer is zero. The Z/A of the isotope at the peak of the isotopic distributions (~0.42) does not correspond to the Z/A of the compound system of the reaction (0.387 for ^{238}U + ^{238}U to 0.408 for ^{86}Kr + ^{181}Ta).

If the above relation is assumed to hold for all heavy ion-heavy target reactions, then it is interesting to apply this to superheavy element production. Using a slope of 0.43 and a ΔZ with no mass transfer of 1.0, the "most probable" mass of elements above the target can be predicted from the equation:

$$Z - Z_{target} = 0.43\ (A - A_{target}) + 1.0 \quad .$$

This equation would yield estimations of the "most probable" mass of element 114 as 288 ($N = 174$) for the reaction of heavy ions with a ^{248}Cm target and 287 ($N = 173$) for the reaction of heavy ions with

^{254}Es. Depending on which theories are used, this leads to isotopes of element 114 whose half-lives would be on the order of milliseconds to minutes.[103,104] Cross-sections for production of superheavy elements cannot be predicted from data presented in this paper; however, an estimate of 0.1 mb for a primary product of $Z = 114$ from ^{238}U + ^{238}U is given by Schädel, et al.[30]

C. Thin Tantalum Targets

The discussion in this section will focus on the excitation functions of the heavy products from the reactions of ^{86}Kr and ^{136}Xe with ^{181}Ta. The results of these experiments are given in Tables 22-28 and are shown graphically in Figures 25-34. The bombardment energy and the thickness of the targets (in MeV) for these reactions are given in Tables 29 and 30.

The isotopic distributions of bismuth isotopes from both heavy ion induced reactions do not show any change in shape with a change in energy of the projectile. If ^{190}Au is ignored, the shapes of the gold isotope distributions do not change with energy either. This result is in agreement with the results obtained for heavy actinide products from the reaction ^{238}U + ^{238}U performed at various incident energies.[102] The results of those experiments showed that the shape and location of the distributions of californium, einsteinium, and fermium isotopes remain the same at incident energies ranging from 6.5 MeV/A to 8.7 MeV/A. ^{190}Au is the exception to this trend. The discrepancy does not seem to arise from problems in detection and identification of this nuclide since in most cases the cross-section is based on the identification of several gamma-ray energies. Possibly, the change in the cross-section may be due to cross-section for mass number 190 being "lost" due to an unknown isomer. This might arise from changes in angular momentum transfer. In either case, the behavior of ^{190}Au is the only indication that the shapes or positions of the isotopic distributions change with projectile energy.

It seems reasonable to conclude from this that within roughly one mass number unit, the position of the isotopic distributions of elements heavier than the target does not change with a change in the heavy ion incident energy. Further, the shape (width) of the distributions does not show a major change with projectile energy. One possible reason for this behavior may be that the net effect of mass and energy transfer at different projectile energies is to give the same final products at all energies. That is to say, if more neutrons (for the same charge transfer) are transferred to the target at the higher projectile energy, then enough extra excitation energy is given to the primary fragment to evaporate the additional neutrons with the net effect of yielding the same final products. Correlation of nucleon transfer and kinetic energy loss has been demonstrated.[26]

The excitation functions for the production of individual isotopes of gold and bismuth are shown in Figures 31-34. Within the errors shown, the excitation functions of all isotopes of the same element are the same. This would be expected if the shape and position of the isotopic distributions remain the same at all energies. However, the unusual behavior of ^{190}Au is again observable showing a completely different behavior from all other gold isotopes from the ^{86}Kr induced reaction. Although the behavior of ^{190}Au in the ^{136}Xe induced reaction is not the same as that for the ^{86}Kr induced reaction, the cross-section for the production of ^{190}Au seems to change more drastically than that for the other gold isotopes. The curves drawn in these figures represent smooth fits to the data and therefore appear different in shape; however, when the errors are considered, the same curve may be drawn for excitation functions for all isotopes of the same element. The shape of the excitation functions for gold and bismuth isotopes from the same heavy ion reaction are very similar.

The excitation functions show a peak at a projectile energy of 1.4–1.5 times the Coulomb barrier (B) in all excitation functions except ^{190}Au from ^{86}Kr + ^{181}Ta. When viewed as a function of the ratio of the incident energy to the Coulomb barrier energy, E/B, the drop in cross-section at higher energy shows little dependence on the projectile. If viewed in terms of the available energy above the Coulomb barrier, ^{86}Kr induced reactions show a more dramatic drop in cross-section with an increase in energy. In either case, the drop in cross-sections exhibited for the production of gold and bismuth isotopes from the same reaction is nearly the same in all cases. The decrease in cross-section of products heavier than the target with an increase in projectile energy has also been observed by Schädel.[102] He has observed a decrease in cross-section of heavy actinide products from the reaction ^{238}U + ^{238}U. The peak in the excitation functions for the production of actinides occurs near 6.7 MeV/A (projectile energy) with a fairly rapid decrease in cross-section above this energy.

The decrease in cross-section at the higher energies observed with the tantalum targets could be due to the fission of the heavy fragment. Russo, et al.,[105,106] have observed secondary fission of heavy products in the reaction $^{136}Xe + {}^{197}Au$. Wozniak, et al.,[107] and Rajagapalan, et al.,[108] have observed this in the reaction $^{86}Kr + {}^{197}Au$. At the high excitation energy and angular momentum available in heavy ion reactions, it is possible to cause a substantial fraction of products heavier than the target in the gold region to undergo fission. Above ~1.4 times the Coulomb barrier, the combination of excitation energy and angular momentum may be enough to cause an overall decrease in cross-section due to fission.

One other point needs to be considered in the reaction of ^{86}Kr with thin tantalum targets. An experiment was performed in which the incident energy of the projectile was very close to the Coulomb barrier in which unusually high cross-sections were obtained for gold isotopes. Because the energy was so close to the Coulomb barrier, the cross-section will be strongly affected by the value of the barrier used to calculate the thickness of the target over which the reactions occurred. The cross-sections obtained by use of the Coulomb barrier as calculated using the equation in the Experimental Methods section appear too high by about one order of magnitude. Values of the Coulomb barrier calculated by other methods[109-111] will only differ by a few percent from that used in this paper. This change in the

Coulomb barrier will not change the cross-sections enough to yield reasonable values. Extrapolations of the excitation functions would indicate measurable cross-sections near the Coulomb barrier but not to the extent indicated by the low energy ^{86}Kr data.

VII. CONCLUSIONS

From the results obtained in attempts to produce new actinide isotopes, it is reasonable to state that except in certain cases the deep inelastic mechanism should be used as a last resort. Other methods can present a much more direct route to new isotopes and yield a more limited number of products. Although cross-sections from the deep inelastic reaction in the best cases may be comparable to cross-sections obtained via other reactions, additional problems of chemical separation and identification arise due to the wide range of nuclides produced. Unless the "new isotope" is near the peak of the isotopic distributions, the cross-section is likely to be lower than the detection limits.

Results from heavy ion reactions with thick tantalum targets have indicated a lack of sensitivity of the heavy reaction products on the heavy ion projectile. Products from all heavy target-heavy projectile combinations investigated show the same positioning in change in Z and change in A above the target. The "most probable" mass of a particular element heavier than the target may be predicted by the equation:

$$Z-Z_{\text{target}} = 0.43\ (A-A_{\text{target}}) + 1.0\quad .$$

From this, the most probable mass number of a superheavy element with Z = 114 can be predicted. The predicted values of the mass number are 288 from a heavy ion reaction with a ^{248}Cm target and 287 from the reaction with an ^{254}Es target. The projectile appears to primarily govern the cross-sections of the heavy nuclide and has a small effect on the widths of the isotopic distributions.

Results from the reactions of heavy ions with thin tantalum targets have indicated that there is little if any change in shape or position of the isotopic distributions with a change in projectile energy. Nuclidic cross-sections rise with energy to a maximum at ~1.4 times the Coulomb barrier then decrease at higher energies. Presumably this decrease in cross-section is due to the fission of the heavy fragment, caused by additional excitation energy and angular momentum transferred to the target at the higher projectile energies. Based on these observations and similar observations for heavy actinide products from the reaction $^{238}U + ^{238}U$, one must choose carefully the projectile energy for production of nuclides heavier than the target since the higher cross-sections for these products occur at lower energies.

REFERENCES

1. Nuclear Spectroscopy and Reactions, Part B, J. Cerny, ed., Academic Press, New York (1974).
2. T. D. Thomas, Ann. Rev. Nucl. Sci. 18, 343 (1968).
3. J. R. Huizenga, Acct. Chem. Res. 9, 325 (1976).
4. F. Hanappe, M. Lefort, C. Ngô, J. Péter, B. Tamain, Phys. Rev. Lett. 32, 738 (1974).
5. K. L. Wolf, J. P. Unik, J. R. Huizenga, J. R. Birkelund, H. Freiesleben, V. E. Viola, Phys. Rev. Lett. 33, 1105 (1974).
6. J. V. Kratz, A. E. Norris. G. T. Seaborg, Phys. Rev. Lett. 33, 502 (1974).
7. J. V. Kratz, J. O. Liljenzin, A. E. Norris, G. T. Seaborg, Phys. Rev. C 13, 2347 (1976).
8. S. G. Thompson, L. G. Moretto, R. G. Jared, R. P. Babinet, J. G. Galin, M. M. Fowler, J. B. Hunter, Phys. Scr. A10, 36 (1974).
9. A. G. Artyukh, G. V. Gridnev, V. L. Mikheev, V. V. Volkov, J. Wilczynski, Nucl. Phys. A215, 91 (1973).
10. J. Péter, C. Ngô, B. Tamain, J. de Phys. Lett. 36, L23 (1975).
11. D. C. Hoffman, private communication.
12. K. A. Geoffroy, D. G. Sarantites, M. L. Halbert, D. C. Hensley, R. A. Dayras, J. H. Barker, Phys. Rev. Lett. 43, 1302 (1979).
13. R. J. Otto, M. M. Fowler, D. Lee. G. T. Seaborg, Phys. Rev. Lett. 36, 135 (1976).
14. R. Vandenbosch, M. P. Webb, T. D. Thomas, M. S. Zisman, Nucl. Phys. A263, 1 (1976).

15. E. K. Hulet, R. W. Lougheed, J. F. Wild, J. H. Landrum, P. C. Stevenson, A. Ghiorso, J. M. Nitschke, R. J. Otto, D. J. Morrissey, P. A. Baisden, B. F. Gavin, D. Lee, R. J. Silva, M. M. Fowler, G. T. Seaborg, Phys. Rev. Lett. 39, 385 (1977).

16. J. D. Illige, E. K. Hulet, J. M. Nitschke, R. J. Dougan, R. W. Lougheed, A. Ghiorso, J. H. Landrum, Phys. Lett. 78B, 209 (1978).

17. R. J. Otto, D. J. Morrissey, D. Lee, A. Ghiorso, J. M. Nitschke, G. T. Seaborg, M. M. Fowler, R. J. Silva, J. Inorg. Nucl. Chem. 40, 589 (1978).

18. V. V. Volkov, Phys. Rep. 44, 93 (1978).

19. R. J. Otto, D. J. Morrissey, G. T. Seaborg, W. D. Loveland, International Symposium on Superheavy Elements, ed. M.A.K. Lohdi, (Pergamon, New York, 1978).

20. G. T. Seaborg, W. Loveland, D. J. Morrissey, Science 203, 711 (1979).

21. G. Hermann, Nature 280, 543 (1979).

22. W. U. Schröder, J. R. Huizenga, Ann. Rev. Nucl. Sci. 27, 465 (1977).

23. M. Lefort, C. Ngô, Ann. Phys. 3, 5 (1978).

24. L. G. Moretto, Lectures given at the" Post-Conference School on Selected Topics in heavy Ion Physics" International Conference on Dynamical Properties of Heavy Ion Reactions, Univ. of the Witwatersrand, Johannesburg, South Africa, also Lawrence Berkeley Laboratory Report LBL-8936, (1979).

25. J. R. Huizenga, Comm. Nucl. Part. Phys. 7, 17 (1976).

26. J. R. Huizenga, J. R. Birkelund, W. U. Schröder, K. L. Wolf, V. E. Viola, Phys. Rev. Lett. 37, 885 (1976).

27. P. Glässel, R. C. Jared, L. G. Moretto, Nucl. Inst. Meth. 142, 569 (1977).

28. K. L. Wolf, J. P. Unik, E. P. Horwitz, C. A. A. Bloomquist, W. Delphin, Bull. Am. Phys. Soc. 22, 67 (1977).

29. R. Lucas, J. Poitou, J. V. Kratz, G. Wirth, Z. Phys. A 290, 327 (1979).

30. M. Schädel, J. V. Kratz, H. Ahrens, W. Brüchle, G. Franz, H. Gäggeler, I. Warnecke, G. Wirth, G. Hermann, N. Trautmann, M. Weis, Phys. Rev. Lett. 41, 469 (1978).

31. P. A. Baisden, K. E. Thomas, G. T. Seaborg, Lawrence Berkeley Laboratory Report, LBL-6575, pp. 28-29 and 37-38 (1977).

32. P. A. Baisden, G. T. Seaborg, Lawrence Berkeley Laboratory Report LBL-8151, pp. 35-37 (1978).

33. J. V. Kratz, W. Brüchle, G. Franz, M. Schädel, I. Warnecke, G. Wirth, M. Weis, to be published, Nucl. Phys. A.

34. Yu. Ts. Oganesyan, Yu. E. Penionzhkevich, Nguyen Toc Anh, D. M. Nadkarnee, K. A. Gavrilou, Kim De En, M. Yussonua, Yad. Fiz., 18, 734 (1973), also Sov. J. Nucl. Phys. 18, 377 (1974).

35. N. N. Kolesnikou, A. G. Demin, JINR Report P6-9421, Dubna (1975).

36. S. Katcoff, E-M. Franz, P. E. Haustein, R. L. Klobuchar, H-C. Hseu, Bull. Am. Phys. Soc. 24, 614 (1978).

37. N. E. Holden, F. W. Walker, "Chart of the Nuclides," eleventh ed., General Electric Co. (Schenectady 1972).

38. W. Seelmann-Eggebert, G. Pfennig, H. Münzel, Karsruher Nuklidkarte, fourth ed., Kernforschungszentrum Karlsruhe (1974).

39. R. J. Otto, G. T. Seaborg, M. M. Fowler, Phys. Rev. C. 17, 1071 (1978).

40. R. M. Diamond, F. S. Stephens, R. W. Lougheed, E. K. Hulet, Phys. Lett. 68B, 122 (1977).

41. D. Habs, V. Metag, J. Schukraft, H. J. Specht, C. O. Wene, K. D. Hildenbrand, Z. Physik A 283, 261 (1977).

42. P. Colombani, P. A. Butler, I. Y. Lee, D. Cline, R. M. Diamond, F. S. Stephens, D. Ward, Phys. Lett 65B, 39 (1976).

43. R. A. Esterlund, D. Molzahn, R. Brandt, P. Patzelt, P. Vater, A. H. Boos, M. R. Chandratillake, I. S. Grant, J. D. Hemmeingway, G.W.A. Newton, Phys. Rev. C 15, 319 (1977).

44. H. Bruchertseifer, K. A. Gavrilou, Yu. E. Penionzhevich, T. Reetz, Choi Val Sek, Yad. Fiz. 26, 26 (1977), also Sov. J. Nucl. Phys. 26, 1 (1977).

45. J. V. Kratz, J. O. Liljenzin, A. E. Norris, I. Binder, G. T. Seaborg, Proceedings of the International Conference on Reactions Between Complex Nuclei, Nashville, 1974, ed., R. L. Robinson, F. K. McGowan, J. B. Ball, J. H. Hamilton (North-Holland, Amsterdam/American Elsevier, New York, 1974).

46. R. J. Otto, A. Ghiorso, D. Lee, R. E. Leber, S. Yashita, G. T. Seaborg, Radiochim. Acta 24, 3 (1977).

47. H. Gäggeler, W. Brüchle, H. Ahrens, H. Folger, G. Franz, J. V. Kratz, M. Schadel, I. Warneke, G. Wirth, N. Trantmann, G. Hermann, N. Kaffrell, P. Peuser, G. Trittel, M. Zendel, Z. Phys. A 286, 419 (1978).

48. H. Jungclas, D. Heides, R. Brandt, P. Lemmertz, E. Georg, H. Wollnik, Phys. Lett. 79B, 58 (1978).

49. G. Hermann, *International Symposium on Superheavy Elements*, ed. M.A.K. Lodhi, (Pergamon, New York, 1978)

50. J. Péter, C. Ngô, B. Tamain, Nucl. Phys. A250, 351 (1975).

51. K. D. Hildenbrand, H. Freieslehen, F. Puhlhofer, W.F.W. Schneider, R. Bock, D. v. Harrach, H. J. Spect, Phys. Rev. Lett 39, 1065 (1977).

52. R. Vandenbosch, M. P. Webb, T. D. Thomas, M. S. Zisman, Nucl. Phys. A269, 210 (1976).

53. B. Cauvin, R. P. Schmitt, G. J. Wozniak, P. Glassell, P. Russo, R. G. Jared, J. B. Mouton, L. G. Moretto, Nucl. Phys. A294, 225 (1978).

54. H. A. Grunder and F. B. Selph, Proceedings of the 1976 Proton Linear Accelerator Conference, Chalk River, 1976, and Lawrence Berkeley Laboratory Report LBL-5390, (1976).

55. Conceptual Design Report: "High Intensity Uranium Beams," Lawrence Berkeley Laboratory, pub. 96 (1976).

56. SuperHilac User's Manual, Lawrence Berkeley Laboratory Report, Pub. 102 (1979).

57. D. J. Morrissey, University of California, Berkeley, Ph.D. Thesis, Lawrence Berkeley Laboratory Report LBL-7713, (1978).

58. I. Binder, University of California, Berkeley, Ph.D. Thesis, Lawrence Berkeley Laboratory Report LBL-6526, (1977).

59. L. C. Northcliffe and R. F. Schilling, Nucl. Data Tables A7, 223 (1970).

60A. H. J. Krappe and J. R. Nix, Proc. 3rd Symp. on Physics and Chemistry of Fission, Rochester Vol. 1, (Vienna: IAEA) pp. 159-76.

60B. M. Lefort, Rep. Prog. Phys. 39, 129 (1976).

61. Uranium Target Dissolution Procedure. P. A. Baisden, B. Nishida, unpublished.

62. J. E. Grindler, The Radiochemistry of Uranium. Subcommittee on Radiochemistry, Nat'l Academy Sci. - Nat'l Research Council, NAS-NS-3050 (1962).

63. E. K. Hyde, The Radiochemistry of Thorium, Subcommittee on Radiochemistry, Nat'l Acad. Sci. - Nat'l Research Council, NAS-NS-3004 (1960).

64. R. A. Penneman and T. K. Keenan, The Radiochemistry of Americium and Curium, Subcommittee on Radiochemistry, Nat'l Acad. Sci. - Nat'l Research Council, NAS-NS-3006 (1960).

65. G. H. Higgins, The Radiochemistry of the Transcurium Elements, Subcommittee on Radiochemistry, Nat'l Acad. Sci. - Nat'l Research Council, NAS-NS-3031 (1960).

66. P. C. Stevenson and W. E. Nervik, *The Radiochemistry of the Rare Earths, Scandium, Yttrium, and Actinium*, Subcommittee on Radiochemistry, Nat'l Acad. Sci. - Nat'l Research Council, NAS-NS-3020 (1961).

67. G. A. Burney and R. M. Harbour, *Radiochemistry of Neptunium*, Subcommittee on Radiochemistry, Nat'l Acad. Sci. - Nat'l Research Council, NAS-NS-3060 (1974).

68. G. H. Coleman, *The Radiochemistry of Plutonium*, Subcommittee on Radiochemistry, Nat'l Acad. Sci. - Nat'l Research Council, NAS-NS-3058 (1965).

69. O. Samuelson, *Ion-Exchange Separations in Analytical Chemistry*, John Wiley and Sons, Inc., New York (1963).

70. R. M. Diamond, K. Street, Jr., and G. T. Seaborg, J. Am. Chem. Soc. **76** 1461 (1954).

71. F. L. Moore, Anal. Chem. **40**, 2130 (1968).

72. J. R. Stokely, Jr., and F. L. Moore, Anal. Chem. **39**, 994 (1967).

73. J. Kleinberg and H. L. Smith (ed.), Collected Radiochemical Procedures (Radiochemistry Group CNC-11), Los Alamos Scientific Laboratory Report, LA-1721, 4th Ed. (1975).

74. G. H. Morrison, and H. Freiser, *Solvent Extraction in Analytical Chemistry*, John Wiley and Sons, Inc., New York (1957).

75. F. E. Beamish, Talanta **5**, 1-35 (1960).

76. E. P. Steinberg, *The Radiochemistry of Niobium and Tantalum*, Subcommittee on Radiochemistry, Nat'l Acad. Sci. - Nat'l Research Council, NAS-NS-3039 (1961).

77. G. W. Leddicotte, *The Radiochemistry of Iridium*, Subcommittee on Radiochemistry, Nat'l Acad. Sci. - Nat'l Research Council, NAS-NS-3045 (1961).

78. G. W. Leddicotte, *The Radiochemistry of Platinum*, Subcommittee on Radiochemistry, Nat'l Acad. Sci. - Nat'l Research Council, NAS-NS-3044 (1961).

79. J. F. Emery and G. W. Leddicotte, *The Radiochemistry of Gold,* Subcommittee on Radiochemistry, Nat'l Acad. Sci. - Nat'l Research Council, NAS-NS-3036 (1961).

80. J. Roesmer and P. Kruger, *The Radiochemistry of Mercury*, Subcommittee on Radiochemistry, Nat'l Acad. Sci. - Nat'l Research Council, NAS-NS-3026 (1960).

81. W. M. Gibson, *The Radiochemistry of Lead*, Subcommittee on Radiochemistry, Nat'l Acad. Sci. - Nat'l Research Council, NAS-NS-3040 (1961).

82. K. S. Bhatki, *Radiochemistry of Bismuth*, Subcommittee on Radiochemistry, Nat'l Acad. Sci. - Nat'l Research Council, NAS-NS-3061 (1977).

83. A. K. De, *Separation of Heavy Metals*, Pergamon Press, Oxford (1961).

84. M. V. Kantelo, McGill University (Canada), Ph.D. Thesis (1975).

85. J. T. Routti and S. G. Prussin, Nucl. Instr. Meth. 72, 125 (1969).

86. J. T. Routti, Lawrence Berkeley Laboratory Report, UCRL-19452 (1969), unpublished.

87. G. Friedlander, J. Kennedy, J. M. Miller, Nuclear and Radiochemistry, 2nd ed., John Wiley and Sons, Inc., New York, p. 69-76, (1964).

88. D. J. Morrissey, D. Lee, R. J. Otto, and G. T. Seaborg, Nucl. Instr. Meth. 158, 499 (1979).

89. I. Binder, R. Kraus, R. Klein, D. Lee, and M. M. Fowler, Lawrence Berkeley Laboratory Report LBL-6515 (1977), unpublished.

90. W. W. Bowman and K. W. MacMurdc, Atomic and Nuclear Data Tables 13, 89 (1974).

91. C. M. Lederer and V. S. Shirley, Table of the Isotopes, 7th ed., John Wiley and Sons, Inc., New York (1978).

92. U. Reus, W. Westmeir, I. Warnicke, Gesellschaft fur Schwerionenforeschung Report, GSI 79-2 (1979).

93. G. Friedlander, J. Kennedy, J. M. Miller, Nuclear and Radiochemistry, 2nd ed., John Wiley and Sons, Inc., New York, pp. 79-80, (1964).

94. J. V. Kratz, private communication with G. T. Seaborg.

95. P. A. Baisden, private communication.

96. B. G. Harvey, G. Hermann, R. W. Hoff, D. C. Hoffman, E. K. Hyde, J. J. Katz, O. L. Keller, Jr., M. Lefort, G. T. Seaborg, Science 193, 1271 (1976).

97. D. C. Hoffman, J. Weber, J. B. Wilhelmy, E. K. Hulet, R. W. Lougheed, J. H. Landrum, J. F. Wild, Paper presented at the Fourth International Transplutonium Element Symposium, Baden-Baden, Germany (1975), also Lawrence Livermore Laboratory Report UCRL-77103 (1975).

98. R. W. Lougheed, J. H. Landrum, D. C. Hoffman, W. R. Daniels, J. B. Wilhelmy, M. E. Bunker, J. W. Stainer, S. V. Jackson, Paper presented at the Third International Conference on Nuclides Far from Stability, Cargese, Corsica (France) (1976), also Los Alamos Scientific Laboratory Report LA-UR 76-1051 (1976).

99. J. B. Wilhelmy, J. Weber, W. R. Daniels, E. K. Hulet, J. H. Landrum, R. W. Lougheed, J. F. Wild, paper presented at the Conference on Interactions of Heavy Ions with Nuclei and Synthesis of New Elements, Dubna, USSR (1977), also Los Alamos Scientific Laboratory Report LA-UR-77-2901 (1977).

100. R. W. Lougheed, J. F. Wild, E. K. Hulet, R. W. Hoff, J. H. Landrum, Lawrence Livermore Laboratory Report UCRL-79432 (1977).

101. J. Poitou, R. Lucas, J. V. Kratz, W. Brüchle, H. Gäggeler, M. Schädel, G. Wirth, to be published, Phys. Lett. B.

102. M. Schädel, Ph.D. Thesis, Gesellschaft fur Schwerionenforschung Report 79-8 (1979).

103. E. O. Fisset, J. R. Nix, Nucl. Phys. A193, 647 (172).

104. A. Socicewski, Proc. Int. Symp. on SuperHeavy Elements (ed. M.A.K. Lohdi), 294 (Pergmon, New York, 1978).

105. P. Russo, B. Cauvin, P. Glässel, R. C. Jared, R. P. Schmidt, G. J. Wozniak, L. G. Moretto, Lawrence Berkeley Laboratory Report LBL 5050 (1976).

106. P. Russo, R. P. Schmitt, G. J. Wozniak, B. Cauin, P. Glässel, R. C. Jared, L. G. Moretto, Phys. Lett. 67B, 155 (1977).

107. G. J. Wozniak, R. P. Schmitt, P. Glässel, R. C. Jared, G. Bizard, L. G. Moretto, Phys. Rev. Lett 40, 1436 (1978).

108. M. Rajagopalan, L. Kowlski, D. Logan, M. Kaplan, J. M. Alexander, M. S. Zisman, J. M. Miller, Phys. Rev. C 19, 54 (1979).

109. W. U. Schroder, J. R. Birkelund, J. R. Huizenga, K. L. Wolf, J. P. Unik, V. E. Viola, Jr., Phys. Rev. Lett. 36, 514 (1976).

110. J. Blocki, J. Randrup, W. J. Swiatecki, C. F. Tsang, Ann. Phys. 105, 427 (1977).

111. J. V. Kratz, H. Ahrens, W. Bogl, W. Brüchle, G. Franz, M. Schädel, I. Warnecke, G. Wirth, G. Klein, M. Weis, Phys. Rev. Lett. 39, 984 (1977).

FIGURE CAPTIONS

Fig. 15. Detection efficiency calibration curve for β^- detectors.

Fig. 16. Detection efficiency calibration curves for several counting arrangements of Ge(Li)3.

Fig. 17. Detection efficiency calibration curves for several counting arrangements of Ge(Li)4.

Fig. 18. β^- decay curve for neptunium fraction from experiment KU4.

Fig. 19. β^- decay curve for plutonium fraction from experiment KU4.

Fig. 20. Flow scheme for gamma-ray spectra data analysis.

Fig. 21. Gamma-ray spectrum of thallium fraction from experiment KT7.

Fig. 22. TAU2 display from analysis of the thallium fraction from experiment KT2.

Fig. 23. Isotopic distributions for Np, Pu, and Am from the reaction of ^{86}Kr ions with a thick uranium target. Incident energy is 731 MeV (8.5 MeV/A). Dashed curves are intended to aid the eye and are only approximations. The Np distribution is a result of quasi-elastic transfer and deep/inelastic transfer.

Fig. 24. Isotopic distributions for Np, Pu, and Am from the reaction of ^{136}Xe ions with a thick uranium target. Incident energy is 1156 MeV (8.5 MeV/A).

Fig. 25. Isotopic distributions for products heavier than tantalum from the reaction of ^{86}Kr ions with a thick tantalum target. The incident energy is 731 MeV (8.5 MeV/A). Solid points represent measured cross-sections. Open points represent cross-sections corrected for feeding from the parent where the two cross-sections differ. The curves are "eyeball" fits to the corrected cross-sections.

Fig. 26. Isotopic distributions for products heavier than tantalum from the reaction of 1156 MeV ^{136}Xe ions with a thick tantalum target. A description of this type of graph is given for Figure 25.

Fig. 27. Isotopic distributions for gold isotopes from the reactions of 731 MeV, 620 MeV, and 506 MeV ^{86}Kr ions with thin tantalum targets. Each curve represents the isotopic distribution for the indicated energy.

Fig. 28. Isotopic distributions for bismuth isotopes from the reactions of 731 MeV, 620 MeV, and 506 MeV ^{86}Kr ions with thin tantalum targets.

Fig. 29. Isotopic distributions for gold isotopes from the reactions of 1156 MeV, 980 MeV, and 801 MeV ^{136}Xe ions with thin tantalum targets.

Fig. 30. Isotopic distributions for bismuth isotopes from the reactions of 1156 MeV and 980 MeV ^{136}Xe ions with thin tantalum targets. Bismuth isotopes were not observed at 801 MeV.

Fig. 31. Excitation functions for gold isotopes from the reactions of 731 MeV, 620 MeV and 506 MeV ^{86}Kr ions with thin tantalum targets. Each curve is the excitation function of a different isotope. The target thickness is illustrated by the horizontal lines near the bottom of the figure (labeled Target Thickness). Two horizontal scales are used for energy. The lower scale is the excess energy above the Coulomb barrier (in

the center-of-mass system). The upper scale is the ratio of the average energy in the target and the Coulomb barrier. Note the difference in the curve for ^{190}Au (dashed curve) and the similarity of the other curves.

Fig. 32. Excitation functions for bismuth isotopes from the reactions of 731 MeV, 620 MeV and 506 MeV ^{86}Kr ions with thin tantalum targets. A description of the graph is given for Figure 31. Note similarity of curves.

Fig. 33. Excitation functions for gold isotopes from the reaction of 1156 MeV, 980 MeV, and 801 MeV ^{136}Xe ions with thin tantalum targets. The graph is described in Fig. 31.

Fig. 34. Excitation functions for bismuth isotopes from the reactions of 1156 MeV and 980 MeV ^{136}Xe ions with thin tantalum targets. No bismuth isotopes were observed at 801 MeV. The graph is described in Fig. 31.

Fig. 35. Relative cross-sections for rhenium and osmium isotopes from the reaction of 731 MeV ^{86}Kr with tantalum. The rhenium isotopes were observed in the reaction with a thin target. The osmium isotopes were observed in the reaction with a thick target.

Fig. 36. Relative cross-sections for rhenium and osmium isotopes from the reactions of 1156 MeV ^{136}Xe ions with tantalum. The rhenium isotopes were observed in a thin target reaction and the osmium isotopes were observed in a thick target reaction.

Fig. 37. Summary of heavy target experiments performed by the Berkeley, Livermore, Argonne and GSI groups. From Reference 95.

Fig. 38 Cross-sections of the peak of the isotopic distributions plotted against the number of charges transferred to the target for several heavy ion-heavy target reactions. References are given in the figure caption for Figure 39.

Fig. 39. Graph of the location of the peaks of the isotopic distributions as a function of the change in Z and A above the target. References are as follows:

^{48}Ca + ^{248}Cm	Ref. 15
^{238}U + ^{238}U	Ref. 30, 102
^{86}Kr + ^{238}U	Ref. 95 (Fig. 37) and this work.
^{136}Xe + ^{238}U	Ref. 30, 95 (Fig. 37) and this work.
^{86}Kr + ^{181}Ta	This work.
^{136}Xe + ^{181}Ta	This work.

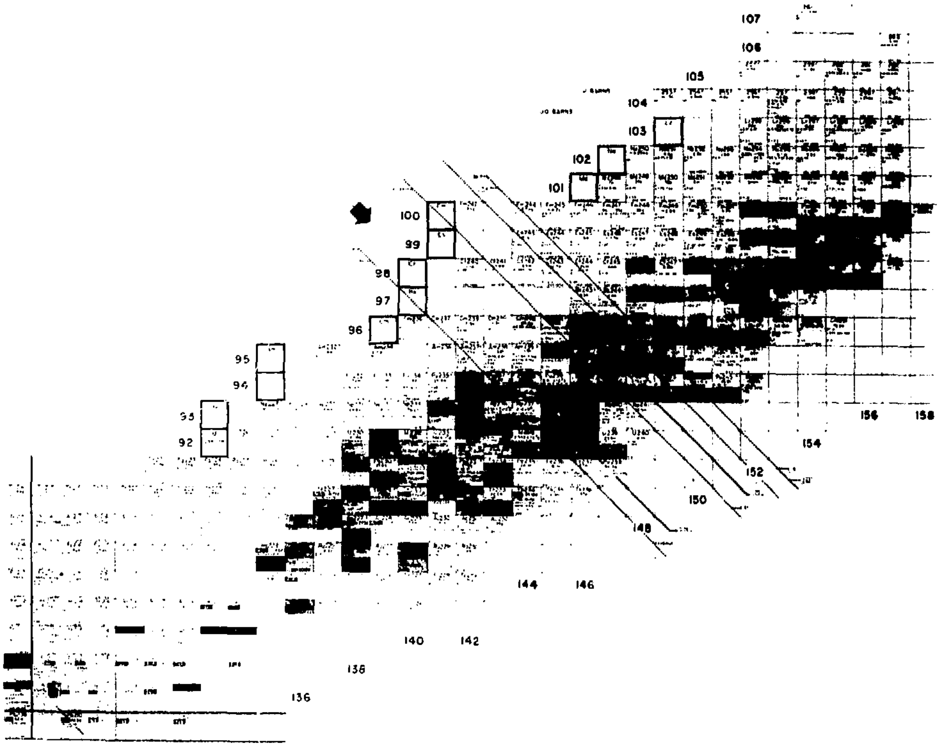

Fig. 1

CBB 783-3608

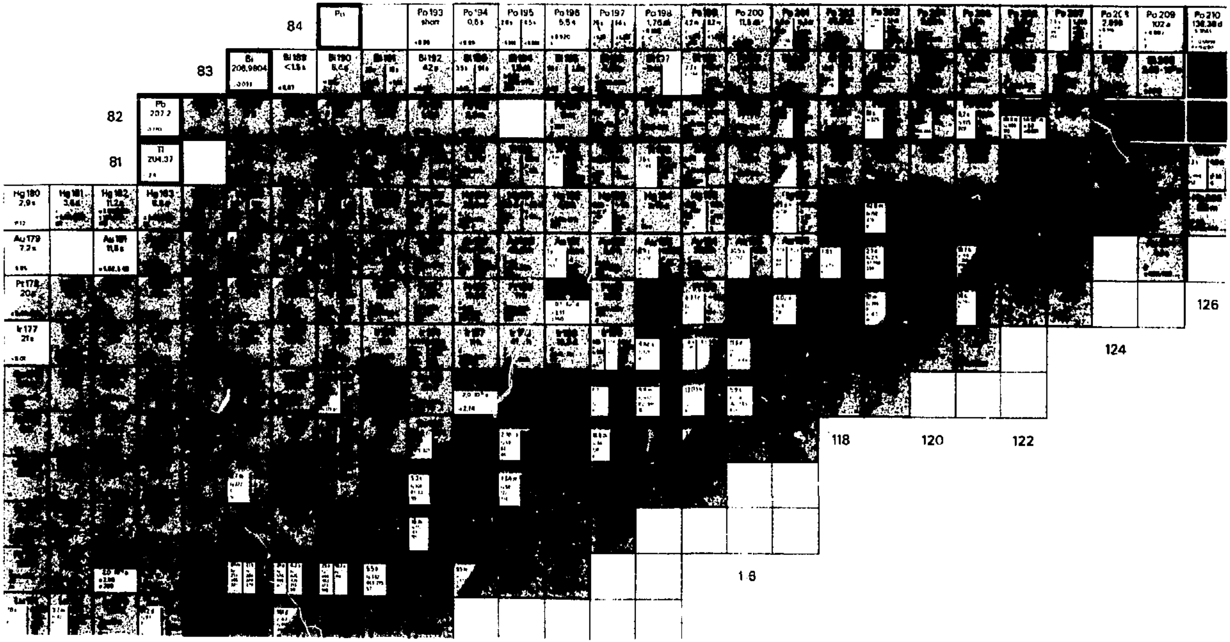

Fig. 2

CBB 790-13497

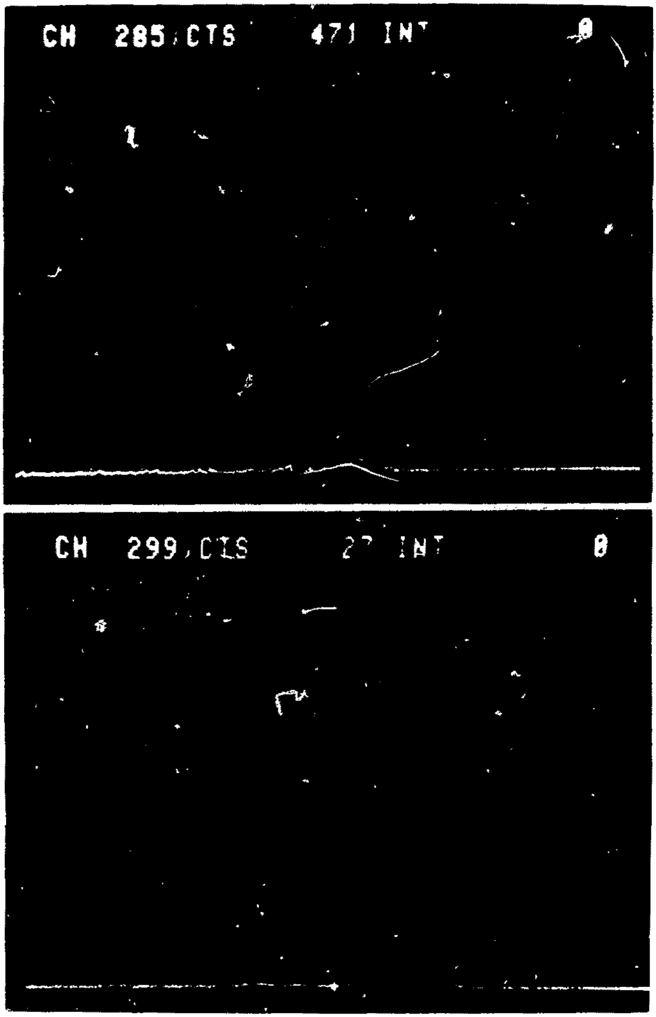

XBB 790-14096

Fig. 3

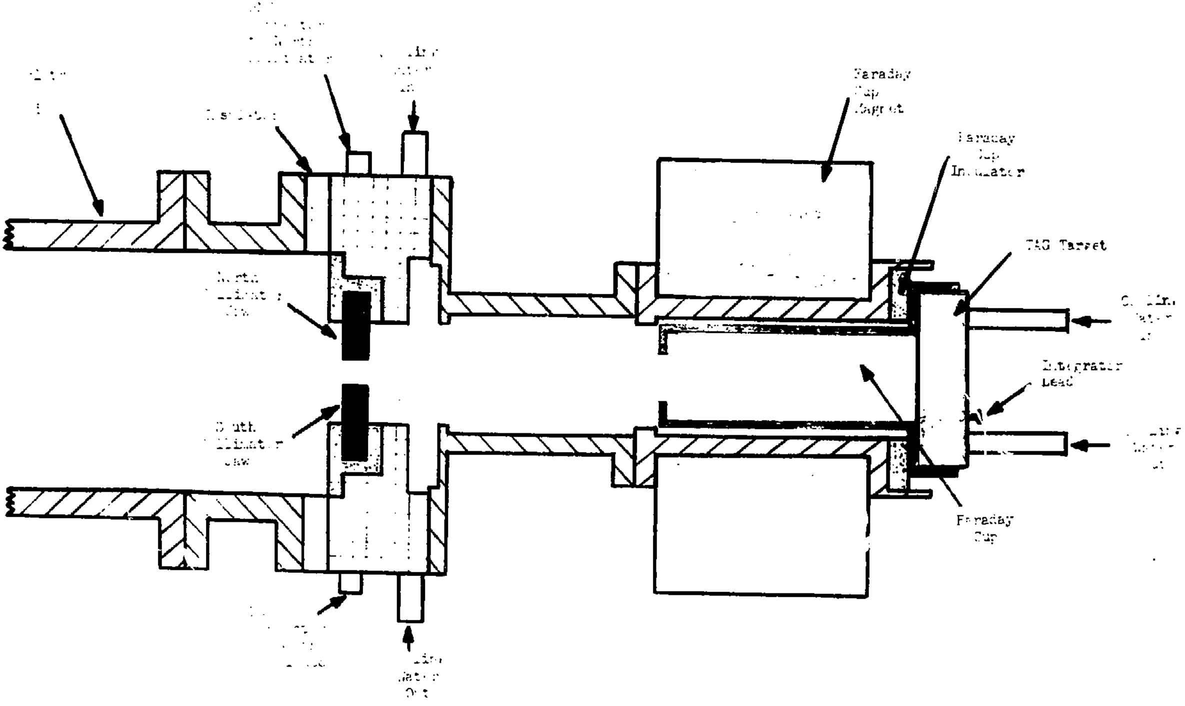

Fig. 4

XBB790 14009

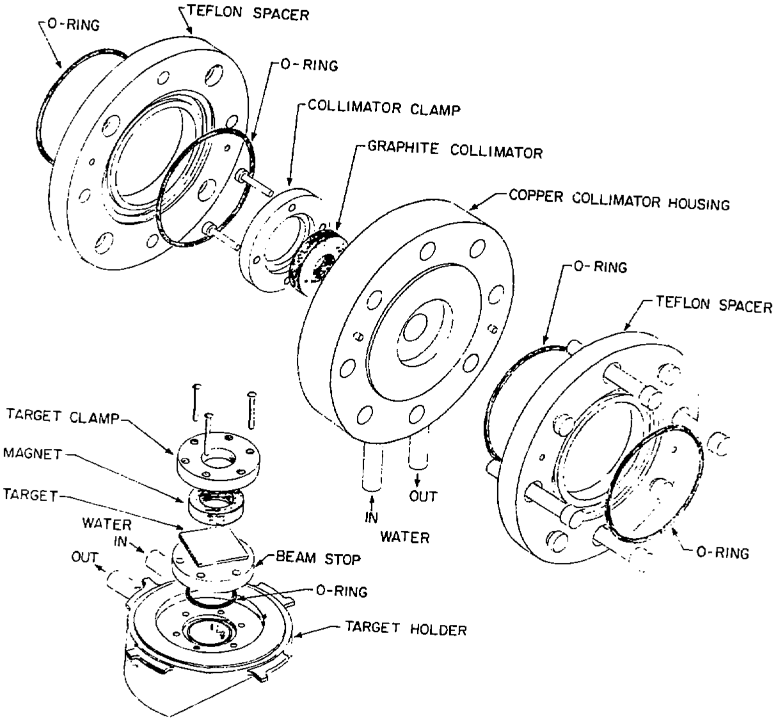

XBL 7910-4518

Fig. 5

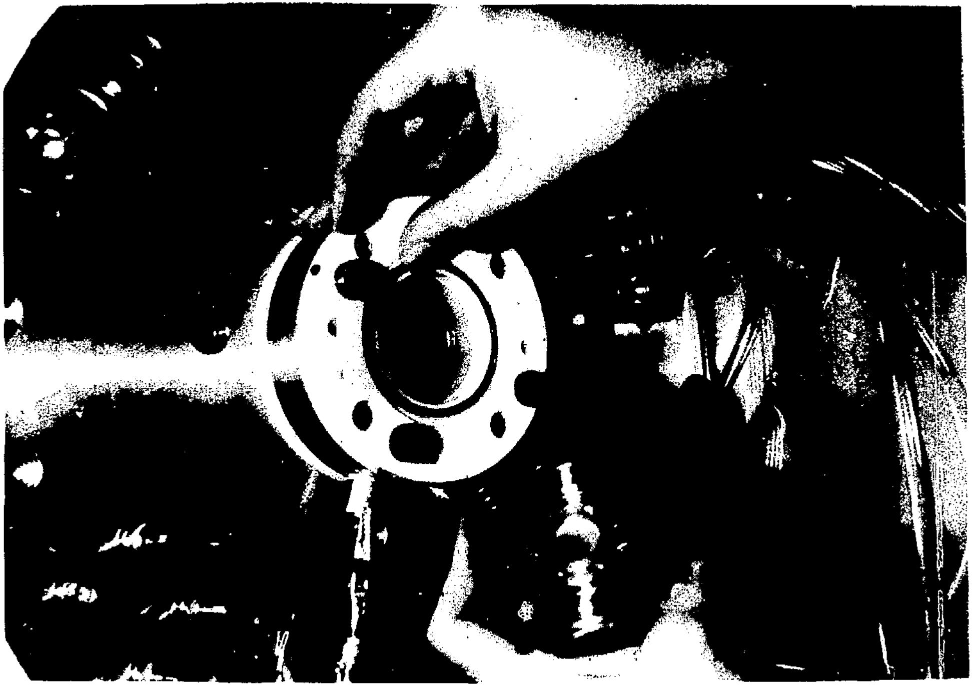

Fig. 6

CBB 793-2991

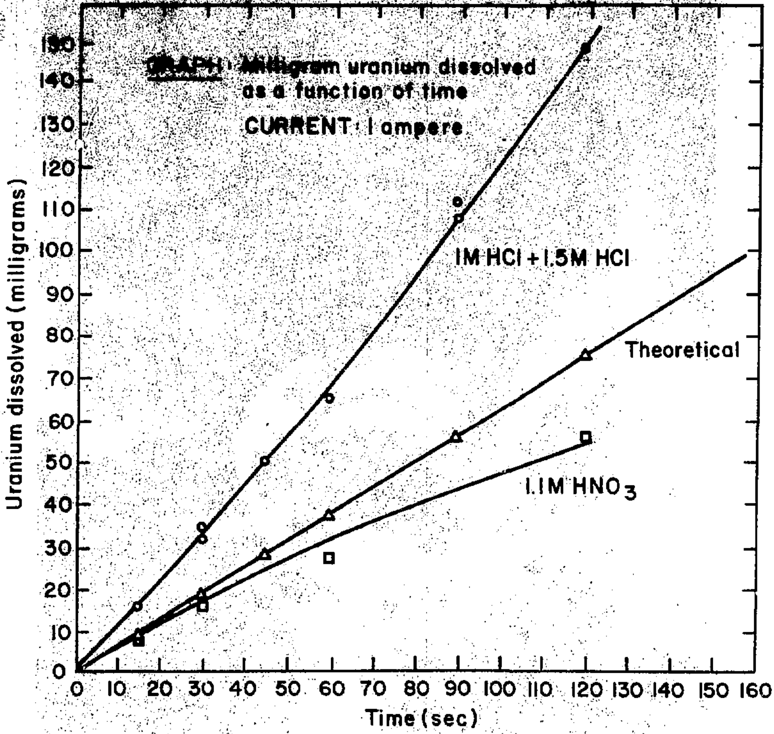

XBL 7910-4451

Fig. 7

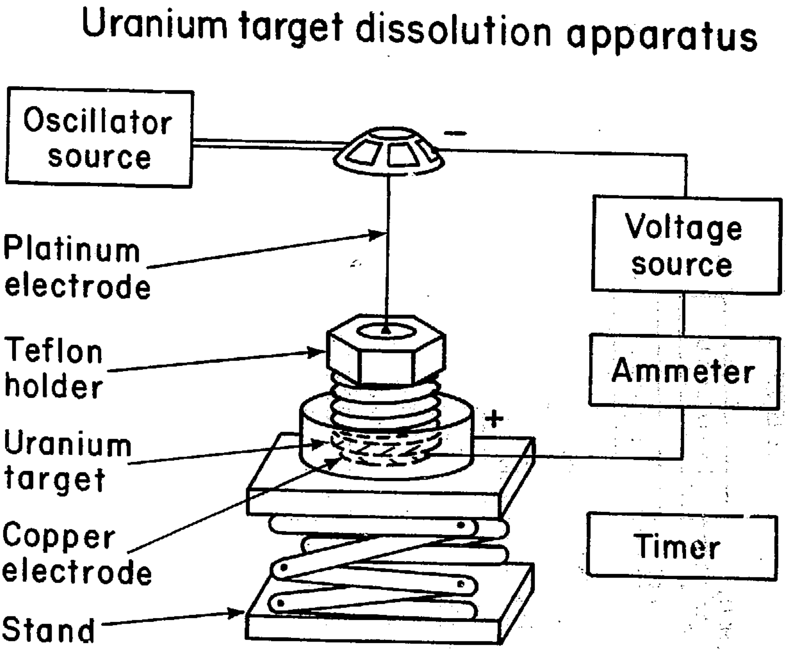

XBL 7910-4447

Fig. 8

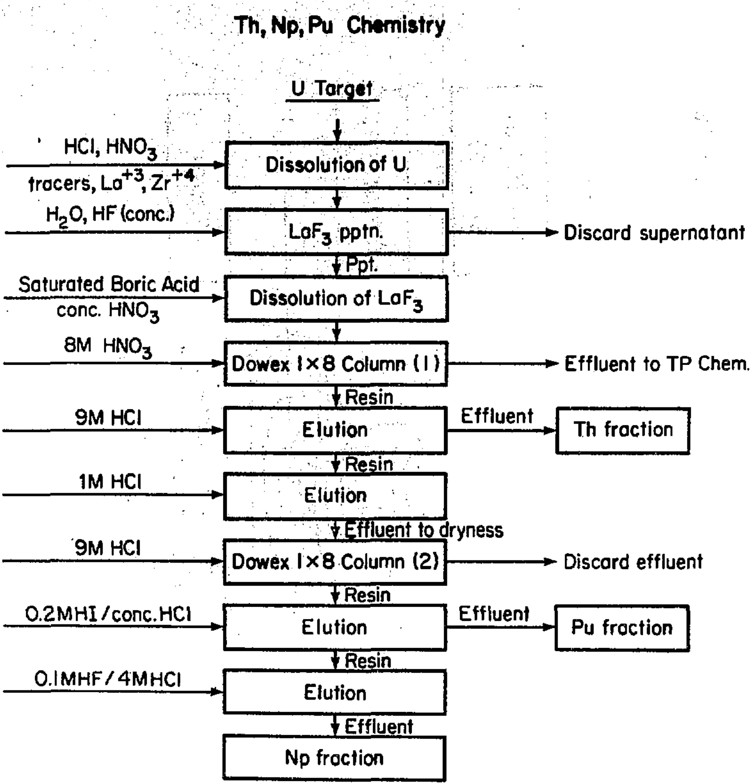

XBL 793 - 1014

Fig. 9

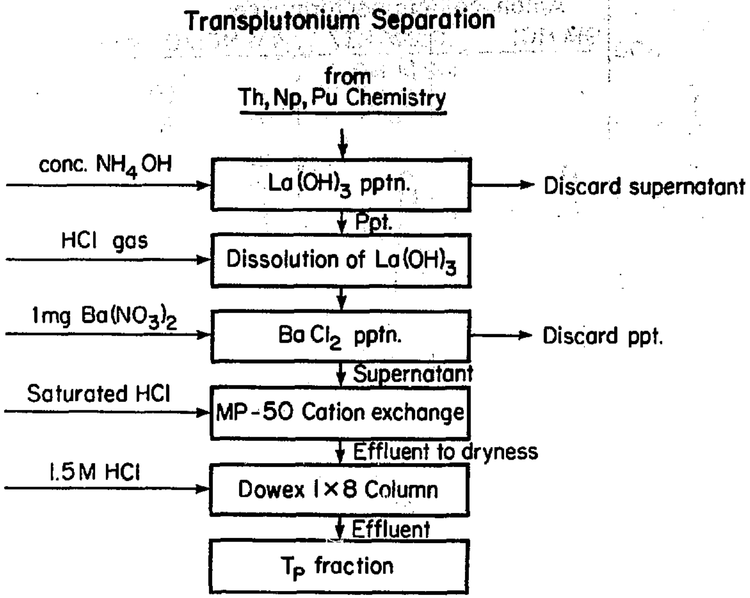

XBL 793-1013

Fig. 10

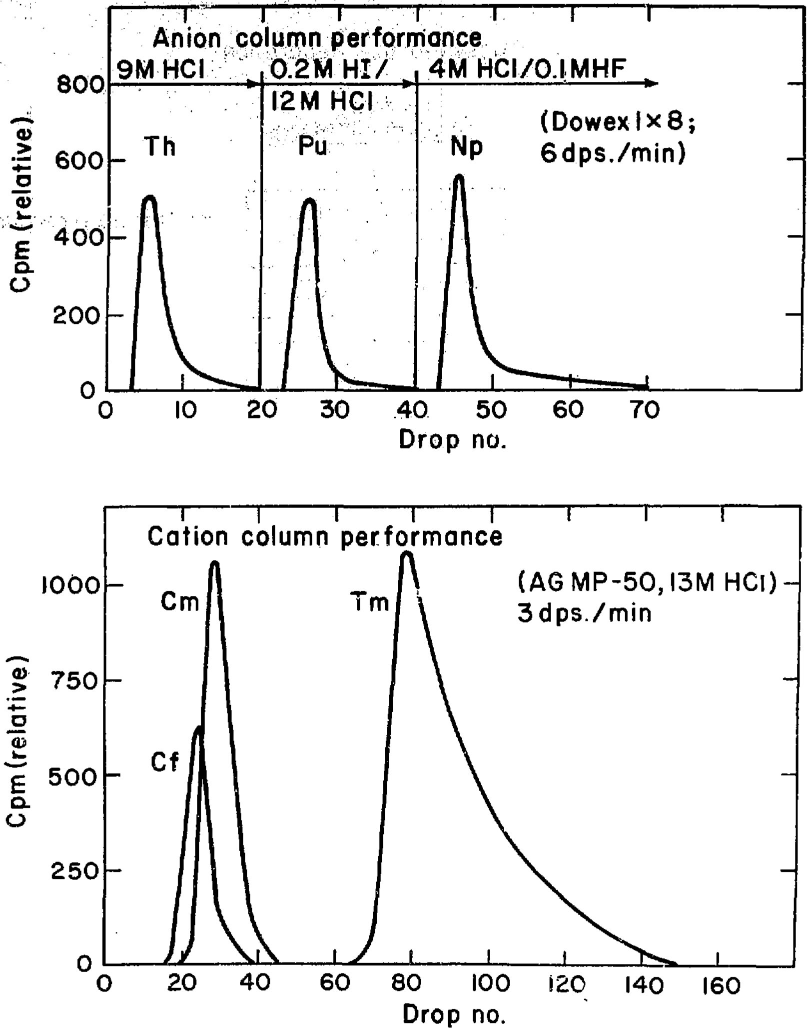

XBL 7910-4450

Fig. 11

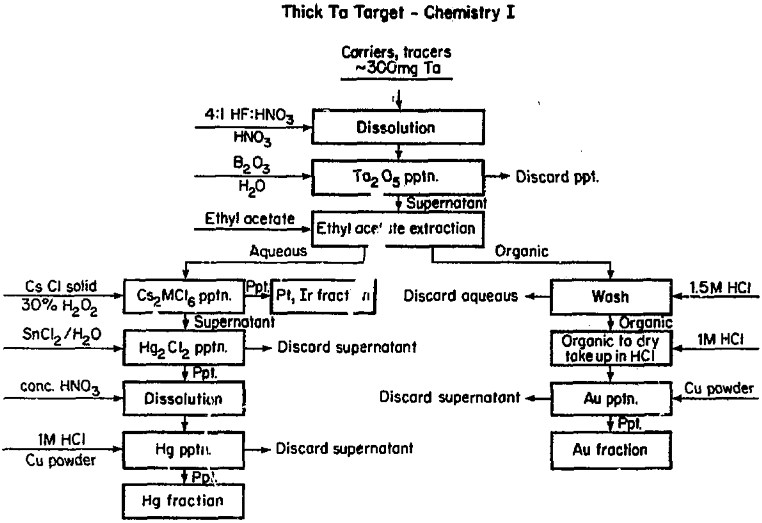
Thick Ta Target - Chemistry I

XBL 793-1016

Fig. 12

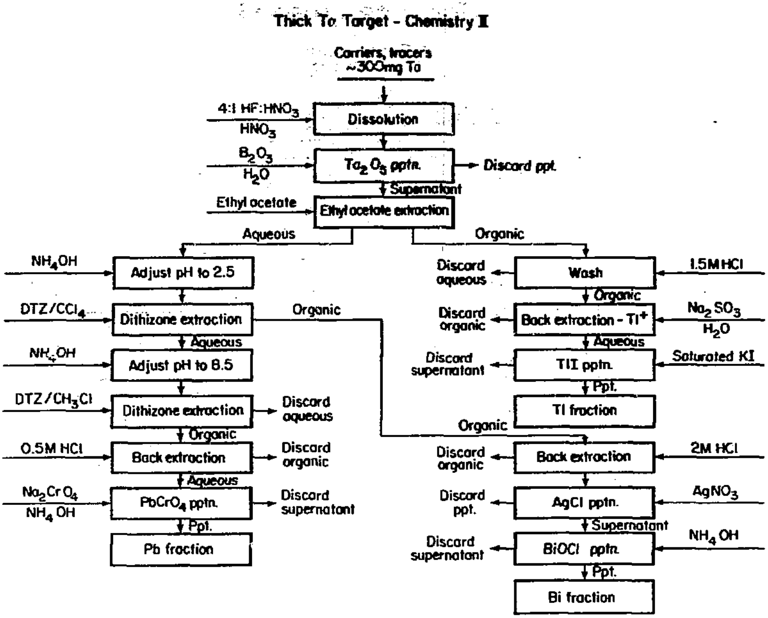

XBL 793-1012

Fig. 13

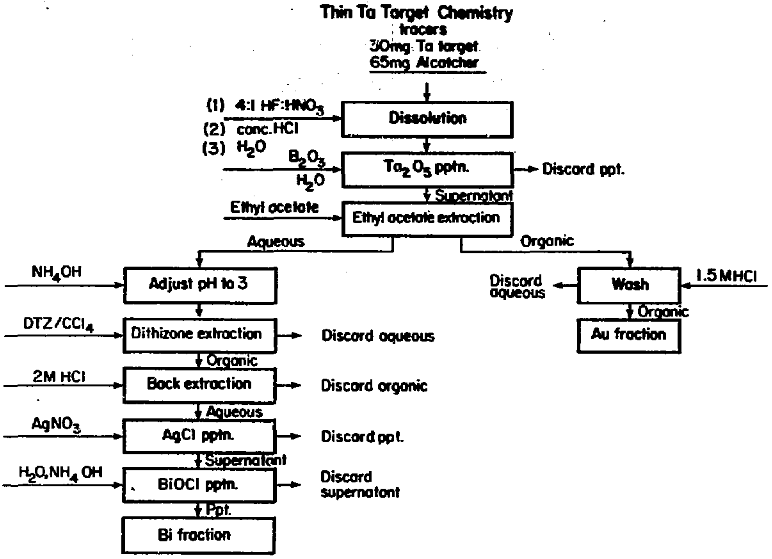

XBL 793-1015

Fig. 14

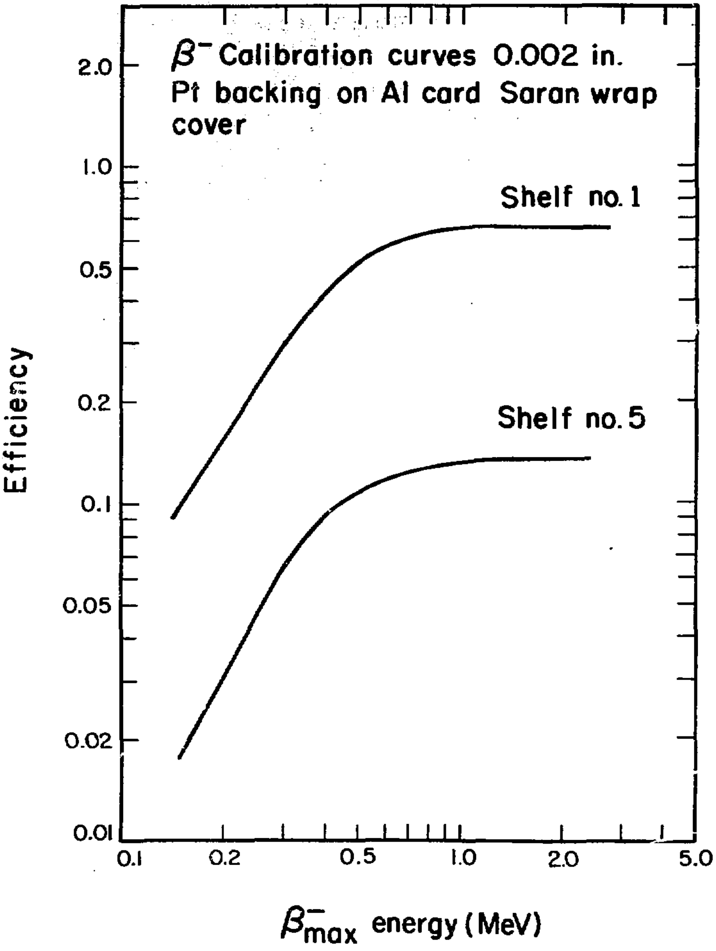

XBL 7910-4446

Fig. 15

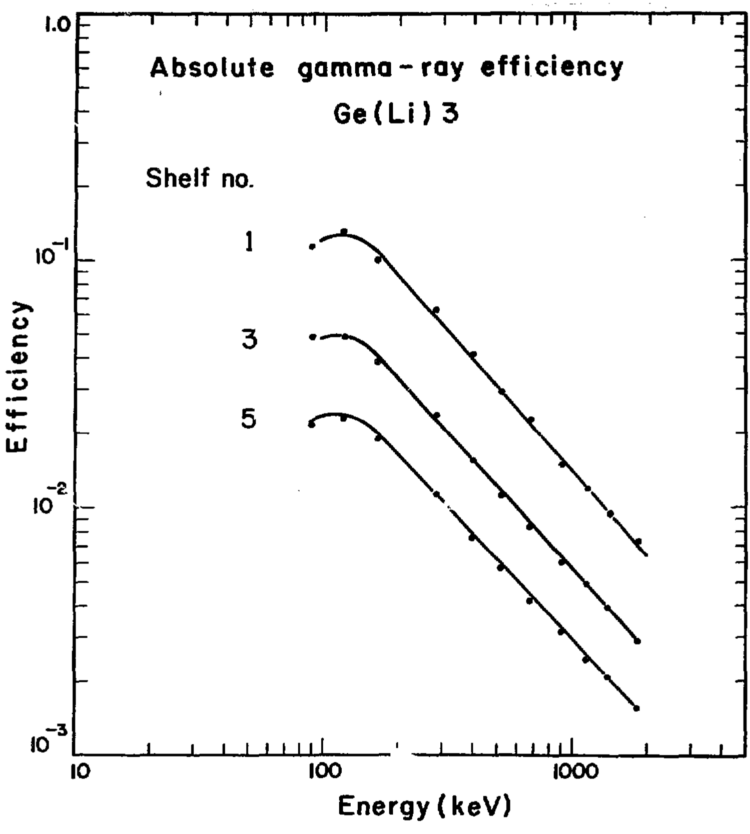

XBL 7910-4454

Fig. 16

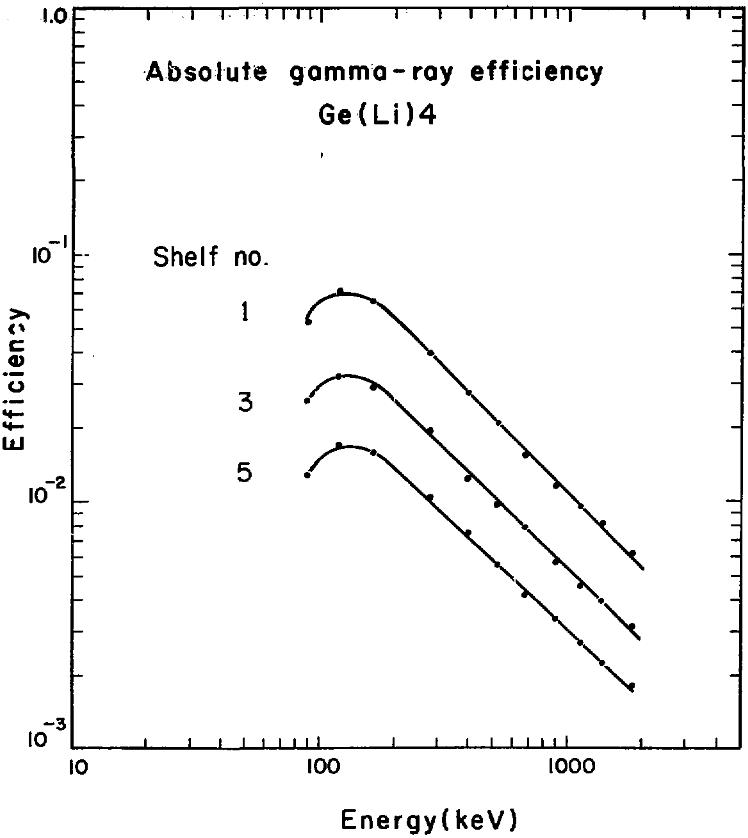

XBL 7910-4453

Fig. 17

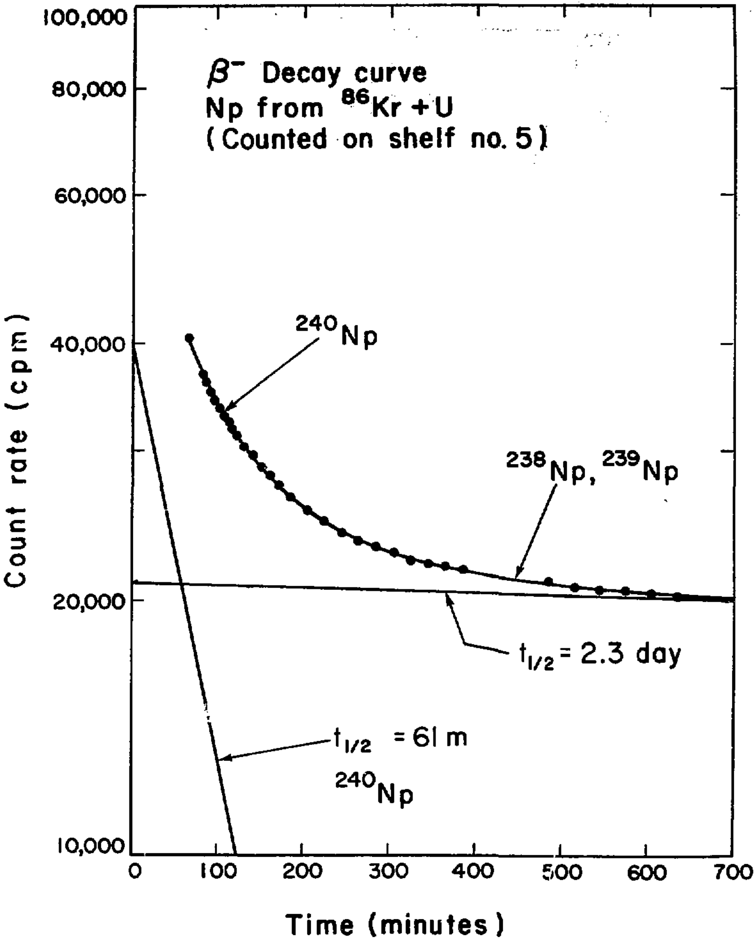

XBL 7910-4452

Fig. 18

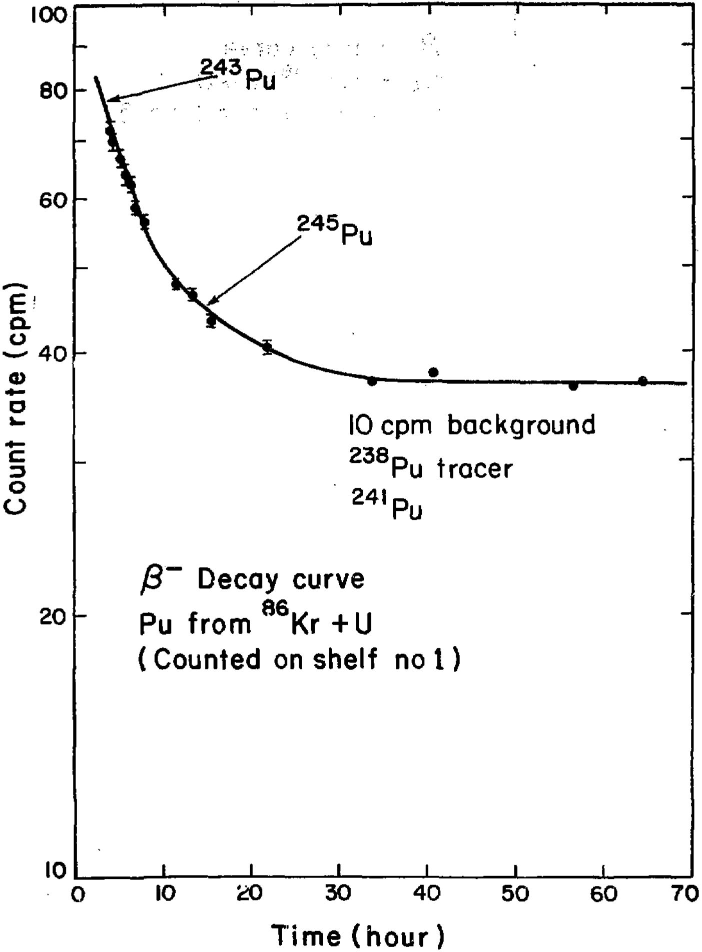

XBL 7910-4448

Fig. 19

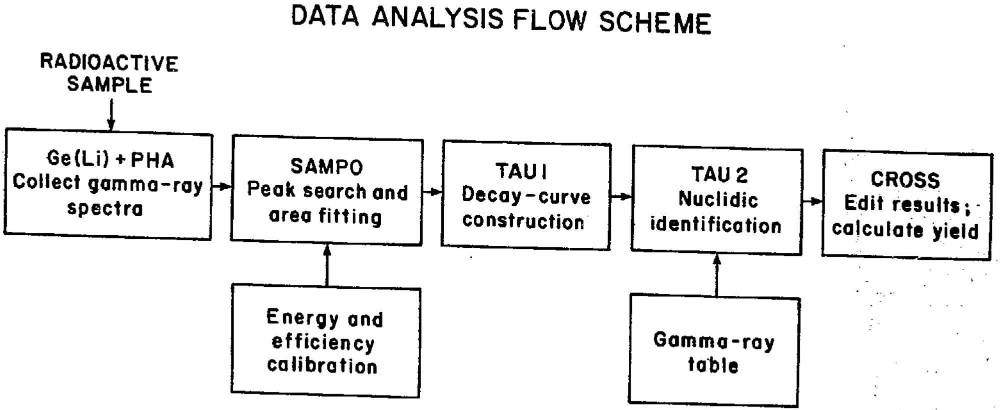

XBL 7910-4449

Fig. 20

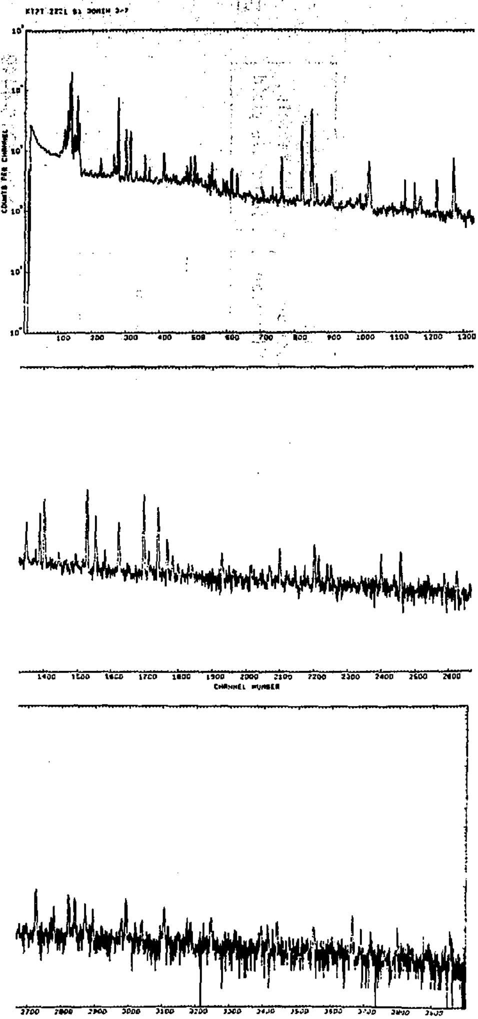

XBL 7910-12157

Fig. 21

```
1143              884.5KEV          884.5 SH TL-195      .048

 (A) 882.8 DI  TE-133M      .038    4.8  SB      (K) 884.6 LA HD-156        .038    9.6
 (B) 883.0 LA  PA-234       .281   13.0  PA      (L) 884.6 LA LU-168        .005    8.2   HF
 (C) 883.3 LA  SB-130       .028    1.2  SN      (M) 884.7 SH AG-110M    253.000   74.7
 (D) 883.5 SH  TC-104       .013   12.2          (N) 884.7 PB IN-110M       .209   94.9
 (E) 883.6 DI  SE- 83       .016    7.8          (O) 884.9 PB NP-240        .045    4.0
 (F) 884.0 SH  CD-105       .038    1.0  IN      (P) 886.1 LA PM-141        .014    2.3   SM SM
 (G) 884.1 SH  TA-186       .007    2.5          (Q) 886.7 DI TE-117        .045    1.5   I
 (H) 884.2 I   I -134       .037   64.9  TE      (R) 887.0 I  AT-208        .067    2.1   RN FR
 (I) 884.3 SH  PO-204       .150   19.5  AT RN   (S) 887.0 LA PU-245        .421     .8
 (J) 884.5 SH  TL-195       .048    3.6  PB      (T) 887.0 SH HG-191        .035    1.8   TL

                                  FIT=     .1561
```

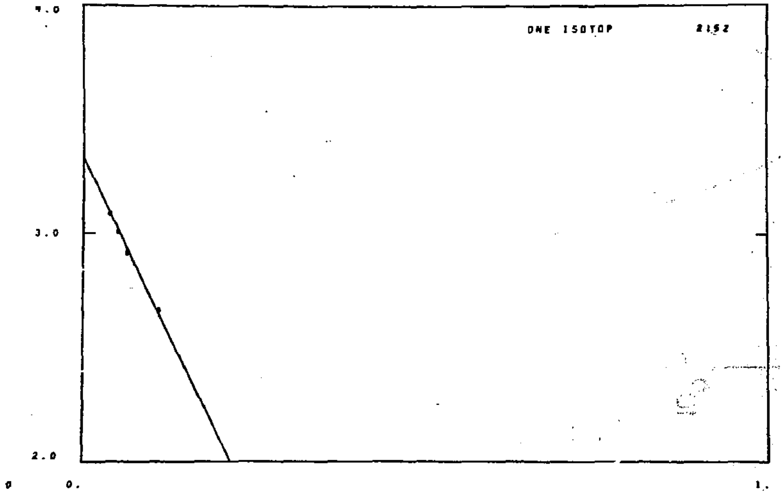

Fig. 22

XBL 7910-12440

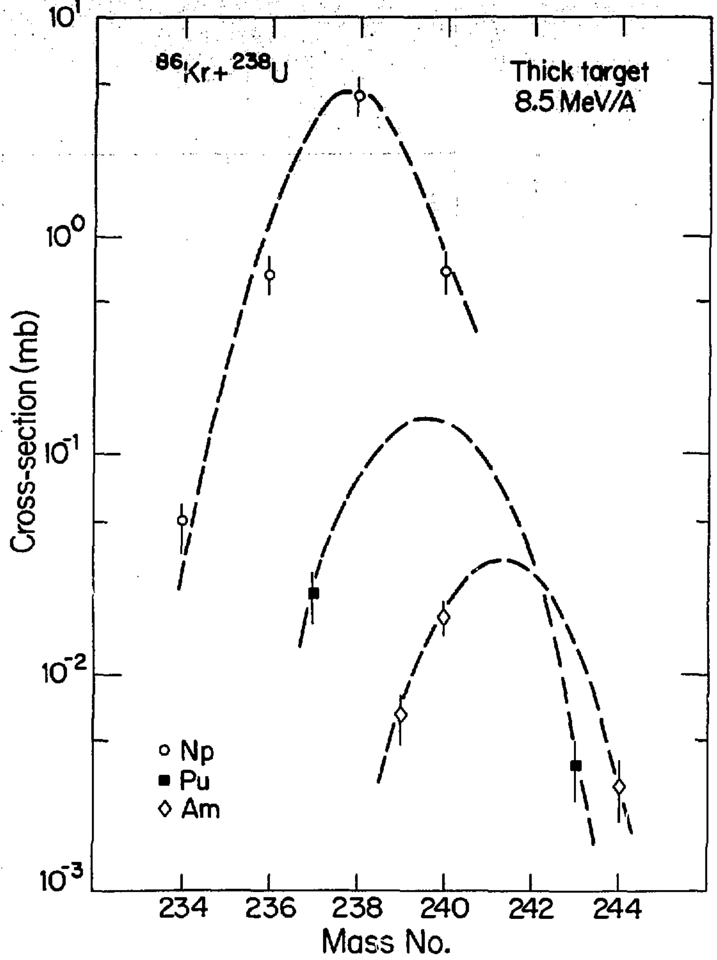

XBL 7910 - 4585

Fig. 23

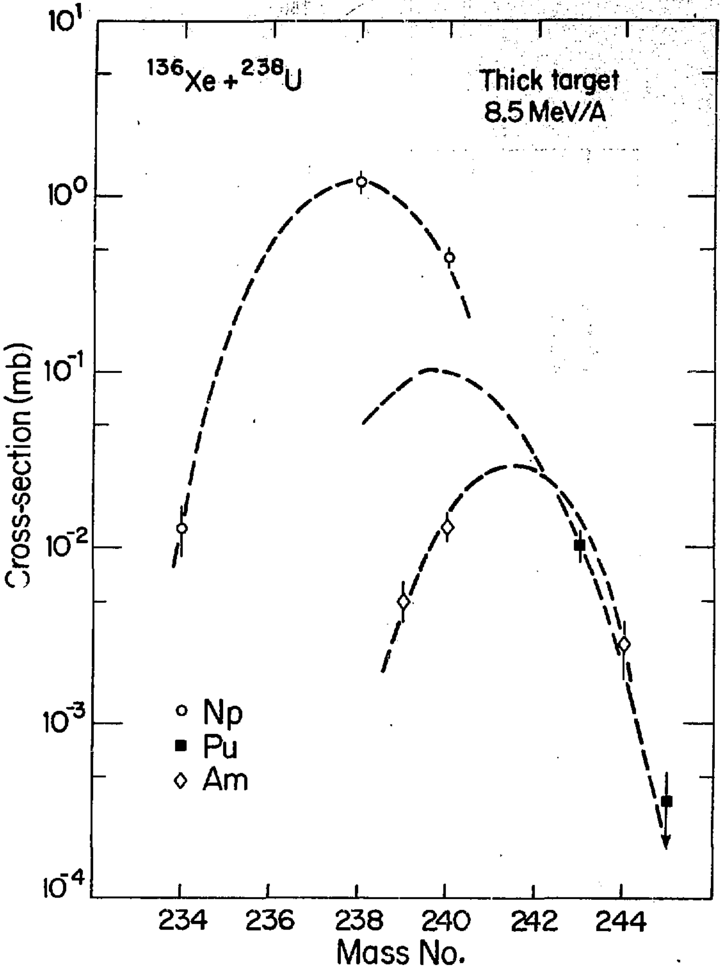

XBL 7910-4584

Fig. 24

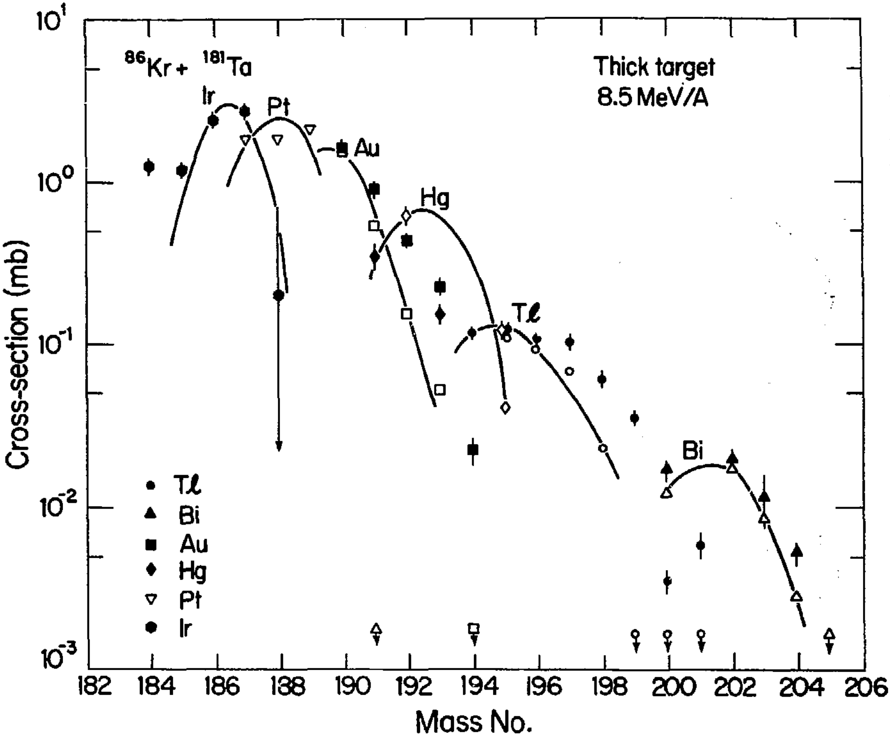

Fig. 25

XBL 7910-4581

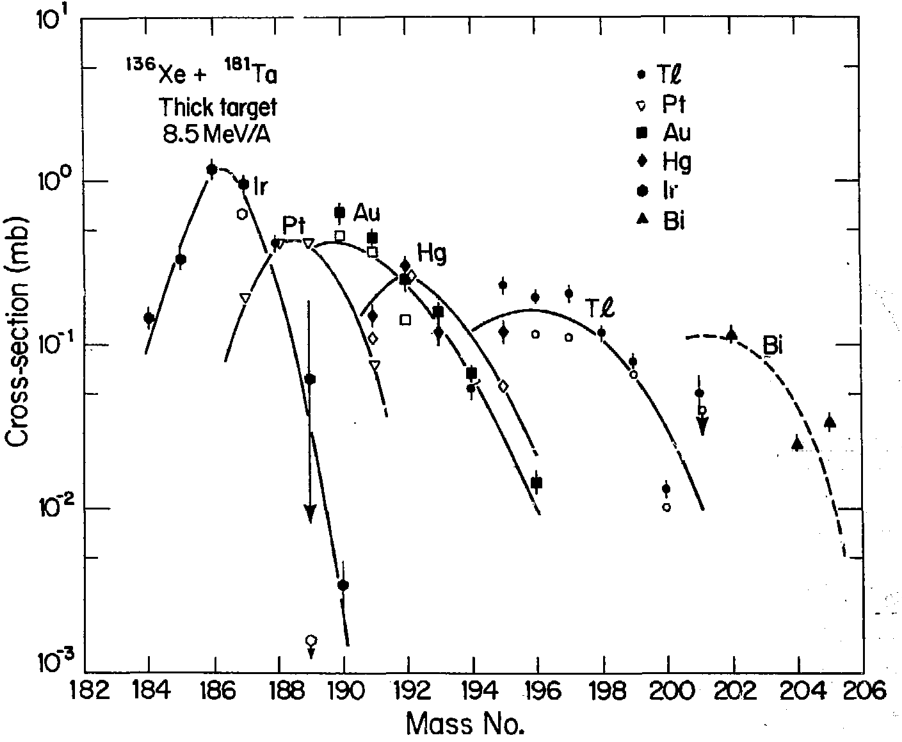

Fig. 26

XBL 7910-4583

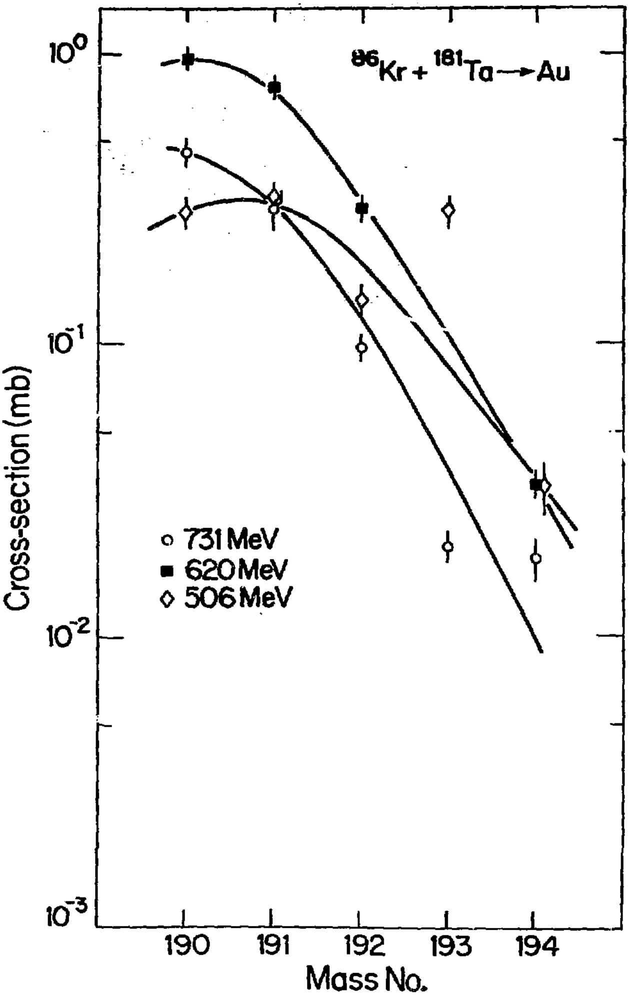

Fig. 27 XBL 7910-4586

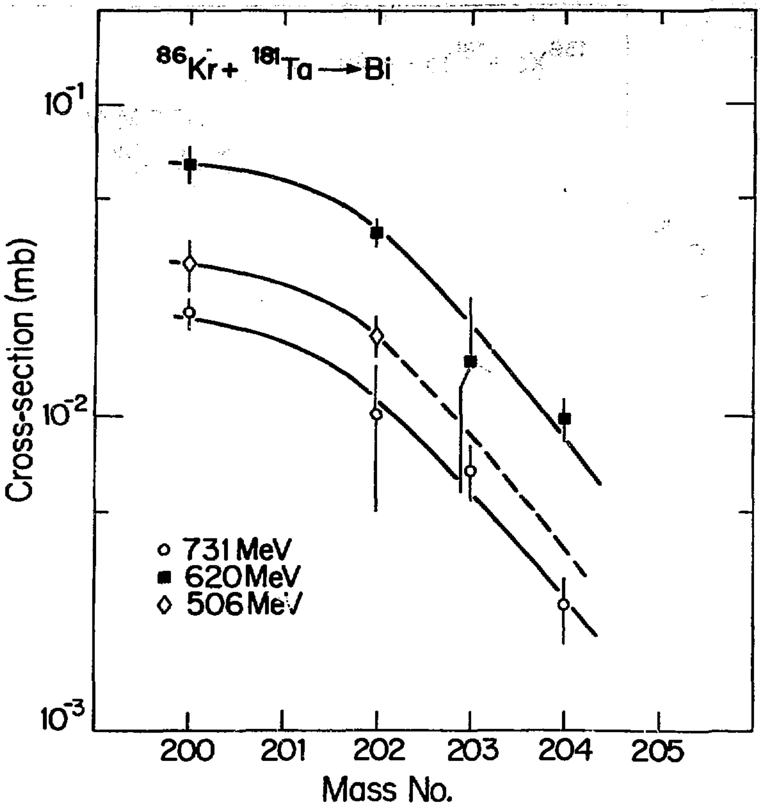

XBL 7910-4579

Fig. 28

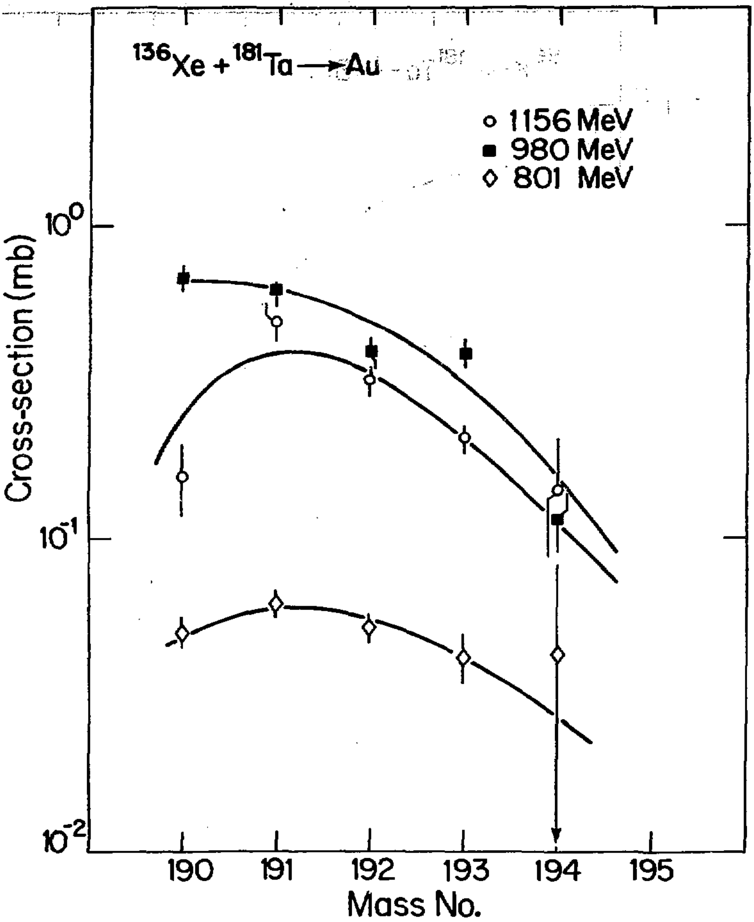

XBL 7910 - 4589

Fig. 29

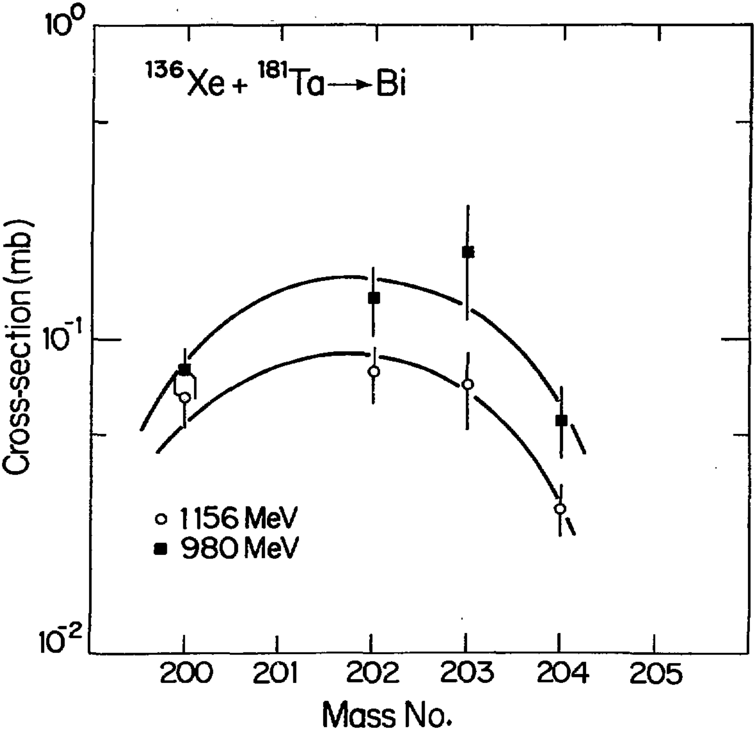

Fig. 30

XBL 7910 - 4580

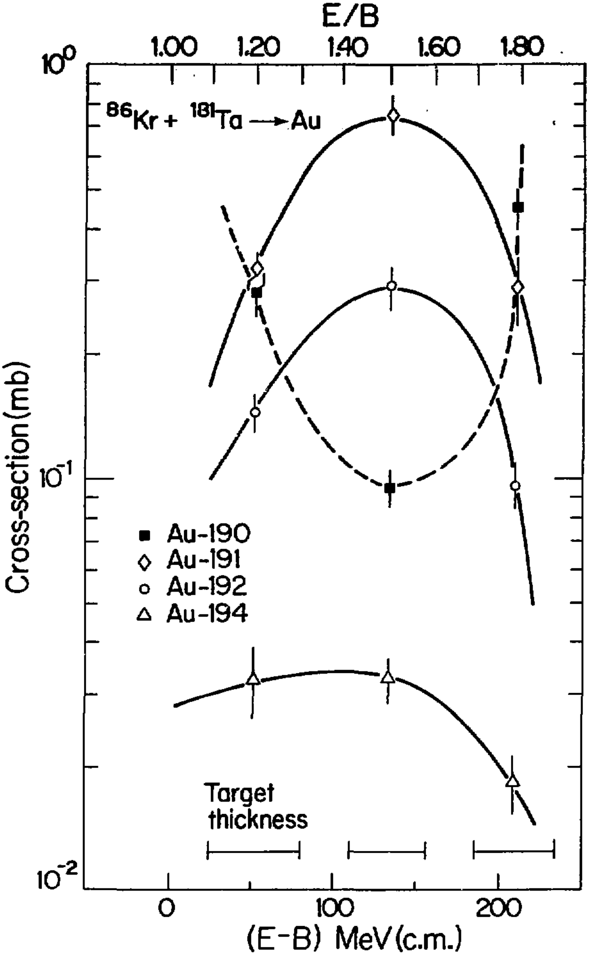

XBL 7910 - 4590

Fig. 31

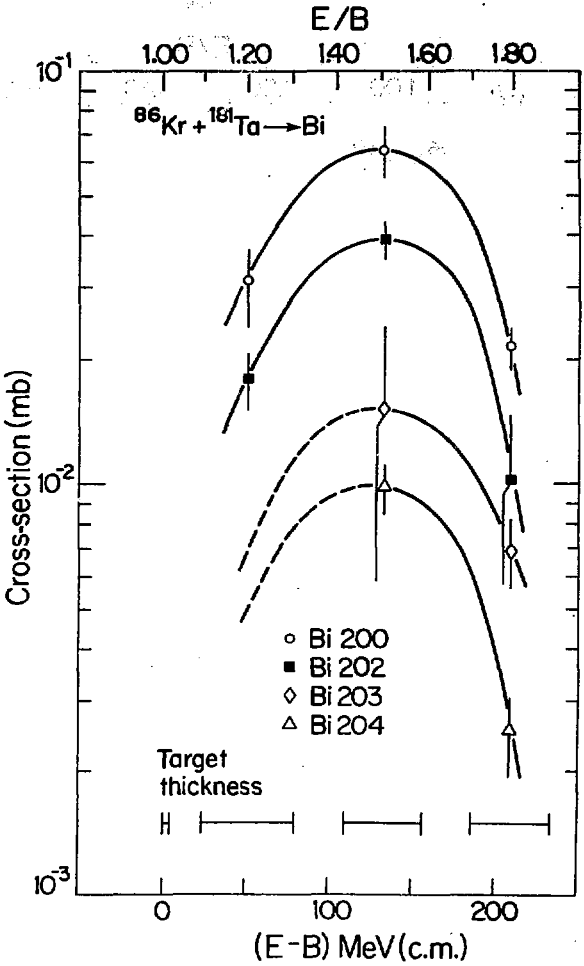

XBL 7910-4588

Fig. 32

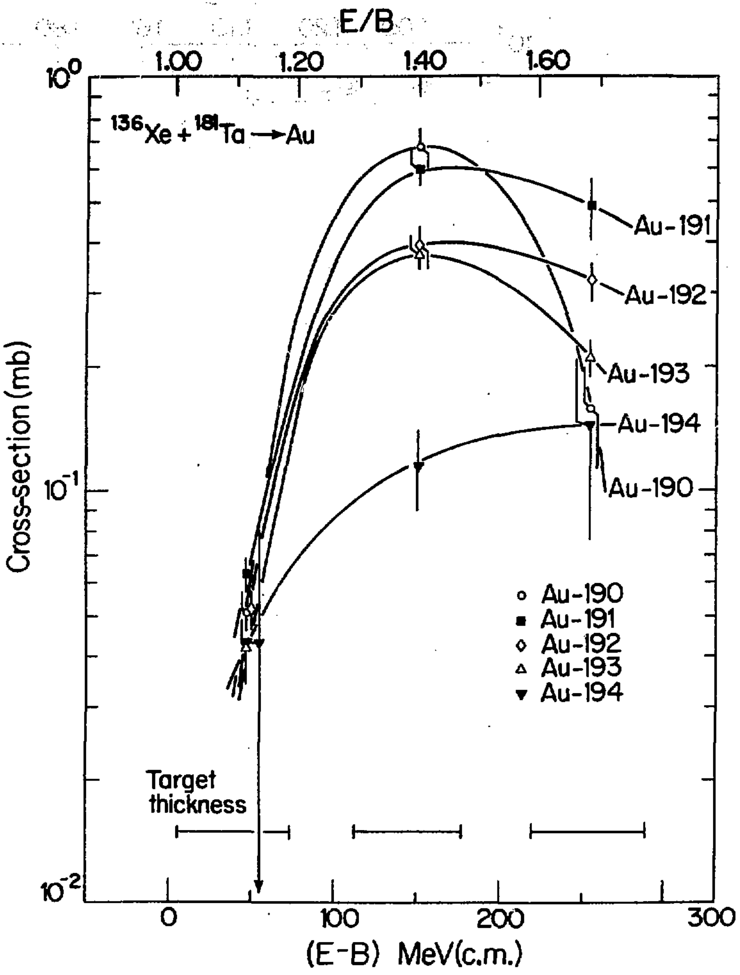

XBL 7910-4592

Fig. 33

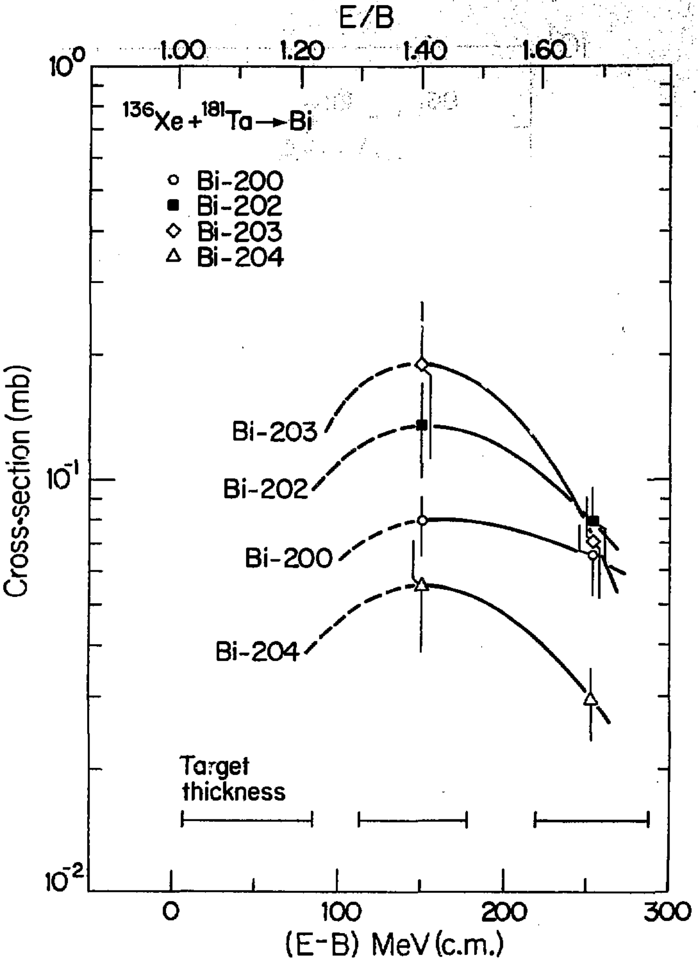

Fig. 34

XBL 7910-4591

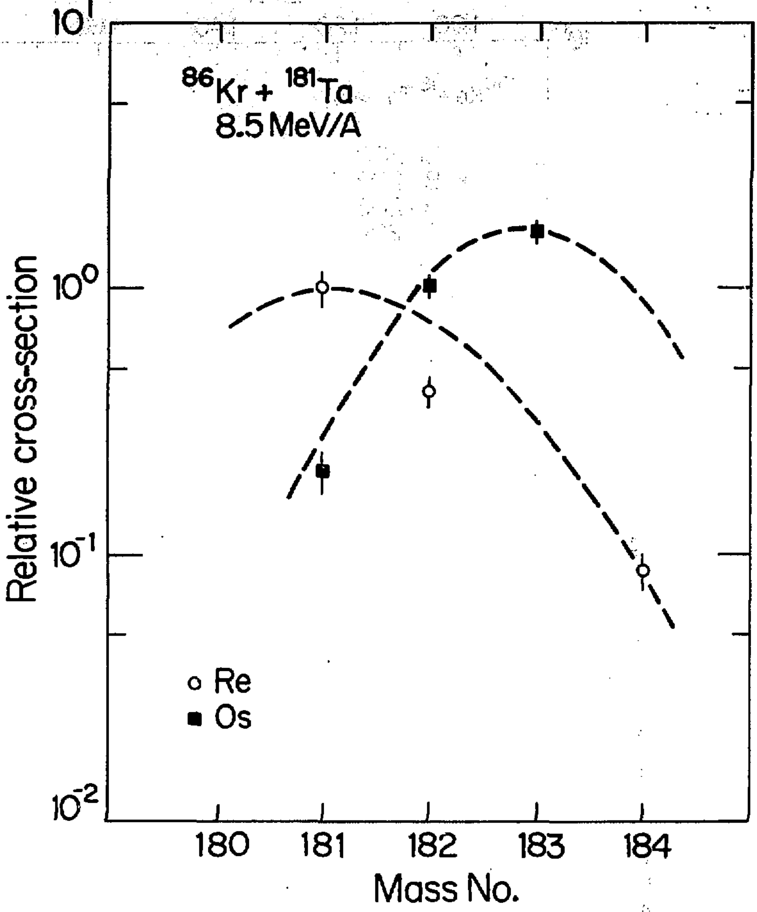

Fig. 35

XBL 7910-4578

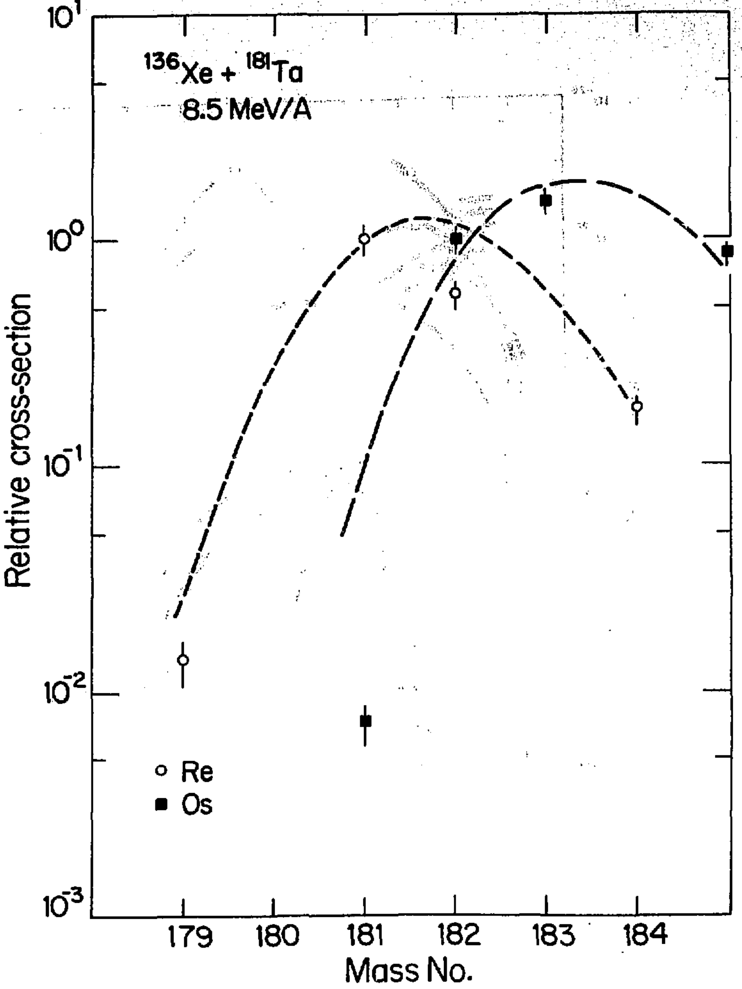

Fig. 36

XBL 7910 - 4587

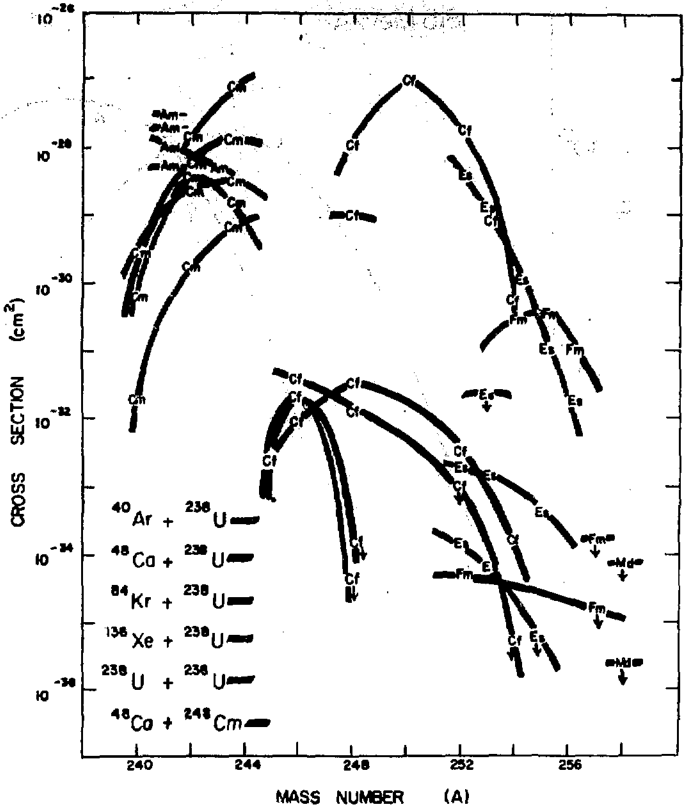

BBC 779-8448

Fig. 37

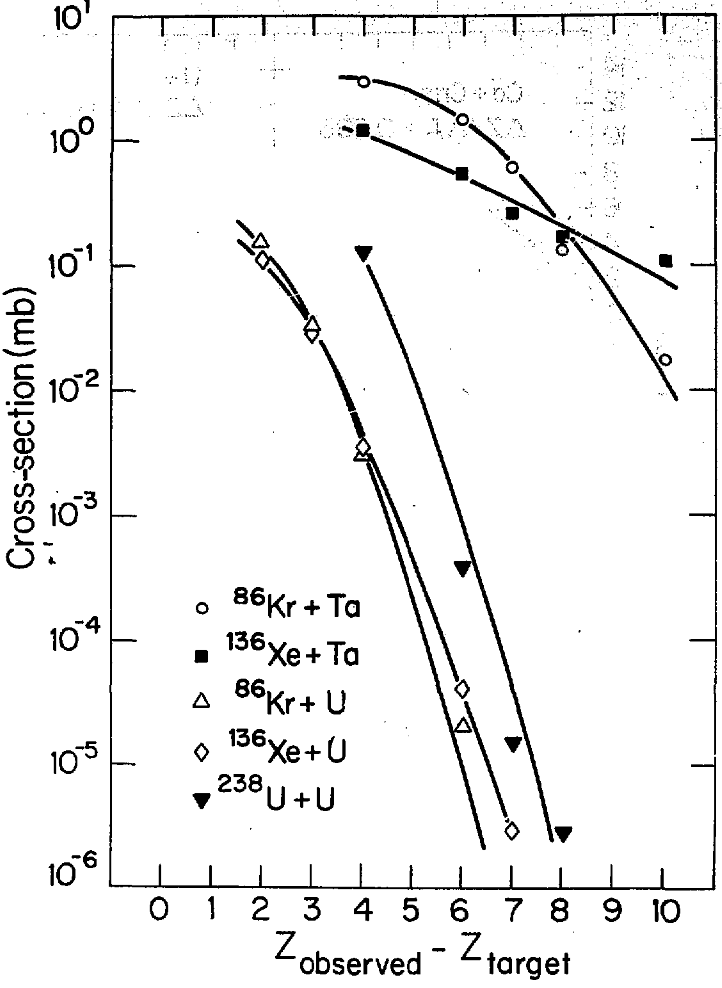

XBL 7910-4577

Fig. 38

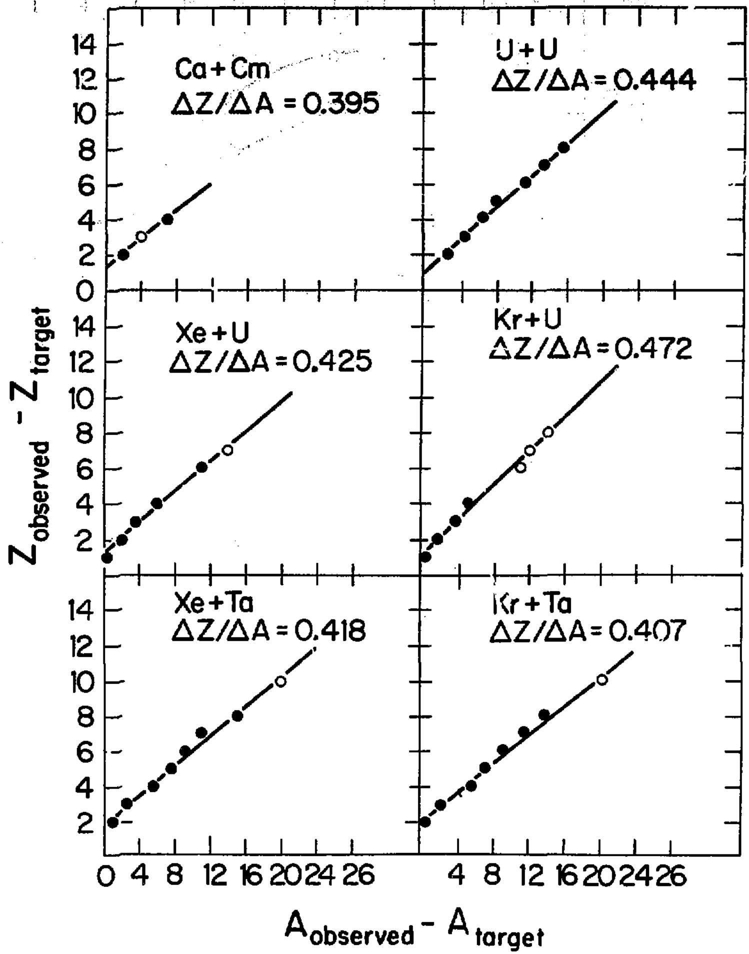

XBL 7910 - 4582

Fig. 39